AD-A084 201 MASSACHUSETTS INST OF TECH CAMBRIDGE FRANCIS BITTER --ETC F/G 20/9
LASER-PRODUCED PLASMAS AND RADIATION SOURCES.(U)
JAN 80 D W SCUDDER, H C PRADDAUDE F44620-76-C-0002
UNCLASSIFIED AFOSR-TR-80-0335 NL

1 OF 2
AD
A084 201

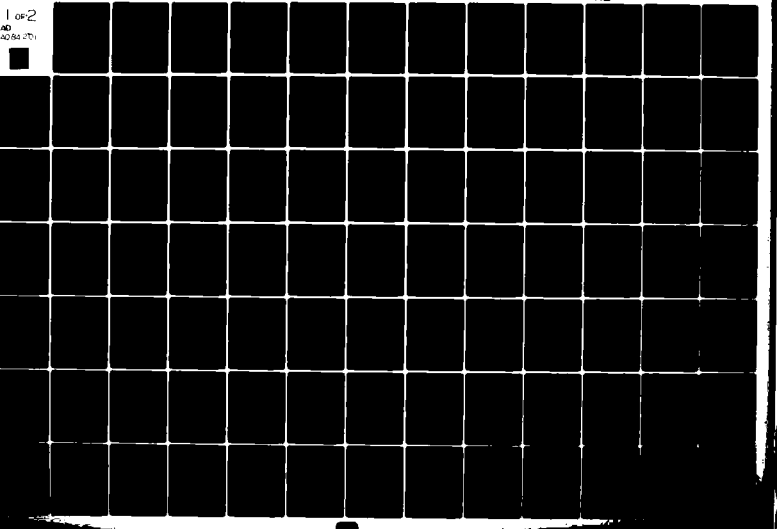

MASSACHUSETTS INSTITUTE OF TECHNOLOGY

FRANCIS BITTER NATIONAL MAGNET LABORATORY

FINAL REPORT

LASER-PRODUCED PLASMAS AND RADIATION SOURCES

Contract F44620-76-C-0002 Mod 4

Air Force Office of Scientific Research

Report Prepared By

D. W. Scudder and Hernan C. Praddaude

Co-Principal Investigator:

Benjamin Lax

Benjamin Lax, Director
Francis Bitter National Magnet Laboratory
Professor of Physics
Soc. Sec. No.: 072-12-7241
Telephone No: (617)253-5541

Co-Principal Investigator:

H. C. Praddaude

Hernan C. Praddaude
Francis Bitter National Magnet Laboratory
Associate Group Leader
Plasma and Laser Systems
Soc. Sec. No.: 133-34-9866
Telephone No.: (617)253-5583

Cambridge, Massachusetts 02139

January 31, 1980

TY CLASSIFICATION OF THIS PAGE (When Data Entered) Unclassified

REPORT DOCUMENTATION PAGE

READ INSTRUCTIONS BEFORE COMPLETING FORM

1. REPORT NUMBER: AFOSR-TR-80-0335	2. GOVT ACCESSION NO.: AD-A084 201
3. RECIPIENT'S CATALOG NUMBER	
4. TITLE (and Subtitle): LASER-PRODUCED PLASMAS AND RADIATION SOURCES	5. TYPE OF REPORT & PERIOD COVERED: Final, 1 Jul 75 - 30 Sep 79
	6. PERFORMING ORG. REPORT NUMBER
7. AUTHOR(s): D. W. Scudder, Hernan C. Praddaude	8. CONTRACT OR GRANT NUMBER(s): F44620-76-C-0002
9. PERFORMING ORGANIZATION NAME AND ADDRESS: Francis Bitter National Magnet Laboratory, Massachusetts Institute of Technology, Cambridge, MA 02139	10. PROGRAM ELEMENT, PROJECT, TASK AREA & WORK UNIT NUMBERS: 61102F 2301/A7
11. CONTROLLING OFFICE NAME AND ADDRESS: AFOSR/NP, Bolling AFB, Wash DC 20332	12. REPORT DATE: 31 Jan 1980
	13. NUMBER OF PAGES: 167
14. MONITORING AGENCY NAME & ADDRESS (if different from Controlling Office)	15. SECURITY CLASS. (of this report): unclassified
	15a. DECLASSIFICATION/DOWNGRADING SCHEDULE

16. DISTRIBUTION STATEMENT (of this Report)

Approved for public release; distribution unlimited.

17. DISTRIBUTION STATEMENT (of the abstract entered in Block 20, if different from Report)

18. SUPPLEMENTARY NOTES

19. KEY WORDS (Continue on reverse side if necessary and identify by block number)

20. ABSTRACT (Continue on reverse side if necessary and identify by block number)

The magnetic field was shown to affect stimulated scattering. The process is affected by alteration of the acoustic frequency for strong fields, increasing the redshift and decreasing the homogeneous growth rate. Landau damping is altered depending upon angle and field strength. The dispersion relation is altered affecting the phase mismatch. X-ray diagnostics of solid target plasmas were built and demonstrated. Spectrographic techniques provided the space and time resolved electron density in fluorine plasmas, and somewhat less reliably

DD FORM 1 JAN 73 1473 EDITION OF 1 NOV 65 IS OBSOLETE

UNCLASSIFIED

SECURITY CLASSIFICATION OF THIS PAGE (When Data Entered)

The temperature. A schlieren photography system capable of providing quantitative time and space resolved density measurements was built and demonstrated.

TABLE OF CONTENTS

(AFSC)

(75).

Officer

LIST OF FIGURES

SUMMARY

This final report describes research on laser interaction with matter carried out at the Francis Bitter National Magnet Laboratory under sponsorship of the Air Force Office of Scientific Research. The research performed under this program has covered a broad range of subjects involving laser interaction with both gaseous and solid target laser plasmas, and with development of plasma diagnostic techniques suitable for our laser-produced plasmas.

In this report we ~~only~~ include detailed descriptions of research activities during fiscal years 1978 and 1979. These include a study of stimulated Brillouin scattering in transverse magnetic fields; development of X-ray diagnostics including X-ray continuum measurements, spectroscopy, and imaging techniques and their use in studying solid target plasmas; development of a fast schlieren photography system; and a theoretical study of nonlinear scattering techniques for plasma diagnostics. In a separate package accompanying this report are included reprints of publications and doctorate theses that have resulted from this work.

Research performed under this program since its inception up to fiscal year 1978 have been described in detail in technical publications and in previous year end reports. A partial listing of these publications is included in Appendix A. This earlier research covered the topics of laser-induced gas breakdown in a magnetic field, laser heating of underdense plasmas, laser-driven detonation waves, collisions between laser-driven fronts, laser beam transport through long plasma columns, radial dynamics of the columns causing laser beam self-trapping, and development of a soft X-ray continuum temperature diagnostic using differential gas absorbers.

INTRODUCTION

Since the early seventies, the Air Force Office of Scientific Research has supported, at the Francis Bitter National Magnet Laboratory of the Massachusetts Institute of Technology, a research program to investigate the interaction of intense CO_2 laser radiation with matter in high magnetic fields. This Air Force sponsored research has resulted in substantial scientific advances in the understanding of many phenomena occuring during the irradiation of matter by an intense laser beam.

This final report includes detailed descriptions of the research activities during only the fiscal years 1978 and 1979. Some of this work is described in meticulous detail in two doctorate theses accompanying this report. Earlier work under this grant is well described by reprints of publications in the technical literature, which also accompany this report, and by earlier year end reports.

Chapter I describes a study of the effects of a strong magnetic field on the stimulated Brillouin backscattering instability when the field is nearly perpendicular to the laser propagation direction. This theoretical and experimental study identifies several magnetic field effects that might be important if strong self-magnetic fields are generated in laser targets.

Chapter II describes the study of solid target plasmas using a variety of X-ray diagnostics and involves development of soft X-ray spectroscopic techniques using helium and lithium-like emission lines to determine plasma density and temperature. Other X-ray diagnostics used are X-ray pinhole photography, differential continuum measurements, and collimator plate imaging.

Chapter III describes the development of a schlieren photography system for studying the evolution of laser-heated gaseous target plasmas. The system utilizes a pulsed nitrogen laser so that it provides 10 nsec time resolution, and two dimension of spatial resolution.

Chapter IV details an extensive theoretical study of four-photon nonlinear scattering processes in plasmas. These nonlinear electromagnetic interactions may provide powerful new tools for plasma temperature diagnostics since they can produce considerable signal enhancement over conventional scattering techniques, and, being coherent interactions, produce a collimated scattered beam.

In the appendices we provide a partial list of technical publications, one of conference presentations and seminars, and a list of students' theses relating to work carried out during the period of this AFOSR grant.

Other areas of research described in accompanying journal reprints cover a broad range of phenomena involved in laser interaction with magnetized, underdense, gaseous-target plasmas. Laser-induced gas breakdown was found to be affected by a magnetic field through inhibition of particle diffusion. Both axial and radial dynamics of laser-generated plasma columns were studied including bleaching waves, laser-driven detonation waves, collisions between laser driven fronts, radial expansion, and the accompanying laser beam self-trapping. In addition, the soft X-ray continuum temperature diagnostic was extended to use with low flux levels by using gas differential absorbers in place of the more conventional thin films.

I. Stimulated Brillouin Scattering in a Strong Transverse Magnetic Field

I.A. Introduction

Stimulated Brillouin scattering has been identified as probably the most important non-linear interaction leading to losses in laser heating of plasmas. Thus it is a subject of considerable interest in laser fusion research. While it has been the subject of a large amount of both theoretical and experimental study, very little attention has been given to the effects of strong magnetic fields in the plasma, this despite the presence of fields estimated to be in the 100s of Tesla in plasmas surrounding laser imploded pellets.

The experience of the group with laser plasma interaction studies and the availability of controlled high magnetic fields at the Francis Bitter Magnet Laboratory provided a good basis for such a study. This study has involved a theoretical and experimental effort to identify and evaluate the effects of a magnetic field immersed in an irradiated plasma with the field direction nearly perpendicular to the laser propagation direction. A 300 J CO_2 laser was used to irradiate plasmas of a number of gases in fields of up to 10T.

The results of the theoretical study will be given in Section I.B. and the experiment will be described in Section I.C. Section I.D. gives the comparisons between experiment and theory and the conclusions of the study.

I.B. Theoretical Results

Stimulated Brillouin scattering (SBS) is the decay of a photon of a strong electromagnetic field incident on a plasma into a quantum of a plasma sound wave (ion-acoustic wave) and a second photon down-shifted in frequency. It is a stimulated process since the decay probability is proportional to the amplitude of the ion-acoustic wave already present in the plasma. Thus such an ion-acoustic wave grows exponentially under the influence of the instability, as does the fraction of the incident field that is scattered, until convection or saturation limits the growth. The effects of the magnetic field on stimulated Brillouin scattering for cases of interest enter primarily through alteration of the ion-acoustic mode in the plasma, as well as through changes in macroscopic plasma behavior. Two of the effects have been examined theoretically. The first is the effect of the field on the Landau damping of the ion-acoustic waves. The second is its effect on convective growth of the instability. These will be treated in the following subsections.

1. Magnetic effects on Landau damping

In the theoretical investigation, we need knowledge of the dynamics of the stimulated plasma mode. This involves finding the magnetized plasma susceptibility while treating the mode as purely electrostatic in character. It is well known that the field-free ion acoustic wave is exactly longitudinal- and we assume that this characteristic does not change substantially with the introduction of the transverse magnetic field and the laser pump field. The validity of this assumption is borne out by actually finding a solution with electrostatic character.

Assuming a Maxwellian plasma (with differing electron and ion temperatures), the magnetized susceptibility is given by:

$$\chi_\alpha = \frac{1}{k^2\lambda_{D\alpha}^2}\left[1 + \frac{\omega}{k_z v_{T\alpha}} \sum_{\ell=-\infty}^{\infty} I_\ell(b_\alpha)\, e^{-b_\alpha} Z(\zeta_\ell)\right] \qquad \text{(I-1)}$$

where $\lambda_{D\alpha}$ is the Debye length contribution from species α, $v_{T\alpha}$ is the thermal speed ($\sqrt{\frac{2k_B T_\alpha}{m_\alpha}}$), and

$$b_\alpha \equiv \frac{k_\perp^2 v_{T\alpha}^2}{2\Omega_\alpha^2} \qquad \text{(I-2)}$$

$$\zeta_\ell \equiv \frac{\omega - \ell\Omega_\alpha}{k_z v_{T\alpha}} \qquad \text{(I-3)}$$

Here, I_ℓ in the modified Bessel function and Z is the plasma dispersion function (or Fried-Conte[1] integral).

The expression for the susceptibility becomes analytically invertible if we make use of limiting forms for I_ℓ and Z. Since propagation is nearly perpendicular to $\hat{z}$, $b_e \gg 1$ always, and the asymptotic form $I_\ell(b)\, e^{-b} \simeq \frac{1}{\sqrt{2\pi b}}$ can be used for the electrons with an error of at most a few per cent (except, in our plasmas, for very strong fields in hydrogen sparks.) To high accuracy then,

$$\chi_e \cong \frac{1}{k^2\lambda_{De}^2}\left[1 + \frac{\omega}{k_z v_{Te}} \cdot \frac{\Omega_e}{\sqrt{\pi}\, k_\perp v_{Te}} \sum_\ell Z(\zeta_\ell)\right] \tag{I-4}$$

The asymptotic form for the plasma dispersion function can also be used. For ions, we need note only that the ion gyroradii for most of our plasmas not only exceeds the wavelengths expected, but exceeds plasma dimensions as well, with the exception, again, of strong fields in hydrogen. This allows us to treat the ions as unmagnetized to a very good approximation. Failure to make this assumption would lead to severe difficulties in handling the Fried-Conte function of magnetically extended argument. Keeping the most important terms in both electronic and ionic susceptibilities, including the term which will result in the ionic pressure contribution to the wave, we get, for the real part of the dielectic function,

$$\varepsilon_R \cong 1 - \frac{\omega_{pi}^2}{\omega^2} - 3k^2\lambda_{Di}^2 \frac{\omega_{pi}^4}{\omega^4} + \frac{1}{k^2\lambda_{De}^2}\left\{1 - \frac{\Omega_e}{\sqrt{\pi}\, k_\perp v_{Te}} \times \left[1 + \frac{\omega}{\omega - \Omega_e} + \frac{\omega}{\omega + \Omega_e}\right]\right\} \tag{I-5}$$

Using $I_m\, Z(\zeta_\ell) = \sqrt{\pi}\, e^{-\zeta^2}$ for real argument or for $Im\zeta_\ell < \frac{1}{R_e \zeta_\ell}$, we get

$$\varepsilon_I = \frac{1}{k^2\lambda_{De}^2} \cdot \frac{\omega}{k}\left[\frac{ZT_e}{T_i} \cdot \frac{\sqrt{\pi}}{v_{Ti}} \exp\left(\frac{-\omega}{kv_{Ti}}\right)^2 + \frac{\Omega_e}{k\, v_{Ti}^2 \sin\phi \cos\phi} \times \sum_\ell \exp - \left(\frac{\omega - \ell\Omega_e}{k\, v_{Ti} \sin\phi}\right)^2\right] \tag{I-6}$$

where ϕ is the angle between the propagation direction and true perpendicular. Then, noting that $\frac{\partial Im\varepsilon}{\partial\omega} \ll \frac{\partial Re\varepsilon}{\partial\omega}$, we can use the simple form of

the Taylor Series result $\gamma = \dfrac{\mathrm{Im}\epsilon}{\dfrac{\partial \mathrm{Re}\epsilon}{\partial\omega}\Big|_{\omega=\omega_R}}$. This yields, for the ratio of the damping rate to the wave frequency,

$$\frac{\gamma}{\omega} = -\frac{\omega}{k}\left[\frac{ZT_e}{T_i}\frac{\sqrt{\pi}}{v_{Ti}}\exp - \left(\frac{\omega}{kv_{Ti}}\right)^2 + \frac{\Omega_e}{kv_{Te}^2\ \sin\phi\ \cos\phi}\right.$$

$$\left.\times\ \sum_{\ell}\exp -\left(\frac{\omega - \ell\Omega_e}{kv_{Te}\ \sin\phi}\right)^2\right]\Bigg/\left[k^2\lambda_{De}^2\left(2\frac{\omega_{pi}^2}{\omega^2}\right.\right. \qquad \text{(I-7)}$$

$$\left.\left. + \ 12k^2\lambda_{Di}^2\ \frac{\omega_{pi}^4}{\omega^4}\right) + \frac{\Omega_e}{\sqrt{\pi}\,kv_{Te}\cos\phi}\ \frac{4\Omega_e^2}{\omega^2}\left(1 - \frac{\Omega_e^2}{\omega^2}\right)^{-2}\right]$$

It is also necessary to solve for the real wave frequency in this same spirit of approximation. This yields,

$$\omega^2 = k^2\omega_{pi}^2\lambda_{De}^2\ \frac{\left\{1 \pm \left[1 + 12\left(\frac{\lambda_{Di}}{\lambda_{De}}\right)^2\left(1 + k^2\lambda_{De}^2 - \frac{\Omega_e}{\sqrt{\pi}\ k_\perp v_{Te}}\right)\right]^{\frac{1}{2}}\right\}}{2\left[1 + k^2\lambda_{De}^2 - \frac{\Omega_e}{\sqrt{\pi}\ k_\perp v_{Te}}\right]} \qquad \text{(I-8)}$$

An examination of the eq.(I-7) for γ/ω reveals the dynamic nature of the problem. The first term in the denominator of the expression is all that would remain for the case of a field-free plasma with cold ions. This represents the interaction of electronic pressure with ionic inertia. The second term is a smaller one, and has been included to account for ionic pressure.

As with the electronic pressure contribution, this effect is easily obtainable from a fluid theory. The third term in the denominator is derived only from a kinetic approach, since it requires the analytical procedure to be cognizant of the electron gyroorbits. This term corresponds to the similar $\dfrac{-\Omega_e}{\sqrt{\pi}\ k_\perp v_{Te}}$ term in the expression for ω^2.

Note that, in our work $\Omega_e^2 \gg \omega^2$ generally, and so the term in eq.(I-7) reverts to the same form as in eq.(I-8), proportional to the magnetic field strength.

The numerator of eq.(I-7) contains two terms, one of which is a summation. The first term is recognizable as ordinary ion Landau damping, unaffected by the presence of the magnetic field. The second term is a contribution to the damping from magnetized electrons, in a manner which is qualitatively different from free electron damping. The term is again proportional to the magnetic field strength if only the $\ell=0$ term in the infinite sum is considered. Notice however, that it bears a more complicated angular dependence.

Equation (I-7) is plotted in Figs.(I-1) - (I-4) as a function of magnetic field and of angle between $\bar{k}$ and the normal to $\bar{B}$.

The Landau damping given by eq.(I-7) affects both the threshold and the absolute growth rate for SBS. In the infinite homogeneous case (i.e., no spatial variation in plasma parameters or field amplitudes) the growth rate for backscattering just above threshold is [2]

$$\gamma_o = \frac{\omega_{pi}^2}{2\gamma_a} \frac{c}{c_s} \frac{v_o^2 - v_{oT}^2}{c^2} \frac{ck_o}{\omega_o} \qquad \text{(I-9)}$$

where γ_a is the ion-acoustic wave damping from eq.(II-7), c_s is the sound speed, v_o is the quiver velocity in the pump field and v_{oT} its threshold value. The threshold is [2]

$$\frac{v_{oT}^2}{c^2} = \frac{2\gamma_a\gamma_1}{\omega_{pi}^2} \frac{\omega_o}{k_o c} \frac{c_s}{c} \qquad \text{(I-10)}$$

where γ_1 is the damping of the backscattered wave. Thus it is apparent that field effects on γ_a will have important effects on the instability.

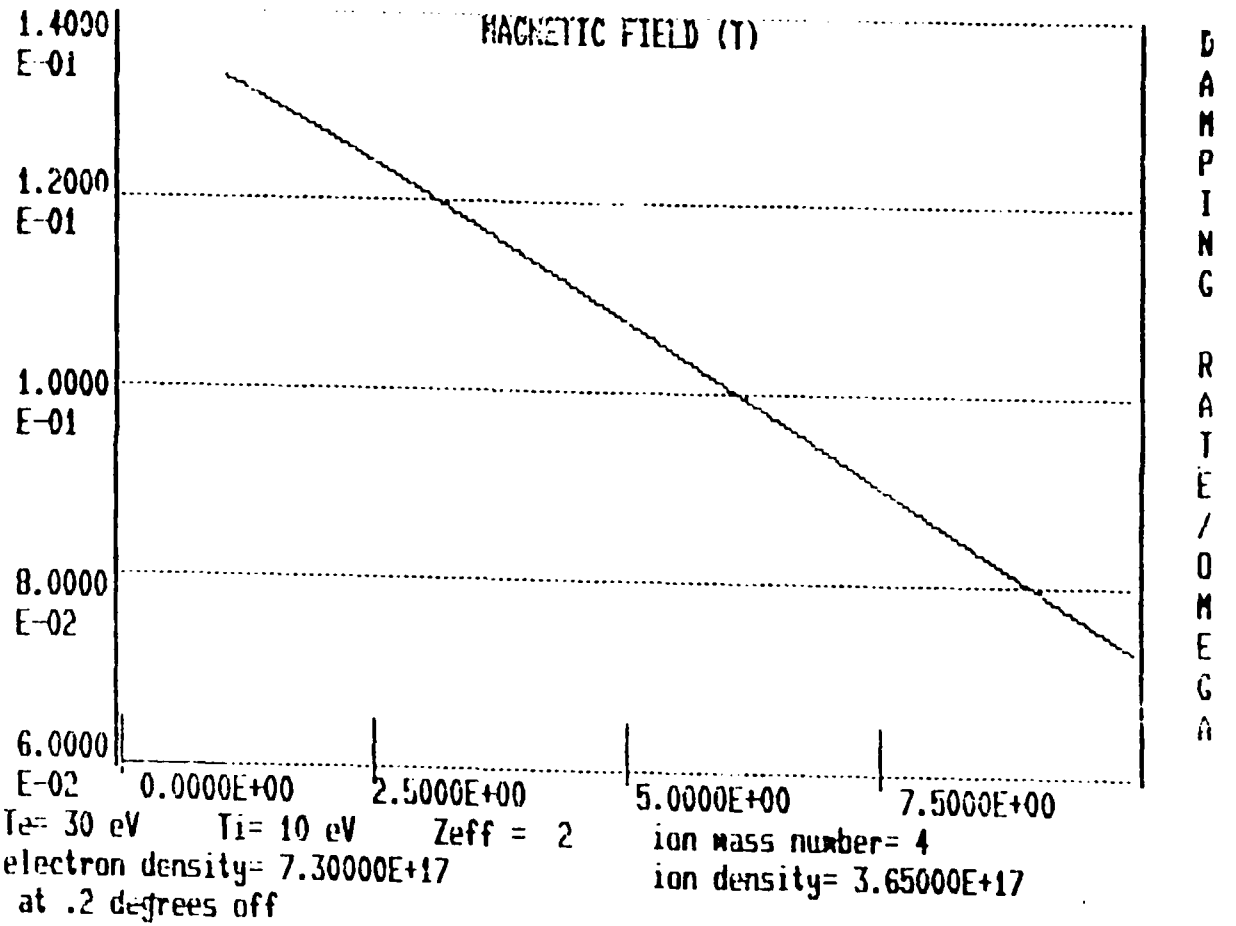

Fig. I-1 Damping rate, γ/ω, versus magnetic field for a helium plasma for E nearly perpendicular to B.

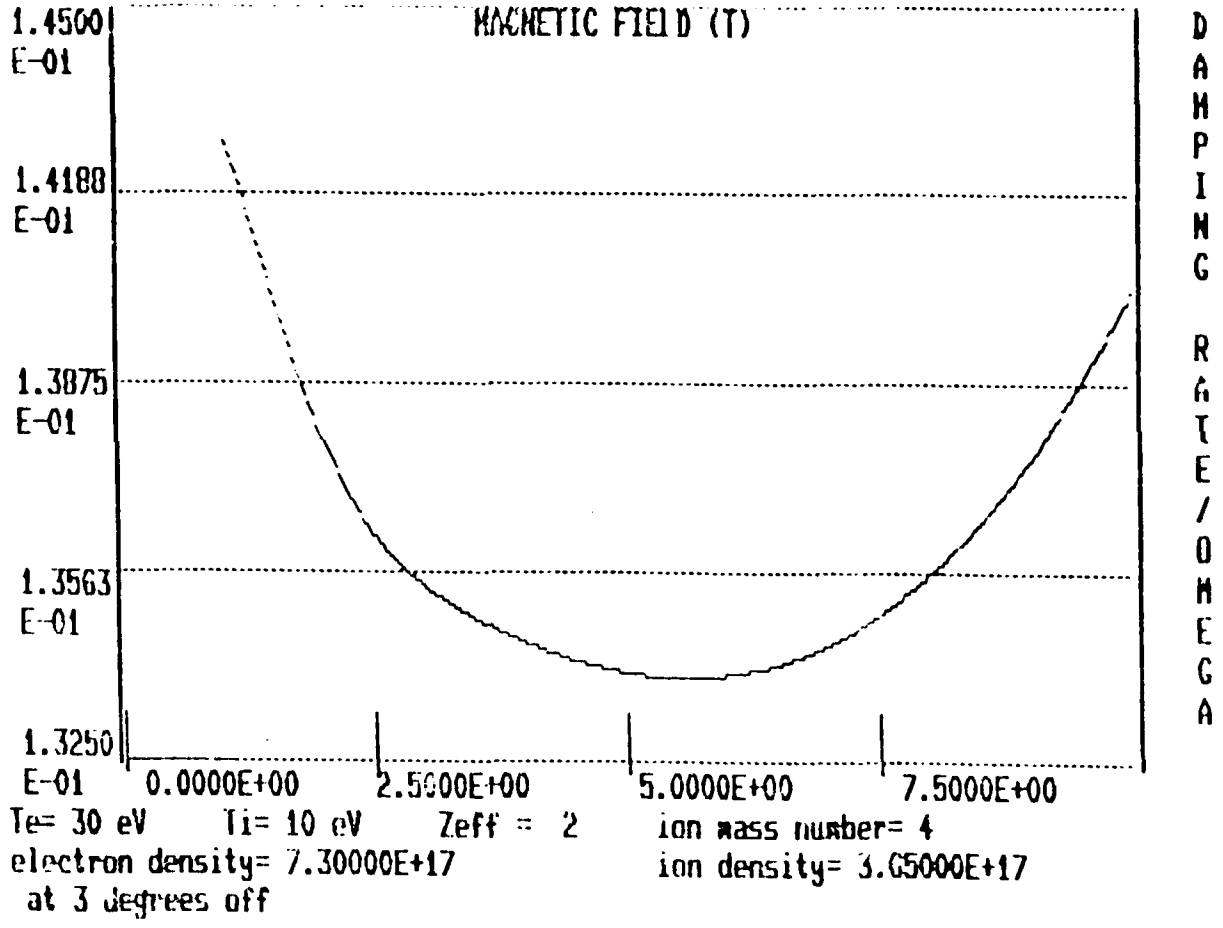

Fig. I-2. Damping rate, γ/ω, versus magnetic field for a helium plasma with $k = 3^{\circ}$ from the perpendicular.

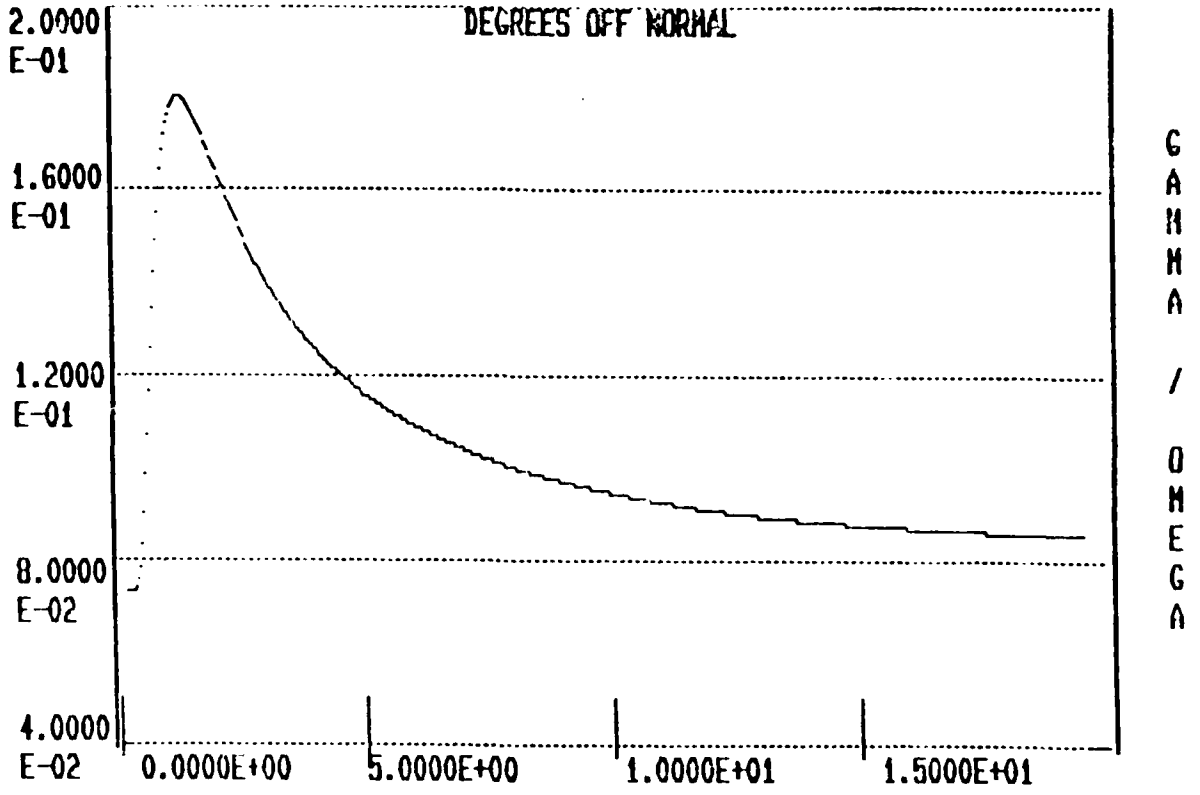

Fig. I-4 Damping rate, γ/ω, versus the angle between $\vec{k}$ and the perpendicular to B at 10T in helium.

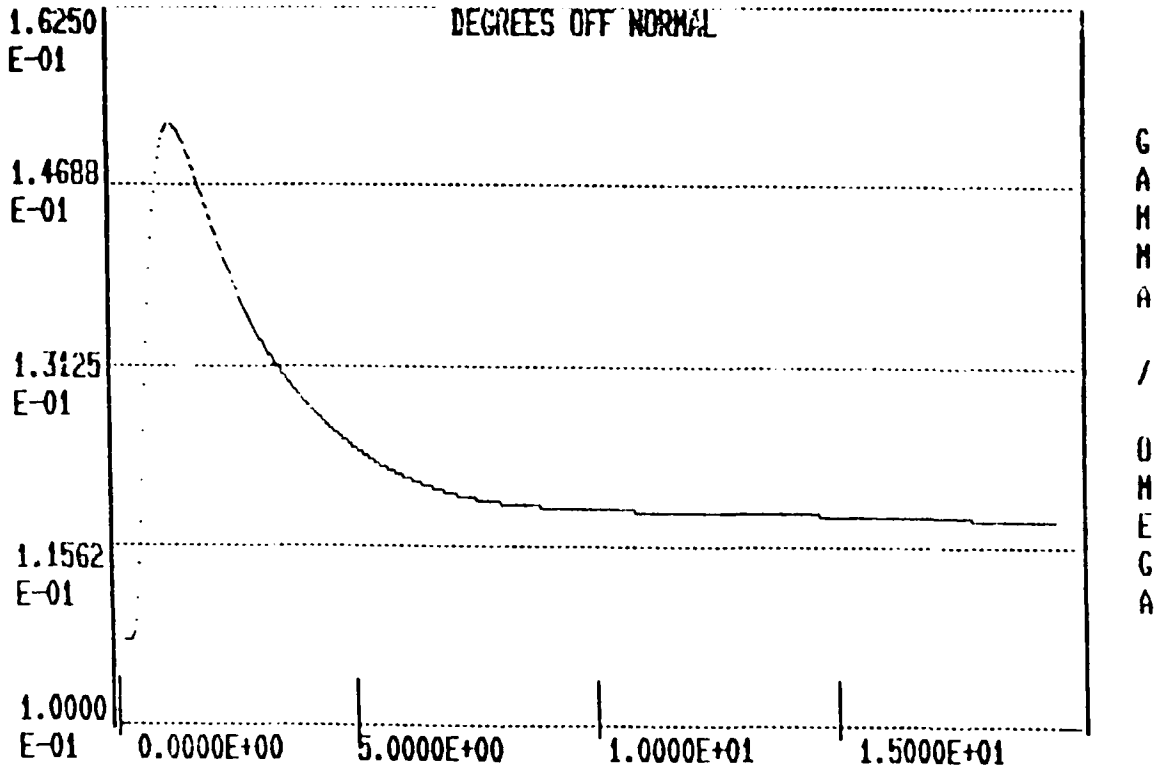

Fig. I-4 Damping rate, γ/ω, versus the angle between $\bar{k}$ and the perpendicular to $\bar{B}$ at 5F in helium.

2. Effect on convective growth

In real plasmas the assumption of infinite homogeneous conditions is almost never appropriate. The effects of plasma nonuniformities and the localized nature of the noise sources from which SBS grows have been described by Liu, Rosenbluth and White.[3,4] Their primary result is that the amplitude of a noise pulse will be amplified to a maximum value given by

$$\frac{a_{max}}{a_o} = \exp\left\{\frac{2\gamma_o^2}{K'cc_s}\left[\frac{\pi}{2} - \frac{(cc_s)^{\frac{1}{2}}}{\gamma_o}\left(\frac{\gamma_l}{c} + \frac{\gamma_a}{c_s}\right)\right]\right\} \qquad \text{(I-11)}$$

Here K' is the spatial derivative of the wavevector mismatch between the three waves. This upper limit is a result of the amplified waves' convection out of the region in which amplification can occur.

In addition to the magnetic field affects on γ_a discussed above, this amplification factor is affected by changes in K' introduced by the field. In order to estimate K' we consider the case of a mismatch due to Doppler shifting of the ion wave frequency by plasma expansion. For the validity of the following, all scale lengths are necessarily greater than a few wavelengths. For CO_2 laser backscattering, this puts a minimum on scale lengths of several times five microns. Taking the derivative of

$$\bar{K} \equiv \bar{k}_o + \bar{k}_l + \bar{k}_a,$$

$$K' = \frac{\partial}{\partial x} k_{ox}(x) - \frac{\partial}{\partial x} k_{lx}(x) - \frac{\partial}{\partial x} k_{ax}(x) \qquad \text{(I-12)}$$

Then, using the approximate dispersion relation for $B_\perp \neq 0$ and $T_i \neq 0$,

$$\omega \cong \bar{k}\cdot\bar{u} + kc_s D^{-\frac{1}{2}} \tag{I-13}$$

where
$$c_s^2 \equiv \frac{2k_B T_e + 3k_B T_i}{m_i}$$

$$D = 1 + k^2\lambda_{De}^2 - \frac{\Omega_e}{\sqrt{\pi}\, k_\perp v_{Te}} \tag{I-14}$$

and we have allowed for a non-zero blow-off speed

$$\bar{u} = -u(x)\,\hat{x}$$

which we have taken to be only a function of x for simplicity. Here, $u(x)>0$ for plasma motion toward the laser.

This dispersion yields

$$k_a' = k_a\left\{-\frac{\frac{1}{L_u} + \frac{1}{2MD^{3/2}}\left[\frac{1}{L_T}\left(1 - \frac{\Omega_e}{2\sqrt{\pi}kv_{Te}}\right) + k^2\lambda_{De}^2\frac{1}{L_n} + \frac{\Omega_e}{\sqrt{\pi}kv_{Te}L_B}\right]}{\left\{1 - \frac{1}{MD^{3/2}}\left[1 - \frac{3}{2}\frac{\Omega_e}{\sqrt{\pi}kv_{Te}}\right]\right\}}\right\} \tag{I-15}$$

where
$$\frac{1}{L_u} = \frac{\partial \ln u}{\partial x}\ ,\ \frac{1}{L_T} = \frac{\partial \ln T}{\partial x}\ ,\ \frac{1}{L_n} = \frac{\partial \ln n}{\partial x}\ ,\ \frac{1}{L_B} = \frac{\partial \ln B}{\partial x}\ ,$$

$$M = \frac{u}{c_s}$$

and we have used $k_{ax} = k_{a_-}$. This expression is valid only for back-scattering. Note that through the first order in magnetic field strength with neglect of Debye dispersion, the denominator simplifies to $(1 - \frac{1}{M})$. We have also utilized the reasonable approximation that

$$L_{T_e} = L_{T_i}$$

We are generally interested, for our plasmas, in the limit of small M. The opposite is true for pellet physics. For M<<1,

$$k_a' = \frac{-k_a}{2} \, , \frac{\left[\frac{1}{L_T}\left(1 - \frac{\Omega_e}{2\sqrt{\pi}kv_{Te}}\right) + k^2\lambda_{De}^2 \frac{1}{L_n} + \frac{\Omega_e}{\sqrt{\pi}kv_{Te}L_B}\right]}{\left[1 - \frac{3}{2}\frac{\Omega_e}{\sqrt{\pi}kv_{Te}}\right]} \qquad \text{(I-16)}$$

The importance of the magnetic field term in the denominator is felt especially for cool plasmas. To obtain the pulse shift gradient, which is the parameter relevant for convective growth, we use

$$K' = \frac{-k_o}{L_n}\frac{\omega_p^2}{\omega_o^2} - k_a' \qquad \text{(I-17)}$$

The first term is due to wavelength alteration of the incident and reflected electromagnetic waves, which are affected approximately equally.

The magnetic field is seen to affect stimulated scattering in a number of ways. First of all, the process is affected by alteration of the acoustic frequency for strong fields. This increases the redshift as well as decreases the homogeneous growth rate. Secondly, electron Landau damping is altered considerably, depending upon angle and field strength. For very small angles between the incident wavevector and $\perp\overline{B}$ the damping decreases with the application of stronger fields. Thirdly, the magnetic field affects the phase mismatch by altering the dispersion relation in a non-cancelling manner. We will compare the predictions of this theory with the results of our experiments.

I.C. The Experiment

1. Experimental Design

The experimental arrangement is shown schematically in Fig.(I-5)[5]. The basic components indicated are the high power carbon dioxide laser, the Cassegrainian focusing system, the d.c. solenoid, the plasma chamber with auxiliary equipment, and the detection and diagnostic apparatus.

The pulsed CO_2 laser is a transversely excited atmospheric pressure Lumonics model 621. The optical configuration is that of an unstable resonator, producing a divergence angle of approximately .15 milliradians. The output optic is a 12" diameter salt window, allowing the passage of a beam of unfocussed diameter of more than nine inches. The method of excitation was that of preionization via flashboard along with four stage Marx bank capacitor discharge, producing a 50-60 nsec spike followed by a microsecond long tail. This tail contained about two-thirds of the total energy of the pulse or about 200 joules, with 100 joules in the gain-switched spike. The peak power was approximately 1500-2000 MW, depending upon self-modelocking conditions. Modelocking was found to be important, and typically was in the range of 10-30%, subject to variation from shot to shot. The spikes on the output pulse that resulted from such modelocking were spaced about 5 nsec apart consistent with competition of longitudinal modes. Part of the beam was monitored to observe this temporal behavior. Photon drag detection traces of the pulse are shown in Figs.(I-6)-(I-7). Shot-to-shot variation was quite dramatic, and served to complicate the analysis. Also, the annular beam intensity varied somewhat spatially. On the average, the energy density of the beam was approximately 2 joules/cm^2. In all cases, however, the laser fired on the strongest line, the P(20) of

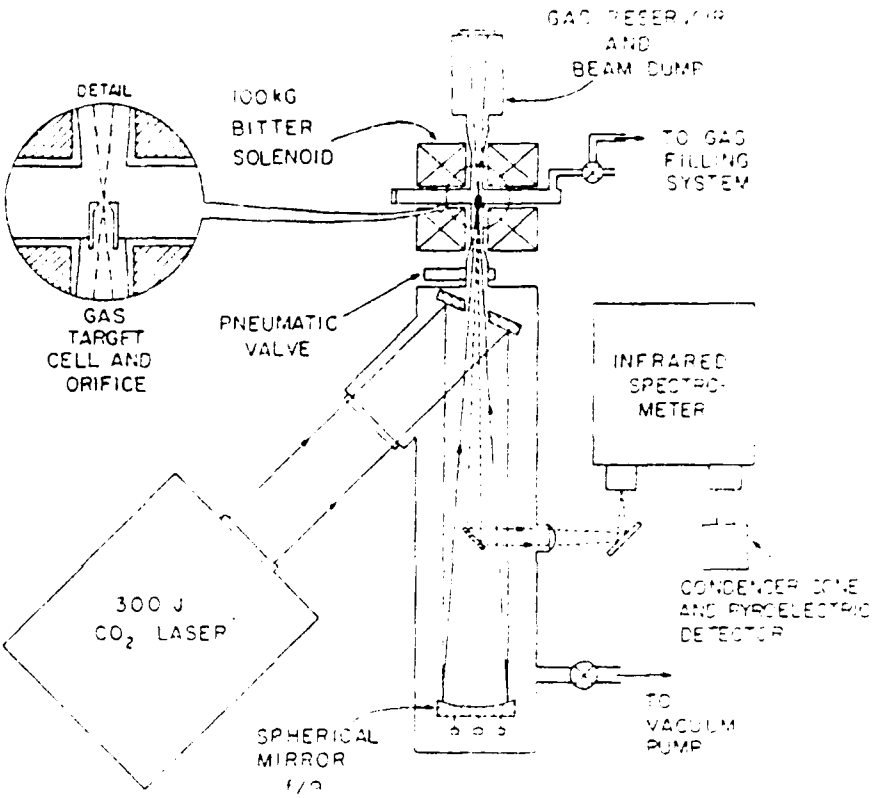

Fig. I-5 Experimental set-up. The magnetic field direction is horizontal in this diagram. The insert at upper left indicates the geometry of the focal region appropriate to gas target studies. Figure (I-8) indicates the difference in focal geometry for solid targets.

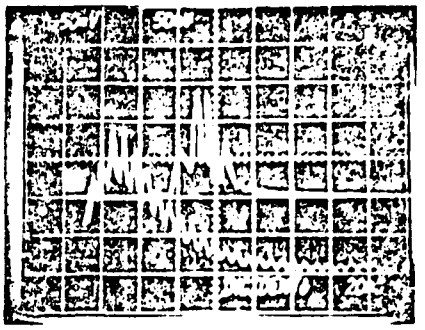

Backscattered radiation (upper trace)
from helium plasma at 5 T.

Fig. I-6 Upper trace marks response of photon drag detector to wavelength unanalyzed backscattered radiation from helium spark. Lower trace marks incident. Delay of 43 nsec is due to photon time-of-flight.

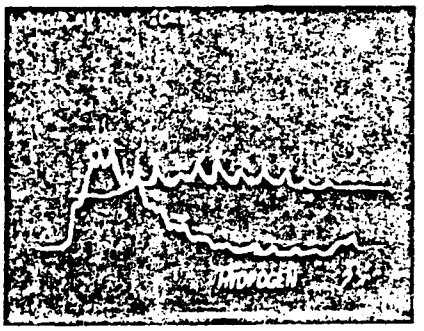

Backscattered radiation (upper trace)
from hydrogen plasma at 2.5 T.

Fig. I-7 Response of photon drag detectors to both backscatter (upper) and incident (lower) from hydrogen. Although plasma response differs between hydrogen and helium, the self-modulated pattern is reflected in the backscatter in both Figs. (I-6) and (I-7).

the 001-100 band of the CO_2 molecule. The vacuum wavelength for this line has been shown to be 105,910 Å and the air wavelength 105,382 Å.

The magnet used to generate the field in the experiment was a Bitter solenoid, water-cooled at room temperature, capable of a 10 Telsa field constant in time. The 2-1/8" diameter bore of the solenoid was accessible not only by its ends, but also through four rectangular (5/8"x2") ports, giving radial access to the center of the magnet. Due to stringent spatial requirements in magnet design, the aluminum jacket surrounding the copper solenoid had to be electrically floated, requiring that it be isolated from other parts of the experiment. Field quality was quite high, with less than a 5% inhomogeneity over the region of interest throughout the tunable range (0-10 Telsa) of the solenoid. Most of the inhomogeneity that was present was due to a central minimum of the field strength, since the necessity of the radial access ports required that the magnet be expanded beyond the centrally homogeneous design.

The solenoid contained the plasma chamber, which was mated to an evacuated Cassegrainian focusing system for the incoming laser beam. The geometry of the solenoid required a focusing mirror of two meter focal length since the beam area is large, resulting in approximately f/9 optics for the Cassegrainian system. The entrance window to the focusing system was another 12" salt; the internal optics were two oxygen-free copper mirrors, both of 10" diameter, one the 2 meter focusing spherical mirror, the other having a 2-1/2" diamter hole, offset from normal by 22.5°, permitting the passage of the focused beam out of the Cassegrainian system and into the target area, as indicated in Fig.(I-8).

The focusing system is connected, via continuous vacuum, to the plasma chamber inside the solenoid. The apparatus we have been referring to as

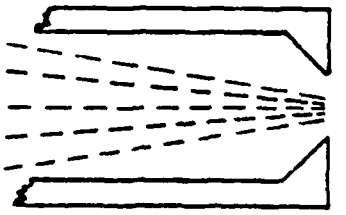

GAS TARGET

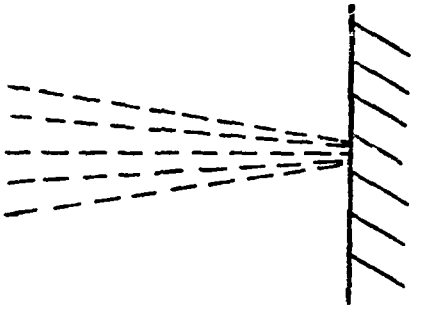

SOLID TARGET

Fig. I-1 Top diagram indicates geometry of gas target focus. Gas streams from right to left through nozzle. Breakdown plasma forms approximately at the point where nozzle begins to narrow. Bottom diagram indicates laser incidence on solid slab targets.

the plasma chamber is actually composed of four sections, with the main plasma located in only one, the orifice region. This section is the part of the chamber in the very center of the solenoid, and consists of an orifice of approximately 3 mm diameter at the end of a short (5/8" length) 3/8" diameter brass pipe. Upstream, that is, toward the laser, from the orifice is the section of the plasma chamber connecting the orifice region to the Cassegrainian focusing system. This section, referred to subsequently as the convergence section, is essentially conically shaped, with the small end at the orifice. The opposite end is separated from the focusing system by a pneumatically operated gate valve, the importance and operation of which will be described subsequently.

Downstream from the orifice is the beam dump and gas reservoir. This section fulfilled this twofold purpose: to provide a method of channeling transmitted laser radiation out of the system, and to provide a large volume of gas at fill pressure for the fast valve operation, as described below. One of the configurations utilized included a 4" diameter salt which permitted the measurement of transmitted laser power through the plasma. In the absence of plasma formation, this salt was close enough to the focus to permit the transmission of the entire beam through the system. This is true upon consideration of geometric optics. No such measurement was possible, since the pumping was via mechanical vacuum pumps only. Sufficiently low pressure then, could not be achieved to avoid breakdown due to the high power density in the focus spot.

The remaining section of the "plasma chamber" served the practical purpose of maintaining and monitoring pressure in the reaction cell. The equipment utilized included a solenoid and needle valve combination for gas filling, absolute and thermocouple pressure gauges, an absolute pressure switch, and electronics for the regulation of the filling.

The pulsed operation of the system is as follows. The pneumatic gate valve forming the boundary between the evacuated Cassegrainian focusing system and the convergence section opens, taking a few tenths of a second to rise completely, during which time the volume of the convergence section is completely evacuated. The gas reservoir downstream from the orifice maintains pressure, causing the formation of a density step in the orifice region. The steep density gradient, parallel to the laser beam, is necessary to eliminate an ionization front which would otherwise move back toward the laser, scattering radiation away from the focus region.

When the gate valve reaches the apex of its cycle, the laser is automatically triggered to fire and the breakdown plasma forms. The same pulse which triggers laser operation also triggers the closing of the gate valve. The pressure switch and gas filling system then automatically raise the pressure in the plasma chamber back to the previous fill pressure, and the system is made ready for the next shot. This method of "puff evacuating" has been shown to be effective in providing a sufficient density gradient at the orifice for the elimination of the backwards moving ionization front. Other researchers, for instance Offenburger, et al.,[6] have used similar methods.

Since the spatial structure of the beam from the unstable resonator is annular, the backscattered radiation is collected by a small front-surface mirror mounted in the center of the beam path, approximately one meter from the focus. This mirror deflects the scattered radiation out of the vacuum system via a ZnSe lens, which focuses the radiation onto the entrance slit of a 3/4-meter Czerny-Turner spectrometer. This monochromator has a grating of 150 lines/mm appropriate to the 10.6 μm wavelength of the CO_2 laser.

Mounted at the exit slit is a pyroelectric detector behind a brass condenser cone. The output of the detector is read on an oscilloscope or by means of a peakreading voltmeter plus chart recorder combination. A wavelength scan consists of taking shots at various settings of the spectrometer. Because of variation in the laser output from shot-to-shot, and of consequent variation of plasma response, several shots had to be taken at each setting. Alternatively, the whole wavelength-integrated backscatter was observed by a fast photon drag detector and oscilloscope or by a time-integrating energy meter.

Signal levels from the pyroelectric detector were always sufficiently high to permit the narrowing of the spectrometer slits to the point that the resulting bandpass did not much exceed the theoretical resolving power of the grating (approximately 7 Å). As will be seen, the sharpness of the resulting spectra attest to the credibility of such small (8-15 Å typically) bandpasses.

2. Experimental Results

The experimental arrangement permitted the analysis of incident and backscattered radiation in three ways. First of all, time-integrated spectral analysis was done on the backscattered radiation by means of the monochromator and pyroelectric detector. Secondly, the temporal behavior of the spectrally integrated backscatter had sufficient power to be observed with a photon-drag detector. This unanalyzed radiation was also lead into a calorimeter to observe the field dependence of the total backscatter. Thirdly, transmission through the plasma of the incident carbon dioxide radiation was observed as a function of field strength.

Plasma conditions were inferred principally from the magnetic field strength and breakdown material and from the backscattering spectra. The initial density and atomic number (Z_o) of the fill gas determined how efficiently the laser radiation was absorbed. The ionization state reached (Z, Z_{eff}) and the ionic mass number (μ) were found to have a strong effect on the temperature attained and expansion of the plasma out of the focal region. For instance, although the electron density of normal hydrogen is the same as that for deuterium and for helium at the same fill pressure, and the laser pump is capable of completely stripping the ions in each case, the observed values of the temperatures from the backscatter spectra were found to be highest for the helium ($Z = 2$, $\mu = 4$), followed by deuterium ($Z = 1$, $\mu = 2$), with hydrogen the coolest ($Z = \mu = 1$). This measurement of the "temperature" ($Z_{eff}T_e + 3T_i$) was further substantiated by photon drag detector traces of the wavelength unanalyzed backscatter, which revealed a lower threshold, but also lower maximum amplitude for hydrogen than for helium. This is consistent with backscatter in the convective mode. Table (I-1) lists typical values at plasma parameters for helium plasmas.

The temporal behavior of the output of the CO_2 laser varied from shot to shot, principally by means of mode competition. Typically one longitudinal mode gave roughly 80% of the output energy, presumably the fundamental mode, with the rest coming from one or a few of the higher modes. The laser output was then an envelope consisting of spike and tail characteristic of the gain-switched laser with a series of mode-locked spikes appearing on top of it. The spacing of these spikes was about 5-6 nsec, as is clear from the oscilloscope traces (see Figs. (I-5) and (I-6)). Since the mirror spacing is approximately 165 cm, this is consistent with the simple type of modelocking described by Yariv[7] with the peak spacing $\tau = \frac{1}{n}\cdot\frac{2L}{C}$.

Plasma Parameters in Helium

Lengths (cm)		
electron Debye length	λ_{De}	3.5×10^{-6}
ion Debye length	λ_{Di}	1.5×10^{-6}
electron gyroradius	ρ_e	1.3×10^{-4}
ion gyroradius	ρ_i	3.5×10^{-3}
acoustic wavelength	λ_s	5.3×10^{-4}
laser wavelength	λ_o	1.06×10^{-3}
Speeds (cm/sec)		
electron thermal speed	$\frac{K_B T_e}{M_e}$	2.4×10^{8}
ion thermal speed	$\frac{K_B T_i}{M_i}$	1.7×10^{6}
ion acoustic speed	c_s	5.3×10^{6}
Frequencies (sec^{-1})		
laser frequency	ω_o	1.8×10^{14}
acoustic frequency	ω_s	6.3×10^{10}
electron frequency	Ω_e	1.8×10^{12}
ion gyrofrequency	Ω_i	4.8×10^{8}
Landau damping rate	λ	6.2×10^{9}
collisional damping rate	ν_{ei}	5×10^{7}
electron plasma frequency	ω_{pe}	4.8×10^{13}
ion plasma frequency	ω_{pi}	1.1×10^{12}
e-i equilibration rate	ν_{ei}	5×10^{7}

Table I-1. Table indicates values of certain parameters relevant to the experimental situation. Values shown are those for helium breakdown plasmas, which are representative of the midrange of our experiments. The field strength is taken to be near its maximum of 10T.

The lower trace on the two photographs is the output of a photon drag detector observing a portion of the incident beam. The upper trace is the wavelength unanalyzed backscatter. A delay of about 42 nanoseconds by which the upper trace follows the lower is due to the photon time of flight and consists of about seven nanoseconds delay for backscatter to reach the detector from the plasma with the remaining time for the incident laser radiation to reach the plasma from the incident-viewing detector.

From the observation of a large number of events, it becomes clear that the temporal structure of the backscatter followed that of the incident in a general way. This can be realized upon examination of the sample events given in Figs. (I-6) and (I-7). Figure (I-6) is from a helium plasma event. Note that the modelocking pattern of the incident is mimicked by the temporal behavior of the backscatter, allowing for some alteration of the amplification mechanism through changing plasma conditions. As will be treated in the analysis chapter, one of the more significant of these is the electron-ion temperature equilibration.

Figure (I-7), on the other hand, pictures the temporal behavior of radiation from a hydrogen plasma. Note that the backscatter, while still mimicking the peaks of the incident, has much less amplitude and longer duration. These are explainable by alteration of convective amplitude amplification and convective threshold, respectively.

Field strength dependence of the appearance of the photon drag traces was weak. As has been pointed out in Section I.B., the presence of the magnetic field does alter the growth rate, threshold, and final convective amplitudes attained. However, the presence of the field was found not to alter essentially the above outlined temporal behavior for all fields not

too strong ($k\lambda_e > 1$), and provided, of course, that the convective threshold was still reached.

Spectra were obtained for backscattered radiation reflected into the annular hole of the unstable resonator beam pattern. Conditions of the plasma affected profoundly the character of the spectrum. In general, peak power was observed to be redshifted from the wavelength of the incident radiation. The response of our instrumentation to this incident is plotted in Fig. (I-9). The width of the spectrum, approximately 5 Å is due almost entirely to instrument broadening, and corresponds roughly to the theoretical estimate of the 150 groove/mm grating resolution. Actually, lasers of this type have a linewidth of about one angstrom (300 MHz). Therefore, the spectrum in Fig. (I-9) serves not only to calibrate with high accuracy the spectrometer in the region of interest, but also displays instrumental response to a nearly δ-function stimulus.

Sample spectra are displayed in Figs. (I-10) and (I-11). Both are taken from helium plasmas, at a 10 torr cell fill pressure. The experimental difference between the two is that, while Fig. (I-10) displays the spectrum obtained from a field-free configuration, Fig. (I-11) corresponds to the application of a 9.0 Tesla magnetic field, directed perpendicularly to the direction of laser propagation. Note that both spectra contain a peak shifted to the red of the incident indicated by the dashed line.

Several noteworthy differences between the spectra indicate variation in their causal physical process. First of all, the presence of the strong transverse field increases the redshift of the peak. According to the derivations in the theoretical section of this chapter, this could correspond to a heating of electrons or ions, as well as a direct contribution by magnetic effects on the plasma dispersion.

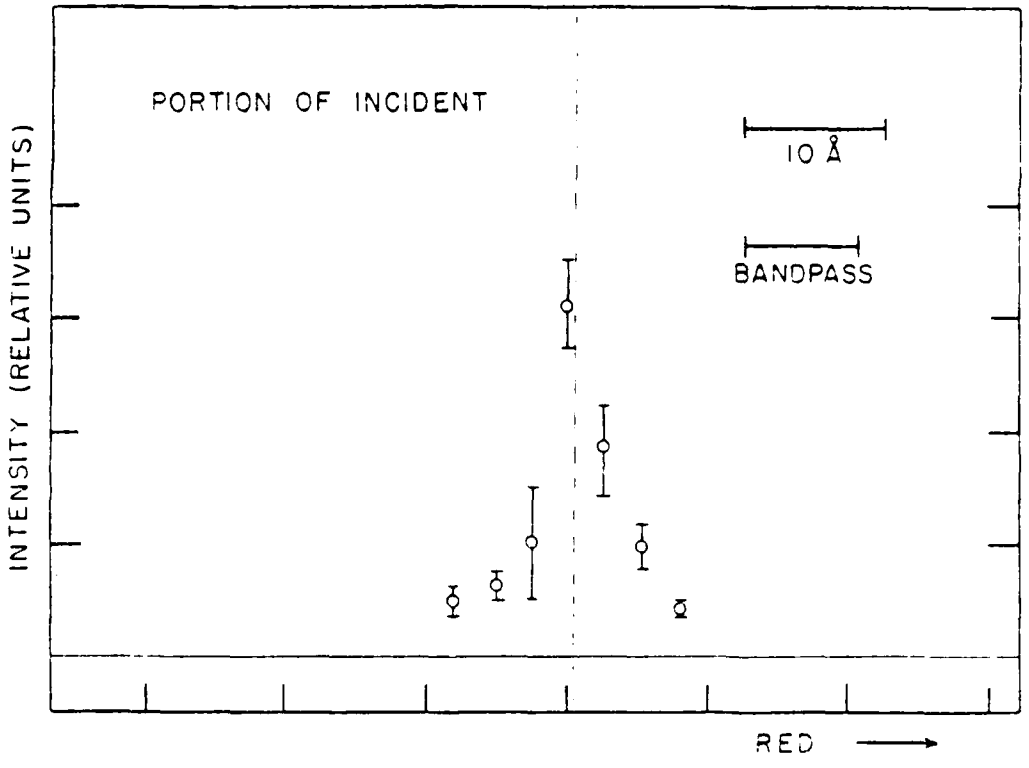

Fig. I-9 Spectrum indicates response of the instrumentation to the incident radiation, which appears as a narrow spike in relation to the bandpass. The bandpass here indicated is approximately the grating limit. The dotted line indicates what has been taken as the λ_o reference in all subsequent spectra.

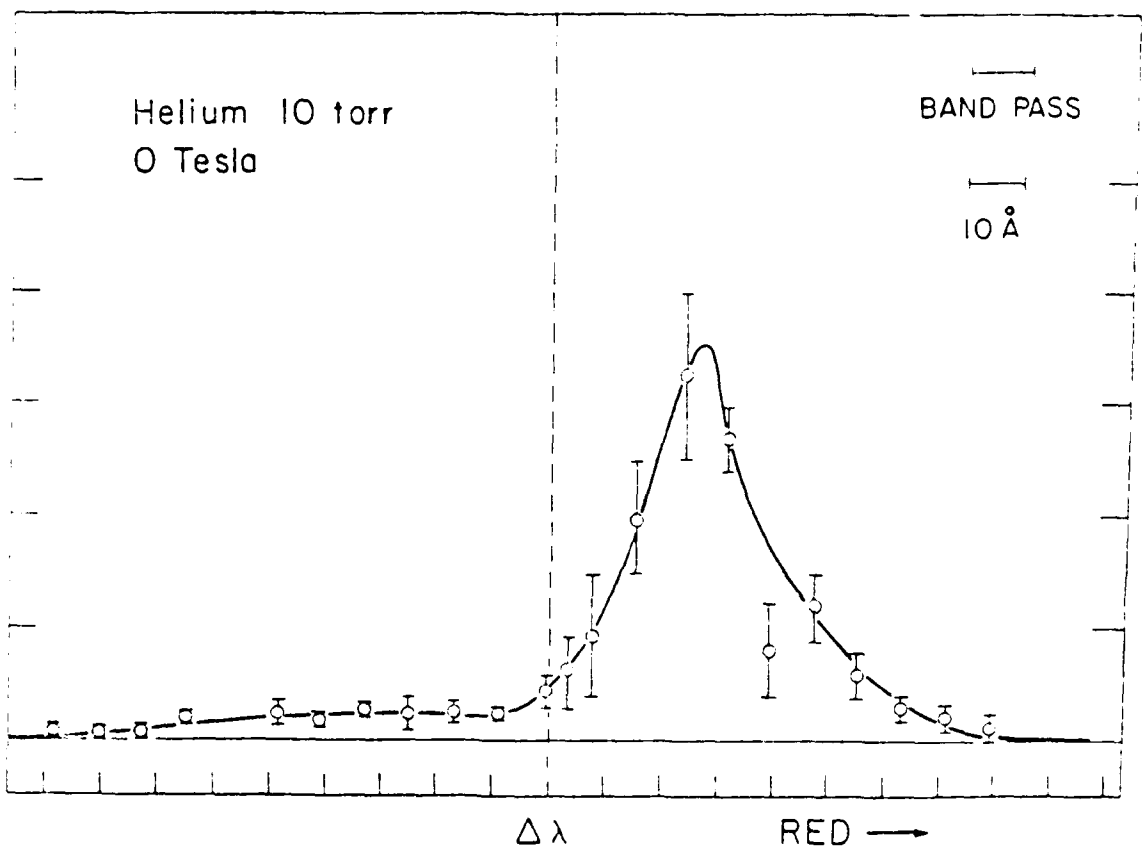

Fig. I-10 Temporally integrated backscatter spectrum from neon at a fill pressure of 10 Torr and no magnetic field. Dotted line indicates the unshifted wavelength, $\lambda_0 = 10.59$ μm.

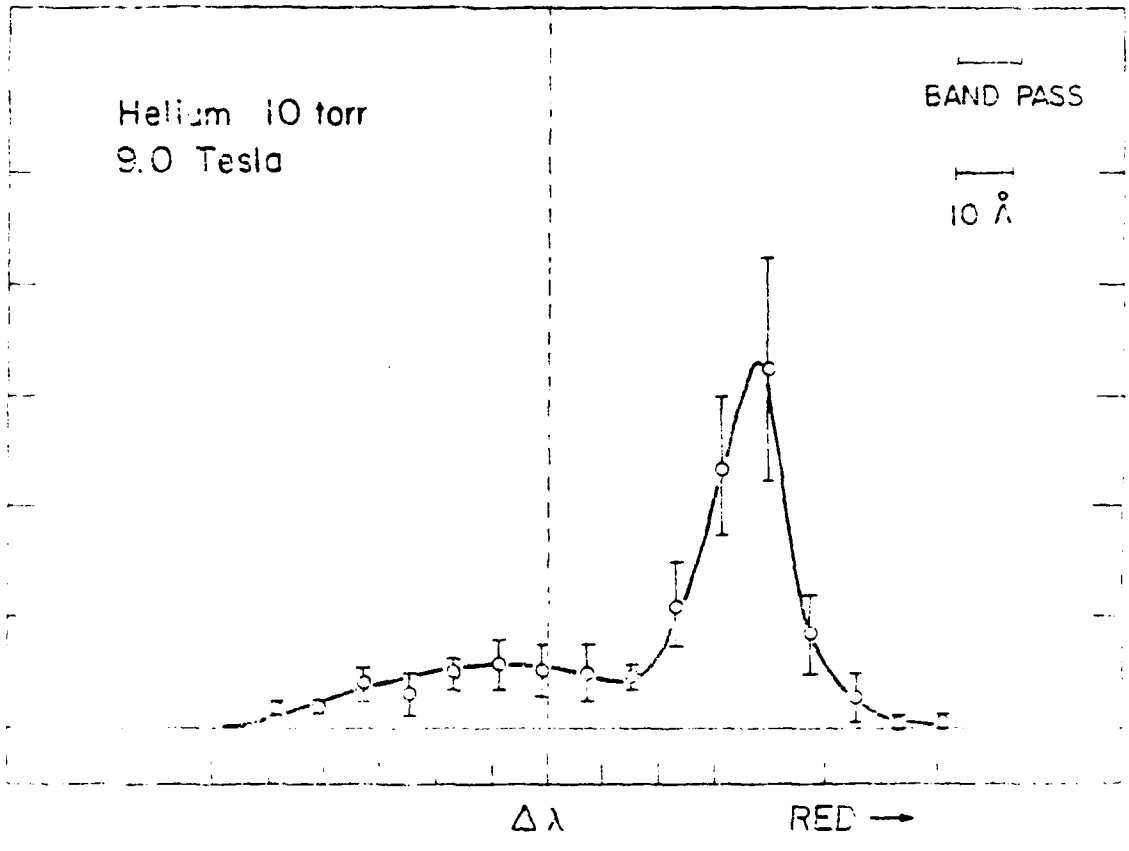

Fig. 7-11 Temporally integrated backscatter spectrum from a film at a pressure of 10 Torr and a strong (2T) magnetic field. Dotted line is the unshifted wavelength, $\lambda_o = 10.59$ μm.

A second effect of the applied field is the substantial line narrowing that occurs. Several mechanisms could contribute to this process, both directly kinetic ones, such as a decrease in the Landau damping rate with increase in field (which was found analytically to occur for small off-perpendicular angles), and more macroscopic mechanisms, such as a change in the number of scattering centers, spanning a temperature range for low fields. The wavelength shift increases and the full width at half maximum of the peak decreases steadily with increasing field strength above 5 T.

A final conspicuous characteristic of the helium spectra is the presence of broadband low-level blue-shifted radiation for the high field plasmas. This blue shift turned on at about 5 T, and increased with the field strength. A likely candidate for a mechanism is a simple Doppler shift from a plasma expanding toward the laser, either by dielectric reflection or by stimulated scattering. The presence of a negative energy wave in a stationary plasma has been ruled out analytically. No appropriate solution can be found for plasmas with the given characteristics.

Spectra were taken of backscatter from plasma created from various gas targets; ordinary hydrogen at 10 and 20 torr fill pressure, nitrogen and deuterium at 10 torr, and methane at 2.5 torr. Spectra were also taken at various field strengths from a plasma formed from a slab target of teflon (C-F polymer). These provided plasmas of a range of ion and electron temperatures and densities, as well as enormously different scale length structures in the case of the slab target plasmas. Due to more efficient laser absorption, electron temperatures were found to be higher for the breakdown plasmas with higher electron densities. Temperature increase was also noted with increase in ionic mass, since the plasma expansion was slower.

No appreciable backscatter or reflection was observed for the case of 10 torr argon fill at any applied perpendicular field strength, presumably because the temperature was too high.

The threshold power for homogeneous growth,

$$\frac{v_{oT}^2}{c^2} \propto \frac{\gamma_2 \gamma_a}{n_i} \sqrt{\frac{A}{Z^2}(ZT_e + 3T_i)} \qquad (I-18)$$

has roughly direct proportionality with the square root of the plasma temperature, but is also weakly dependent upon the magnetic field strength through γ_a and ω_a, the damping rate going either up or down with field strength depending upon angle, and the wave frequency increasing with the field. The homogeneous growth rate, which affects the convective growth amplitude, behaves similarly. It was therefore instructive to study the dependence of the wavelength unanalyzed backscatter on field strength.

Especially interesting is the case of nitrogen. Because of the high value of the acoustic frequency, ω_a, for nitrogen, the threshold for convective growth was high. Alteration of the field strongly affected the total backscatter, as indicated in Fig. (I-12). Interestingly, the transmission through the plasma (6° cone) was found to have an inverse type of behavior, seeming to approach asymptotically a maximum as the backscatter fell to zero, as indicated in the same figure. The graph indicates only relative units; the total transmission was small, approximately 3 Joules maximum. This is transmission into a 6° cone.

The total backscattered energy was never measured directly, due to the unavailability of a beam-splitter of appropriate dimensions. However, we do know the strength of the backscatter at the interior edge of the laser beam, and by this we can make a rough inference of the total, assuming

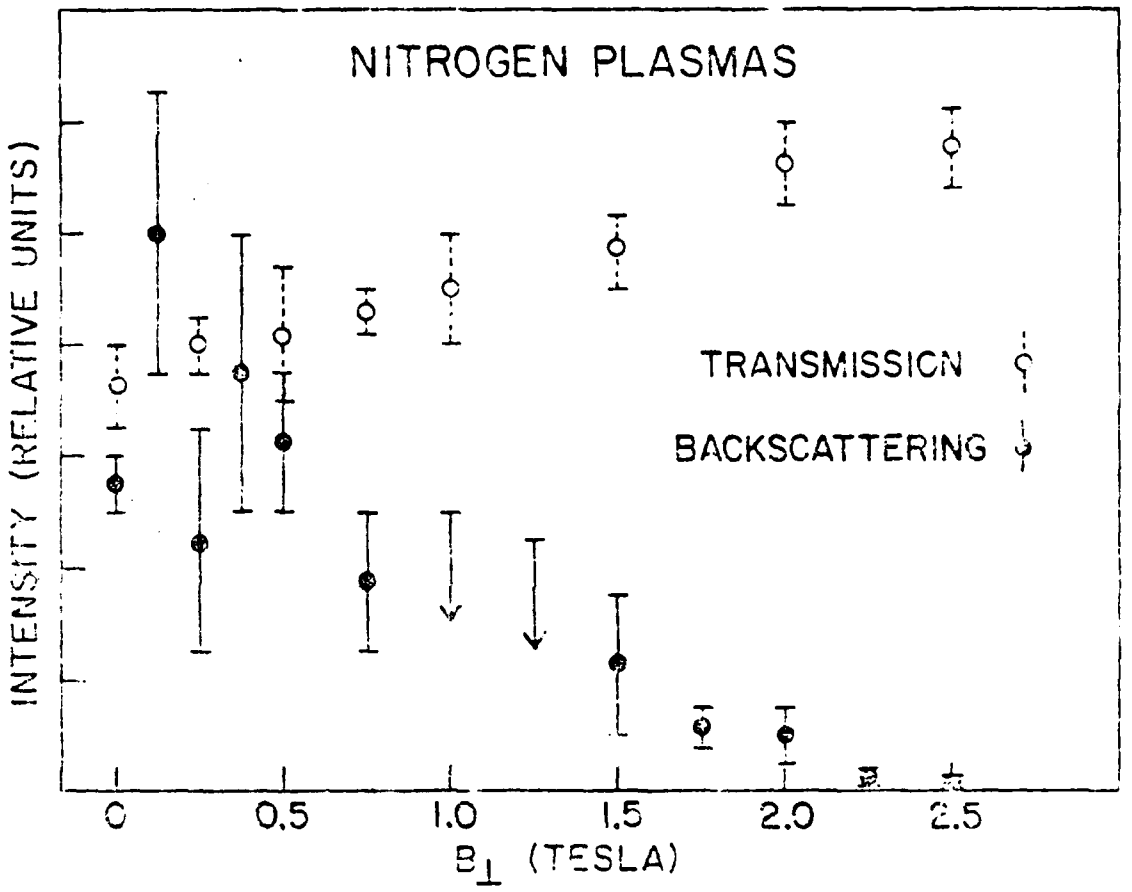

Fig. I-12 Wavelength unmodified backscatter from and transmission through nitrogen plasma at 10 torr fill. Units are relative and independent for transmission and backscatter. Transmission is all radiation [illegible] through a 6° forward cone. Note complimentary rise and fall of [illegible] with field increase.

that the profile does not vary too greatly over the beam. Using this procedure, we can say that probably not less than 5% of the power is backscattered and not more than 15 or 20%. In almost all cases (having to do with various plasma setup parameters), the backscatter appears to fall in the range of 5-10%.

The transmission through hydrogen was found also to increase for the strong fields. Measurements show a rise beginning at 5 T and reaching a maximum at about 7.0-7.5 T. There are several possible candidates for a mechanism, and there may be more than one at work. It will suffice here to note that, with the electron temperature obtained from the shift and crudely by other means, the factor $k\rho_e \tilde{} 1$ for this field regime, that is, the gyroradius is about equal to the magneto acoustic wavelength. At very strong fields the spectrum undergoes a considerable alteration for hydrogen, including an apparently linear increase in amplitude with shift until a maximum, followed by a very sudden drop. Although clear and reproducible data for wavelength unanalyzed backscatter with field strength variation does not exist, it was noted that for very strong fields (above 7 T), the total backscatter amplitude fell precipitously.

I.D. Analysis

1. Interpretation of spectral widths

Various effects can be at work to generate a backscatter spectrum of the measured widths. Since we observe an almost universal narrowing of the red-shifted peak with increasing field strength, and the Landau damping rate has been shown to decrease with increasing field for our laser incidence angle, we expect that a large portion of the width is due to line broadening by damping of the generated wave. Not only is the electrostatic wave

affected, but the collisional damping of the backscattered electromagnetic wave is changed indirectly by application of the field, since the plasma temperature is seen to vary somewhat. Since this damping is much smaller, however, ($\gamma_l \ll \gamma_a$) the growth rate above threshold is affected only slightly, but the threshold power is proportional to the product $\gamma_l \gamma_a$.

We have developed a computer program which generates the backscatter spectrum predicted by the theory. Inputs are bulk plasma conditions of electron and ion temperatures, density, magnetic field strength, scale lengths, laser incidence angle, and laser focussed power. The program calculates wave frequency and magnetoacoustic damping rate, and then calculates the homogenous growth rate as a function of frequency mismatch. It then considers convective amplification, using the expression for the wave number mismatch gradient that we have developed. The backscattered spectrum is then displayed graphically.

A sample of this calculated spectrum is given in Fig. (I-13). This gives the predicted shift and lineshape. Note that the line is completely symmetrical about linecenter, as is this theory. The lineshape is not any simple analytic form, such as a Gaussian or Lorentzian. However, the curve is expressible in closed analytic form, although it is uninstructive and tedious to do so. In this case, the program predicts fairly well the experimentally observed backscatter for strong field helium plasma. Instrumental broadening of the peak is of the order of 8-10 Å. However, the predicted amplitude of the backscatter varies far more wildly with field strength than was observed experimentally.

Nevertheless, the narrowing of the spectrum which occurs in nearly all cases studied, is pronounced in helium, and especially pronounced in nitrogen,

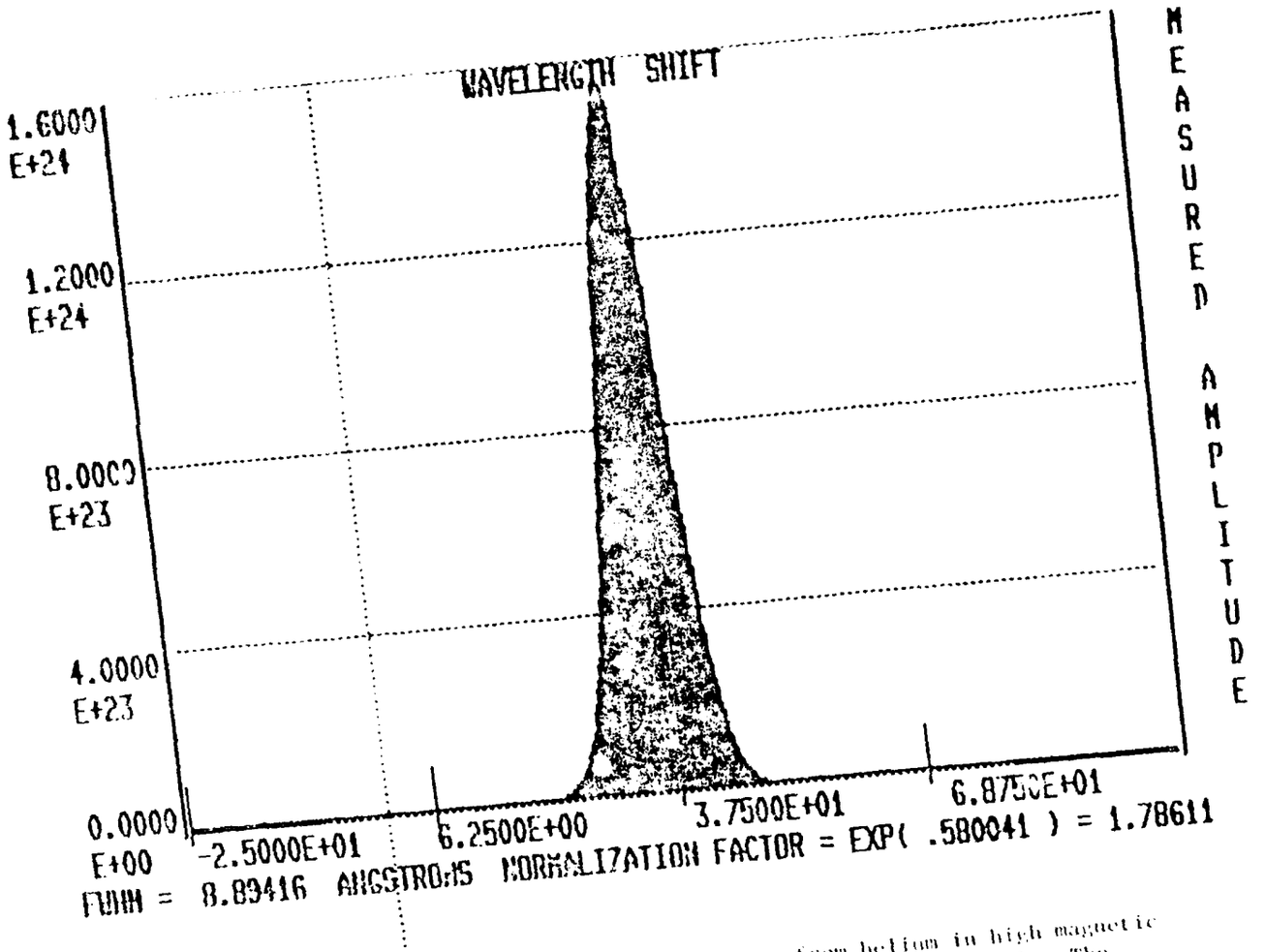

Fig. I-11 Theoretical backscatter spectrum from helium in high magnetic
ti ld (9T). Assumed temperatures are T_e = 32 eV and T_i = 10 eV. The
an,le of k i, taken as 0.20 from the perpendicular to $\vec{B}$.

points to the decrease of the Landau damping rate as a possible explanation. However, other factors which contribute to the width could also be decreasing with increase in field. In particular, increase in the field results in decreased expansion of the plasma toward the laser, steepening the density gradient. Besides reducing convective growth (thereby competing with the decreased damping effect, which promotes growth), this effect also reduces the possibility of multiple scattering centers. The existence of these multiple centers, each with its own set of plasma parameters, has been cited as a contributing factor to the experimentally observed width of a backscatter spectrum.[8] The resulting spectrum in that case should be viewed as a superposition of contributions from the various centers. Moreover, if conditions are not too different for two such centers, the wave generated from one may stimulate the instability in another, or increase its growth, in much the way that a single wave grows convectively.

The three major causes of spectral width cited here, damping of daughter waves, multiple scattering centers, and instrumental broadening, all seem unfortunately, to be of the same order of magnitude. It is also impossible to distinguish between the effect of damping and of multiple centers without being able to vary plasma conditions at will. We have that capability in the adjustment of magnetic field strength, but even there a limitation exists. For the hotter plasmas at low field strength, plasma β is high, thereby effectively excluding the magnetic field from the scattering center. This apparently is the reason for so little change in helium backscattering spectra for fields below 5T. Beyond that level, $\beta < 1$, so that the field is achieved beyond the scattering center. In the case of the hotter nitrogen, the field probably acts almost totally to cut off the effect of multiple

scattering centers. The spectrum from a 2.5T nitrogen breakdown, then, is expected to exhibit a purely Landau-damping broadened scattering event. (See Fig. (I-14).) The calculated damping contribution is minimal, however, so the spectrum should appear as a δ-function being observed by our relatively wide bandpass. The spectrum in Fig. (I-14) does indeed appear that way.

Close correspondence between this simple theory and experiment is not achieved universally, and only for the magnetized cases. The suspected reason for this is, again, the existence of multiple scattering centers which is not treated by the theory, and whose number presumably decreases with increasing field.

Allowing for instrument broadening, fairly close correspondence between prediction and experiment is achieved for strong fields in helium breakdowns. Nitrogen backscatter turns off in high magnetic fields, presumably due to increase of α_s with magnetic field (both directly and via heating) so that correspondence with theory cannot be demonstrated over a range of field strength, as is possible with helium. Also, the very low wave damping in nitrogen plasmas puts the real value of the spectral width too narrow to be resolved with our apparatus. Argon breakdowns were too hot to give any backscatter. Spectral alterations in the hydrogen isotope plasmas complicate the analysis here, especially for high field strengths.

Strong field helium plasma then, is the only material whose experimentally observed conditions permit comparison with the simple theory. One must take into account the decrease of magnetic field in the scattering center (about 5T subtraction for the stronger fields) as well as instrument broadening. These two numbers are not well known, one because of the

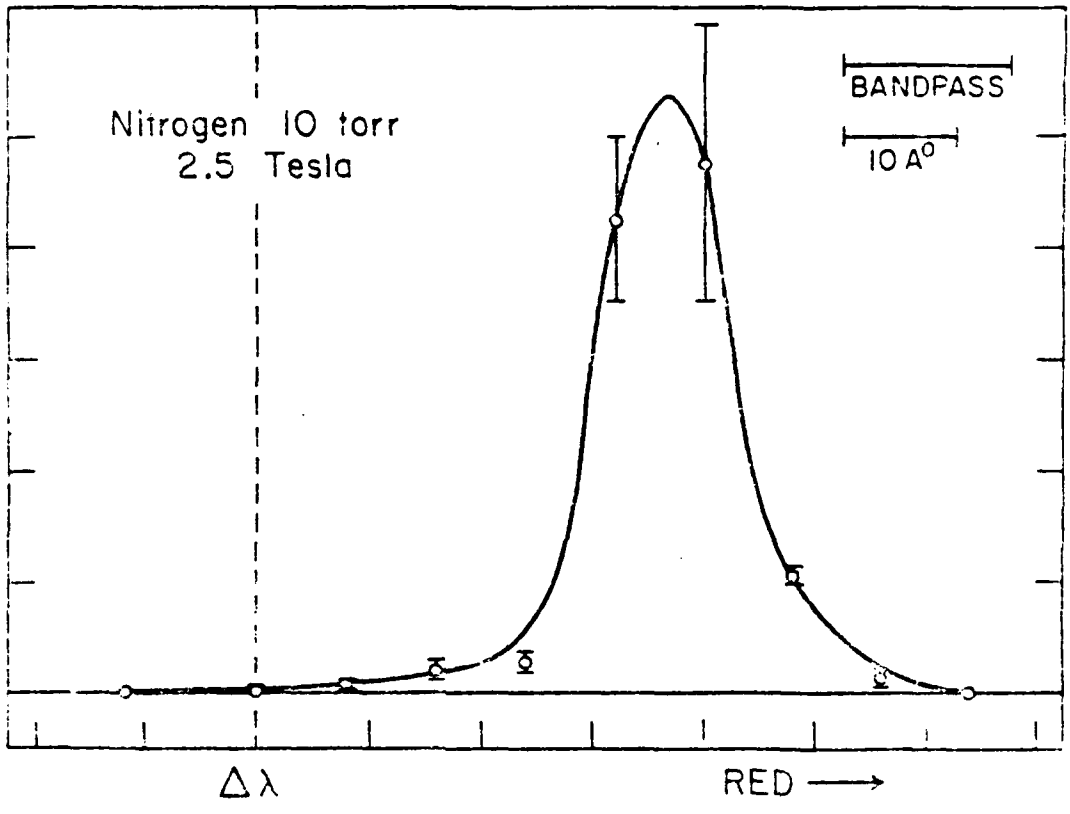

Fig. 3-14. Backscatter spectrum from nitrogen breakdown plasma at 10 torr fill pressure. Dashed line indicates incident wavelength at 10.5 μm.

impossibility of using magnetic probes in the plasma, and the other because rigid requirements of deconvolution are not met by this experiment. Yet, for reasonable estimates (ω value exclusion and bandpass width increase) the general field dependence of γ/ω is demonstrated by the narrowing of the backscatter spectral width for strong field helium. The approach of the experimental results to the simple theory just described is illustrated in Fig. (I-15). The difference between the experimental points and the calculated ones is far greater for the low values of magnetic field than for high. The dramatic approach of these two curves is due, presumably, to the exclusion of multiple scattering centers by the strong transverse field.

2. Conclusions

It has been shown that the red-shifted Brillouin peak has a width dependent upon plasma parameters. This width decreases with increasing field strength for a wide range of transverse magnetic field values and auxiliary plasma parameters. Various mechanisms have been proposed to account for this phenomenon. Most interesting, it has been shown analytically that the magnetic field directly alters both the real and imaginary parts of the frequency of a nearly free longitudinal wave moving across the field. It has been suggested that the change in the Landau damping rate of the stimulated wave directly by the magnetic field is primarily responsible for the width decrease in scattering off strong field helium plasmas. For nitrogen plasmas, the spectrum does not disagree with the application of the same theory, but due to the low value of the damping rate and the proximity to threshold, demonstration is inconclusive.

Scattering from hydrogen isotope plasmas has given a characteristic SBS redshift, but the spectrum undergoes alteration with the application of a

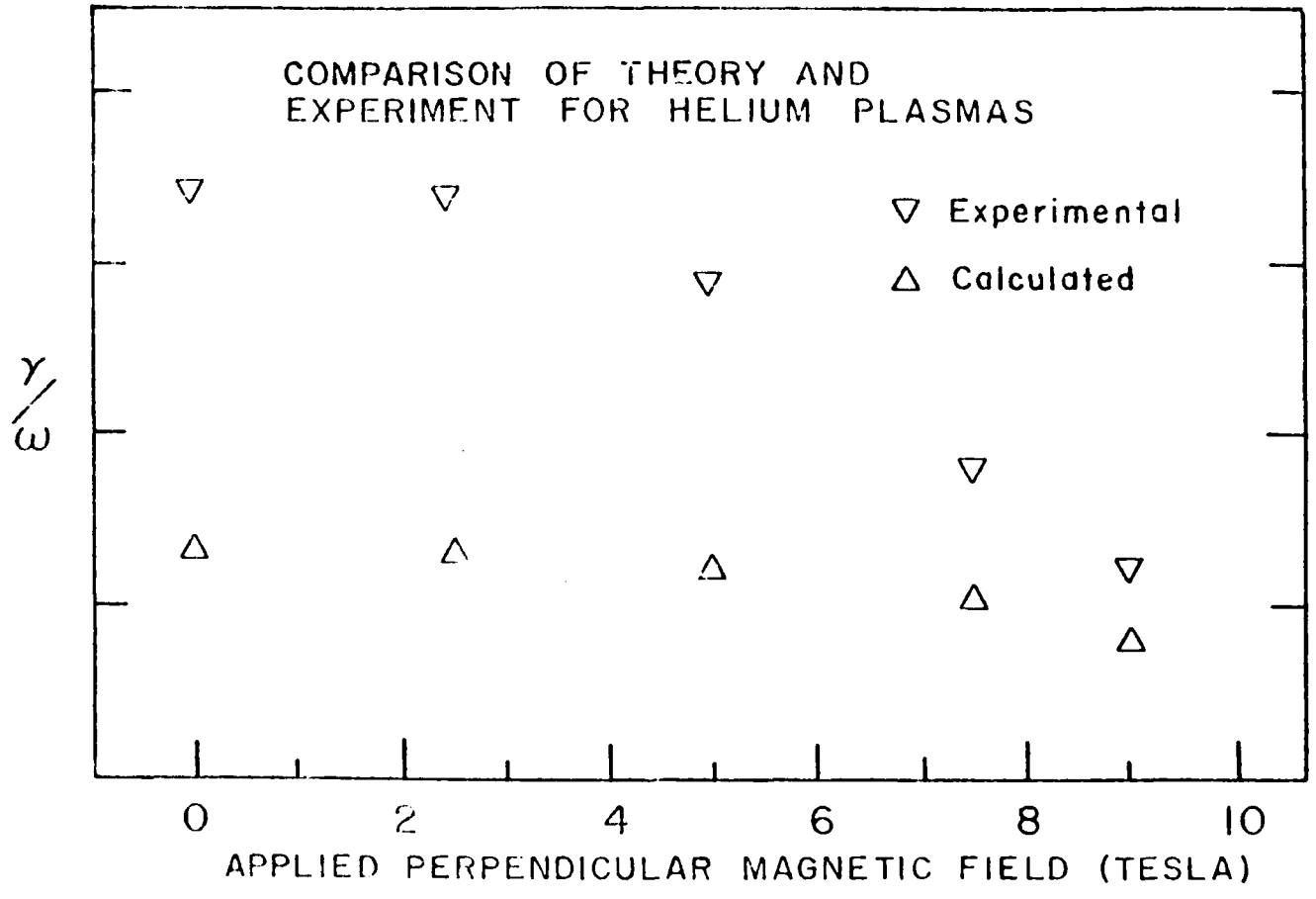

Fig. 6-5 Comparison of measured and theoretical damping coefficients. The measured values are unfolded from the experimental widths of the backscattered radiation. The greater apparent damping at low fields in the experiment may be caused by the presence of multiple scattering centers.

very strong field. The exact cause of this alteration is not understood; however, the condition of $k\lambda_e \approx 1$ is met at this point. Transmission studies support the validity of the assumption of a qualitative change in the scattering phenomenon taking place.

It has been shown analytically that the real wave frequency is increased by application of the strong field. Increase of wave frequency translates to increase in redshift. This is universal in all gas breakdown cases under study. A heating due to the presence of the field supplements this change, however. A very accurate temperature diagnostic (both ion and electron) would be needed to differentiate between the two effects.

It has been shown both analytically and experimentally that the mechanics of the instability depend upon the magnetic field strength. Analytically, this is due to effects both direct, and indirect through alteration of plasma parameters. A detailed analysis has not been possible of the experiment in all cases, but a plausible explanation has been offered for the very strong effects in helium and nitrogen.

II. X-Ray Diagnostics of Solid Target Plasmas

A series of experiments were performed in order to study plasmas generated by focusing the 300 Joule CO_2 laser onto solid targets of various materials[9]. Magnetic fields up to 100 kG were applied normal to the target surfaces. The geometry for these experiments is illustrated in Fig. (II-1) showing the laser focusing system, the Bitter solenoid, and several of the diagnostics used.

Three different types of X-ray diagnostics were used in these studies. A soft X-ray spectrometer was built for the study of density and temperature diagnostics based on the ratios of various lines of multiply ionized flourine atoms. Fast PIN diodes were used to measure broadband X-ray emission in the spectral range above 1 keV as a temperature diagnostic. X-ray imaging techniques including an X-ray pinhole camera were used to determine the spatial extent of the plasmas.

In this chapter the experimental results obtained with each of these techniques will be described.

II.A. Soft X-Ray Spectroscopy

1. Theory

a. Density diagnostics based on helium like atoms

The term structure of helium-like atoms is shown in Fig. (II-2). Its most notable feature is the splitting of the upper states into triplet and singlet levels according to whether the spin of the

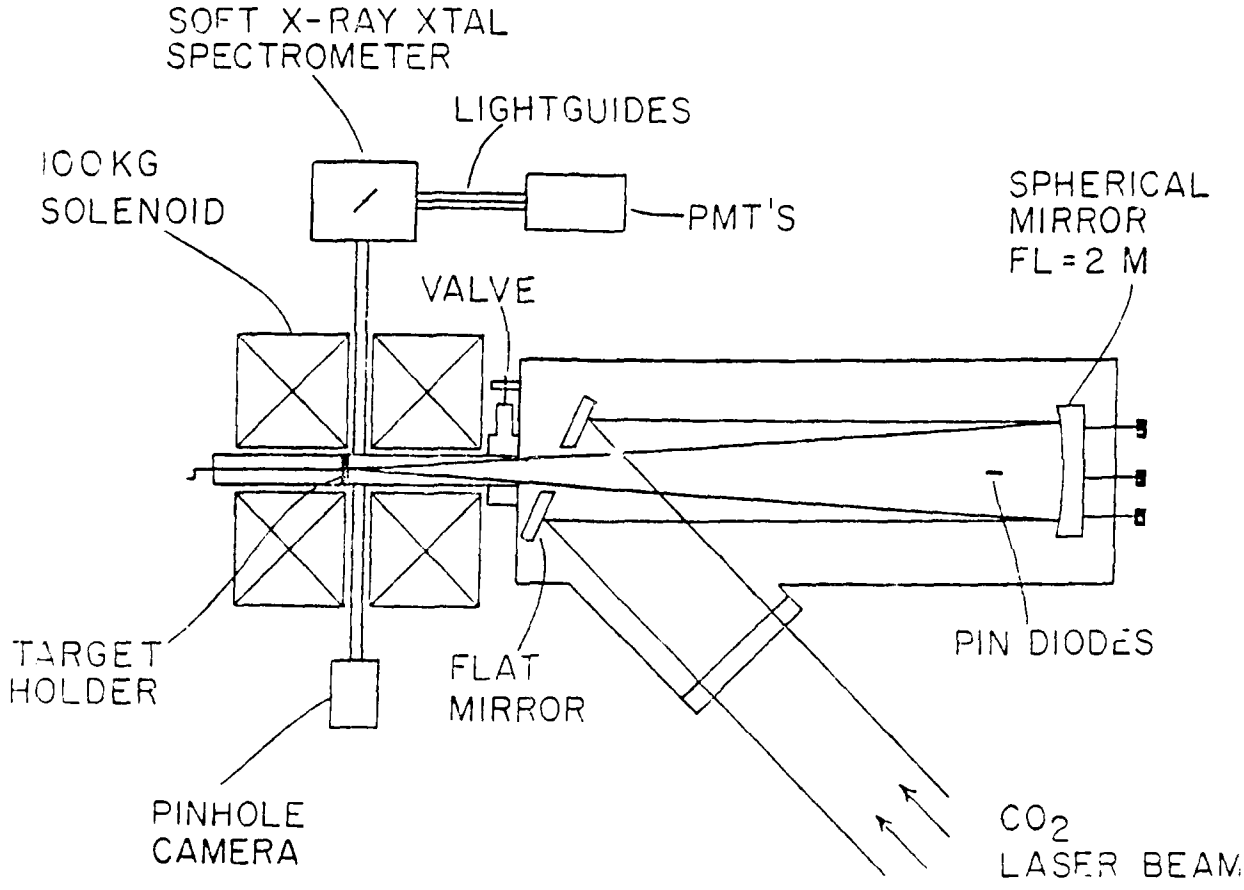

Fig. II-1 Experimental configuration for the X-ray measurements.

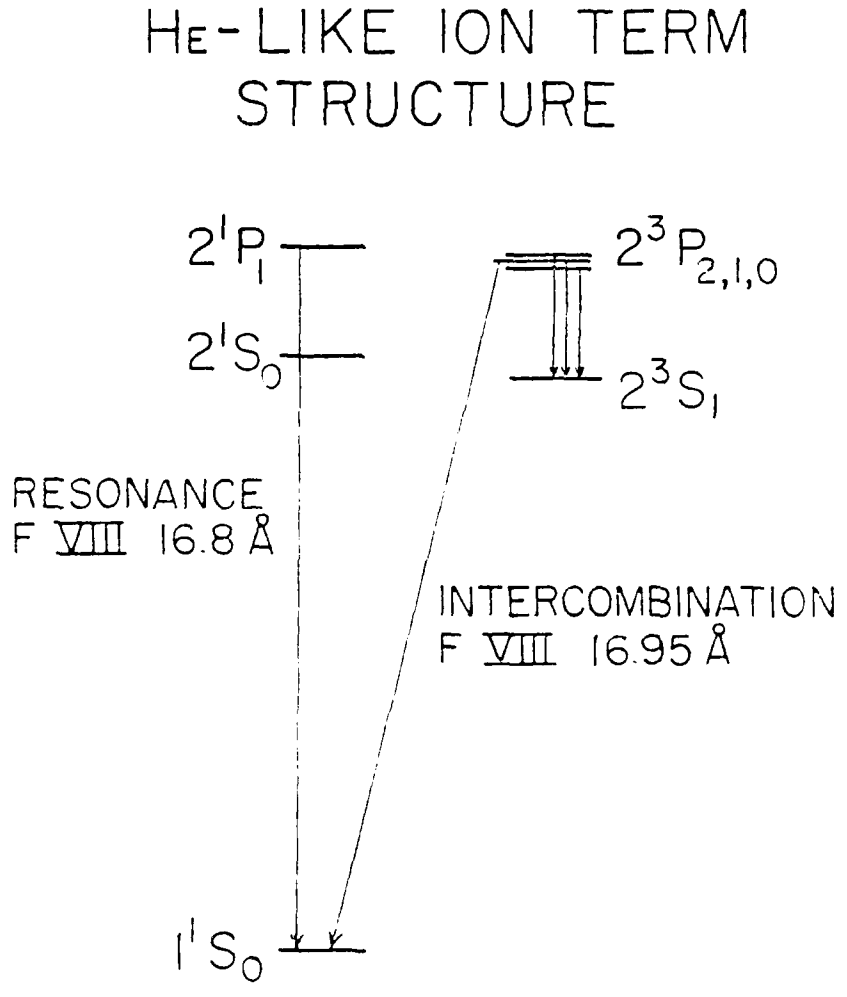

Fig. II-2 Energy levels in helium like ions.

excited electron is parallel or antiparallel to that of the ground state electron. Under strict LS coupling, transitions between triplet and singlet states are forbidden. However, this selection rule gradually breaks down as Z is increased, and the $1^1S_0 - 2^3P_1$ intercombination transition proceeds through spin-orbit interaction with a rate scaling as Z^9. In contrast, the transition rate for the $1^1S_0 - 2^1P_1$ resonance transition scales as Z^4, but its rate is 1.2×10^4 times faster than the intercombination rate for F VIII. Not shown in Fig. (II-2) are the lithium-like ion statellites of the resonance line. The upper states of these transitions are of the form 1s2px, where the 1s and 2p electrons are of opposite spin and the third electron is also excited above the ground state. Because this second excited electron partially screens the nucleus, transitions of the form $1s2px - 1s^2x$ are of slightly lower energy than the helium-like ion resonance line.

The electron density diagnostic used in these experiments is based on the collisional depopulation rate of the n = 2 triplet levels being comparable to the radiative transition rate over a certain range of electron density for each helium-like ion. The resonance-to-intercombination line intensity ratio is then a sensitive function of electron density, and can be derived from a modified corona model.

Ionization equilibrium is not assumed. The n = 2 triplet levels are statistically populated; the collisional coupling rate between the 2^3S and 2^3P levels (both direct and via triplet levels of larger n) is much faster than either the $2^3S - 2^3P$ or the $1^1S_0 - 2^3P_1$ radiative transition rates. The important collisional depopulation

mechanisms (that is, those affecting the intercombination line intensity) are ionization and spin-flip collisions (e.g., $2^3P - 2^1P$, coefficient X_{t2}, or $2^3 - (n \geq 3)^1$, with overall coefficient X_{t3}). The fraction of excitations to the n = 2 triplet levels followed by emission of an intercombination line photon is

$$F = \frac{A_{t1}}{A_{t1} + (I_t + X_{t2} + X_{t3})} \qquad \text{(II-1)}$$

where A_{t1} is the statistically averaged radiative transition rate from the n = 2 triplet levels to the ground state, i.e., one-fourth the rate for the $2^3P_1 - 1^1S_1$ transition. Collisional depopulation mechanisms are insignificant compared to the resonance transition rate, so the resonance to intercombination line intensity ratio is

$$R_{ri} = \frac{\varepsilon(2^1P - 1^1S)}{\varepsilon(2^3P - 1^1S)} = C + \frac{X_{t2}}{A_{t1}}(C + 1) + \frac{X_{t3}}{A_{t1}}(C + 2) + \frac{(I_t + X_{t1})}{A_{t1}} C \; n_e$$

$$\equiv C + \chi(z, T_e) n_e \qquad \text{(II-2)}$$

$$C = X_{12}/X_{1t}$$

where X_{12} and X_{1t} are the collisional excitation rate coefficients from the ground state to the n = 2 singlet and triplet levels.

respectively, and X_{t1} is the collisional deexcitation rate for the 2^3P levels. β is the fraction of $2^3 - n \geq 3^1$ collisions resulting in emission of a resonance photon; if the dominant contribution to X_{t3} involves the n = 3 singlet levels, $\beta = \frac{2}{3}$.

C has been experimentally determined to be 1.8 for oxygen and lighter nuclei[10]. The radiative transition rates A_{t_1} have been calculated to a high degree of accuracy; $4.62 \times 10^8 sec^{-1}$ for F VIII and $1.38 \times 10^8 sec^{-1}$ for O VII[11]. Unfortunately, the collisional rate coefficients in equation (II-2) are beset with large theoretical uncertainties; it is not even clear which term(s) dominate(s). Kunze et.al.[12], assumed X_{t2} to be the key factor, and on that basis claimed their experiments to show

$$X_{t2} = \frac{8.6 \times 10^{-8}}{Z(kT_e)^{1/2}} \text{ cm}^3/\text{sec} \qquad \text{(II-3)}$$

However, this turned out to be a factor of 20 greater than the predictions of Coulomb-Born calculations[13], and $\gamma(Z,T)$ was observed to slowly increase with T_e (Fig. (II-3)). The presently accepted theoretical values for the rate coefficients, according to Gabriel and Jordan[14], are

$$X_{t2} = \frac{3.4 \times 10^{-8}}{Z\, kT_e} \qquad \text{(II-4)}$$

$$X_{t3} = 0.61 \times 10^{-5} \frac{(kT_e)^{1/2}}{\frac{3}{2}} (2.54 + \frac{kT_e}{2})^{-1} e^{-3/kT_e} \qquad \text{(II-5)}$$

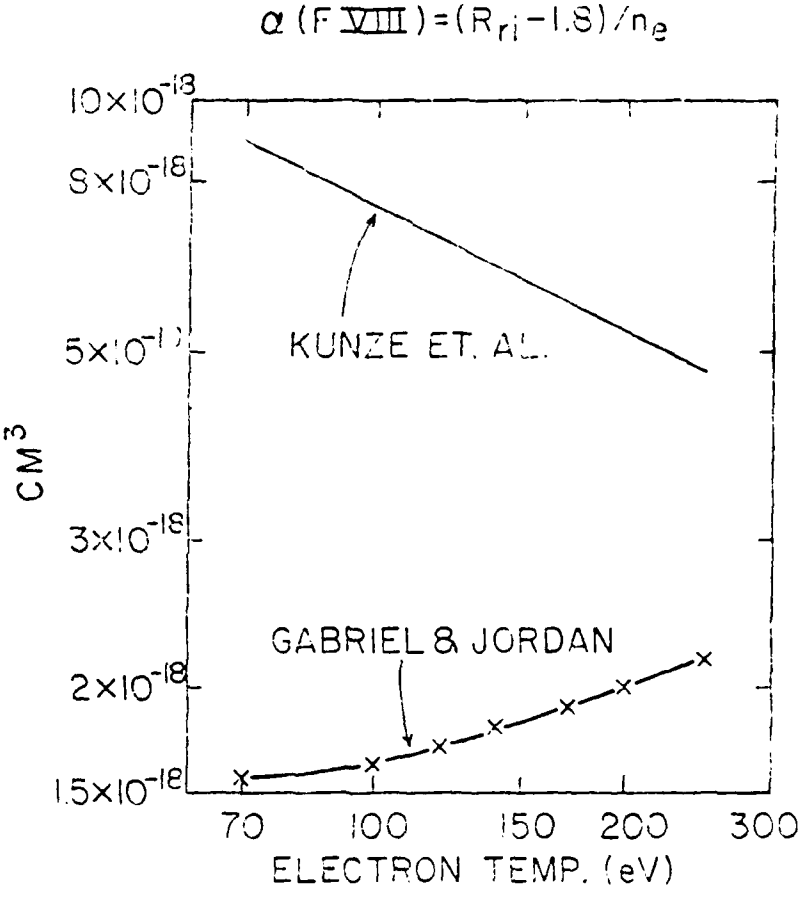

Fig. 17-3 Coefficient α(F VIII) relating F VIII resonance-to-intercombination line intensity ratio to electron density: $\alpha = (R_{ri} - 1.3)/n_e$. (O) proposed by Kunze et al.[12] (X) Currently accepted theory.[4]

$$X_{t3} \sim \frac{3.25 \times 10^{-7}}{Z^2 (kT_e)^{1/2}} \; e^{-\Delta E/kT_e} \qquad \text{(II-6)}$$

where ΔE is the energy gained by the 2^3 electron when excited to a $n \geq 3^1$ level (normally taken as n = 3). We may also add a minor adjustment for the $2^3P \rightarrow 1^1S$ collisional deexcitation rate obtained from detailed balancing of the excitation rate X_{1t}[15]:

$$X_{t1} = 3X_{1t} \; e^{E_{t1}/kT_e} \qquad \text{(II-7)}$$

where the factor of 3 accounts for the ratio of the statistical weights of the 2^3P_1 and ground states, and E_{t1} = 732 eV is the energy separation of the 2^3P_1 and ground states.

It is thus apparent that experimental measurements must be performed for each ion to determine $\phi(Z,T)$ for density estimates to be accurate. Unfortunately, only one such measurement has been done for oxygen[16] ($R_{ri} = 2.5 \pm 0.5$ at $n_e = 6.2 \pm 1.5 \times 10^{16}$ and $T_e = 250 \pm 60$ eV), and none for fluorine.

Besides the theoretical uncertainties, there are a number of other problems which must be confronted in order for measurements of the resonance-to-intercombination line intensity ratio to give worthwhile results. The density must be high enough that R is not dominated by $C_{\ }$.

The resonance and intercombination lines must be separated from nearby dielectronic recombination lines, or a correction must be applied. Unresolvable satellites might typically add ~ 10% to the apparent resonance line intensity, and a larger percentage to the intercombination

line, depending on electron density. We may thus take $3 \leq R_{ri} \leq 20$ as the range of applicability of this technique. Using equations (II-4)-(II-6) this translates to $n_e = 0.7 - 11 \times 10^{18}$ cm^{-3} for fluorine.

It is also very important that the ratio of hydrogen-like to helium-like ions not be very large if $T_e \ll E_{12}$. If the n = 2 levels are populated mainly by direct two-body recombination instead of direct excitation, the low density limit of the resonance-to-intercombination line ratio will be near one third[17]. The collisional excitation rate to the 2^1P level is[18]

$$X_{12} = 8\left(\frac{\pi}{3}\right)^{1/2} \frac{ha_o}{m_e} \frac{\chi_H^{3/2} f_{12} {}^1P}{E_{12} T_e^{1/2}} \; e^{-E_{12}/kT_e} \qquad \text{(II-8)}$$

where f_{12} is the oscillator strength (.65 for F VIII), χ_H = 13.6 eV, and P is slowly varying function of $\frac{E_{12}}{T}$, typically about 0.2. The line intensity is then

$$I_{res} = n_{He} n_e X_{12} \sim 2.06 \times 10^{-6} \frac{n_{He} n_e}{E_{21} T_e^{1/2}} \; e^{-E_{21}/T_e} \quad \frac{\text{photons}}{\text{cm}^3 \text{sec}} \qquad \text{(II-9)}$$

$$\sim 2.8 \times 10^{-9} \frac{n_{He} n_e}{T_e^{1/2}} \; e^{-738/T_e} \quad \text{for F VIII}$$

If $T_e \leq 200$ eV, the net coefficient of direct recombination into the n = 2 levels of F VIII is

$$\alpha_r^{n=2} \simeq 4.2 \times 10^{-13} \frac{X^{3/2}}{X + 0.7}, \quad X = \frac{222\text{eV}}{T_e} \geq 3 \qquad \text{(II-10)}$$

$X_{1t} = X_{12}/1.8$ and $x^{n=2}$ are plotted vs. T_e in Fig. (II-4). Of course, the actual situation is worse than indicated in Fig. (II-4), because electrons can also cascade down to the n = 2 level after recombining into a higher state. Such cascades have a greater effect on the intercombination line than the resonance, since many electrons recombining to singlet states reach the ground state without passing through the 2^1P level (especially those reaching P states of higher n). Cascades may as much as double the effect of two-body recombination on the intercombination line beyond that of direct recombination to the 2^3P levels.

Another potential problem is the optical thickness of the resonance line. At the line center this is [19]

$$\tau = 0.83 \times 10^{-12} \; f\lambda \int n_i \frac{\lambda}{\Delta\lambda_h} \, d\lambda \qquad \text{(II-11)}$$

where the integral is taken over the line of sight, and the Doppler halfwidth is

$$\Delta\lambda_h = 7.73 \times 10^{-5} \sqrt{\frac{T_i}{A}} \qquad \text{(II-12)}$$

where A is the atomic mass number, and T_i the ion temperature in eV. Thus, for the F VIII resonance line (λ = 16.8 Å, A = 19, f = 0.65),

$$\tau = 5.1 \times 10^{-15} \int \frac{n_i}{T_i} \, d\ell \qquad \text{(II-13)}$$

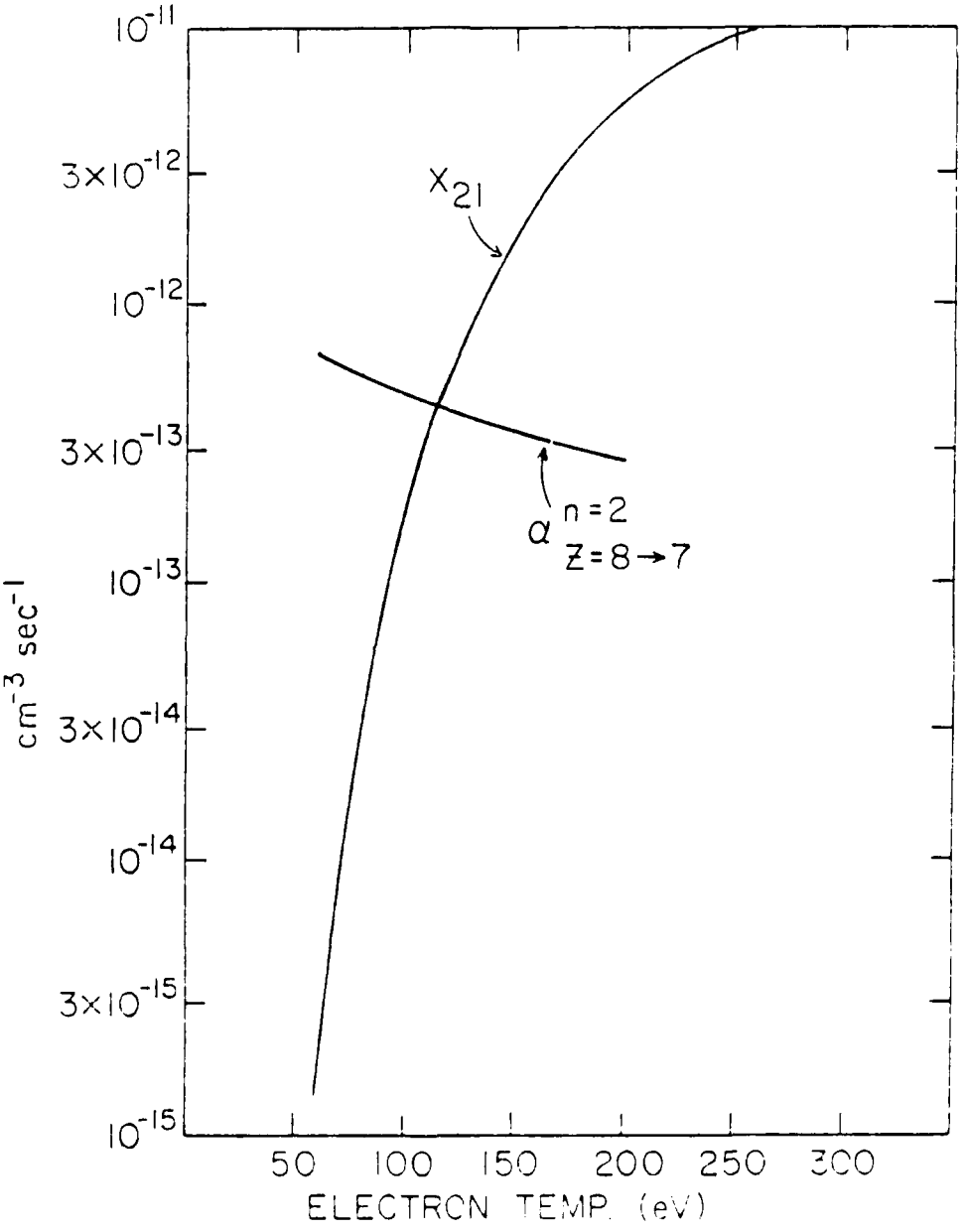

Fig. II-1. X_{21} and F VIII ionization rate coefficients for $2^2S_{1/2}$ state of F^{+7} ion. n = 2 coefficient is for recombination of electron and F VIII ion into n = 2 level of F VIII.

If τ is non-negligible, one should in principle solve the equation of radiative transfer,

$$\frac{dI_\nu}{dx} = \varepsilon_\nu - K_\nu I_\nu \qquad \text{(II-14)}$$

where I_ν is the intensity of radiation of frequency ν, ε_ν the emissivity and K_ν the absorption coefficient. For a uniform plasma of thickness d, the solution of (II-14) is

$$I_\nu = \left(\frac{\varepsilon_\nu}{K_\nu}\right)(1 - e^{-\tau}) \quad , \quad \tau = K_\nu d \qquad \text{(II-15)}$$

In LTE, ε_ν/K_ν is the Planck blackbody function and is independent of I; that is, the source term is essentially unaffected by collisions. In that case, a correction must be applied for $\tau > 0.1$. However, in coronal equilibrium, if a resonance photon is absorbed by an atom, it is highly probable that the photo-excited atom will re-radiate another resonance photon. Using equation (II-2), it can be seen that upwards of 99.9% of absorbed FVIII resonance photons will be re-radiated if $R_{ri} < 20$. The end result is that ε_ν is a function of I_ν, and unless the optical depth of the resonance line is very large in all directions, the total resonance line emission of the plasma will essentially be unaffected. For example, suppose the average F VIII resonance photon has only a 2% chance of escape (average optical depth of 4); the total F VIII resonance line emission is then reduced by less than 5% even for $R_{ri} = 20$. Thus, the primary effect of non-negligible optical depth will be on the angular

distribution of the radiation. In particular, for a long, axially symmetric cylindrical plasma, a detector looking at the plasma end-on may see a great reduction in intensity due to optical depth, while one viewing the plasma side-on simultaneously detects the intensity predicted assuming $\tau = 0$. Such an effect has been observed in a theta pinch . However, when viewing the surface region of the plasma side-on there may be problems. Consider, for example, conditions one may expect near the critical surface ($n_e = 10^{19}$ cm^{-3}) of a CF_2 plasma early in the pulse. If 50% of the fluorine ions still have two electrons, $n_{F\ VIII} \sim 5 \times 10^{17}$. If $T_i \sim 100$ eV (ions not well-thermalized) and the plasma diameter is $\sim$ 0.4 mm, the optical depth of the F VIII resonance line is about 20 across the plasma column. However, with a strong density gradient in the axial direction, photons are more likely to escape the plasma by first travelling away from the surface. Hence the amount of line radiation detected under these conditions may be less than expected.

The resonance and intercombination lines must be separated from nearby dielectronic recombination lines or a correction must be applied. Unresolvable satellites might typically add $\sim$ 10% to the apparent resonance line intensity, and a larger percentage to the intercombination line , depending on electron density[14]

b. Temperature diagnostics based on satellite to line ratios

Many satellite lines appear to the low energy side of the helium-like resonance line which arise from lithium-like ions with two excited electrons. These lines can arise from direct excitation of lithium-like ions; however, a high temperature plasma whose lifetime greatly exceeds τ_{He} produces them primarily by dielectronic recombination. A free electron is captured into an $n \geq 2$ level, and gives up its energy to an inner shell electron so that it too winds up in a state with $n \geq 2$. Each satellite line can thus be excited only by electrons of energy $E_s = E_{12} - \chi_s$ where E_{12} is the photon energy and χ_s is the ionization potential of the second excited electron. Because this process is the inverse of autoionization, its rate coefficient can be calculated using the principle of detailed balance[20],

$$\alpha_D = \frac{h^3 A_a}{2(2\pi m_e kT_e)^{3/2}} \frac{g_s}{g_1} e^{-E_s/kT_e} \qquad \text{(II-16)}$$

where A_a is the autoionization rate and g_s and g_1 are the statistical weights of the satellite level and helium-like ion ground state, respectively. The fraction of such excited ions decaying by radiative means instead of autoionizing is $\beta = A_r/(A_r + A_a)$, where A_r is the radiative transition rate. Since $A_a >> A_r$ for all satellite lines being considered here,

$$I_s = n_e n_{He} \beta \alpha_D = 4 n_e n_{He} \left(\frac{\pi a_0^2 \chi_H}{kT_e}\right)^{3/2} \frac{g_s}{g_1} A_r e^{-E_s/kT_e} \qquad \text{(II-17)}$$

Comparing this to the resonance line intensity (equation (II-9)), we have the density-independent line intensity ratio

$$R_{rs} = \frac{I_{res}}{I_s} = \frac{3.78 \times 10^4}{E_{21}^3} \frac{g_1}{g_s} \frac{A_{21}}{A_r} T_e \; e^{-(E_{21}-E_s)kT_e} \qquad \text{(II-18)}$$

The exponential dependence suggests that measurements of dielectronic recombination satellite emission can give an estimate of electron temperature. Furthermore, measurements of $R_{rs}(T)$ have been performed in a theta pinch for several prominent satellites of the O VII and F VIII resonance lines by Pospieszczyzyk[21]. $R_{rs}(T)$ is plotted in Fig. (II-5) for the F VIII $1s^2\ 2p\ ^2P$-$1s2p\ ^2D$ transition (17.17 Å). The principal difficulty associated with this diagnostic method is the low intensity of the satellite lines (typically two orders of magnitude less than that of the resonance line). One must also be wary of recombination-induced resonance line emission as described previously, and the satellite lines can be difficult to separate from each other.

Bhulla et al., have calculated I_s/I_r for twenty-four different configurations having both excited electrons in n = 2 states[22]. For oxygen at 161 eV, nine have $I_s/I_r > 5 \times 10^{-4}$, with the maximum value 6.9×10^{-3}. The two satellite lines most suitable for measurements are both actually blends of two very closely spaced transitions. Pospieszczyk resolved seventeen separate satellite lines apiece for oxygen and fluorine. Unfortunately, in the case of fluorine two of the brighter lines are very difficult to separate from the intercombination line, so a correction must be applied as discussed previously.

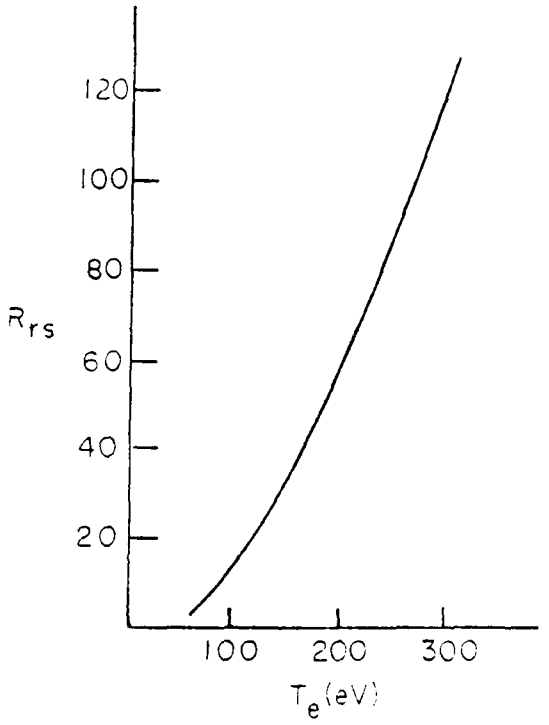

Fig. II-3 Intensity ratio R_{rs} for F VIII resonance and F VII [illegible] satellite lines.

2. The Soft X-Ray Spectrometer

The soft X-ray spectrometer consists of an evacuated pipe leading from the experimental cell to an evacuated box, a flat crystal mounted within the box, and a detection system. A vertical slit ($\perp$B) is normally inserted in the front end of the pipe. A schematic of the basic configuration is shown in Fig. (II-6). All sides of the spectrometer box have 6" or 8" openings for windows, detectors mountings, vacuum feed-throughs, vacuum couplings, etc.

The dispersive element of the spectrometer is a flat, 2.1 x 6.3 mm thallium acid phthalate (TAP) crystal. The wavelength dispersion is given by the Bragg law,

$$\lambda = 2d \sin \theta \qquad \text{(II-19)}$$

where d is the lattice spacing and θ the angle of incidence. With double atomic spacings 2d of order 26 Å, the acid phthalate crystals are well suited for spectroscopy of highly-ionized oxygen and fluorine ions. TAP has a resolving power $\lambda / \Delta\lambda \sim 700$ over the range of interest, where $\Delta\lambda$ is the FWHM of the Lorentzian rocking curve. While this is only half the resolving power of potassium acid phthalate (KAP, 2d = 26.6 Å), it is sufficient to separate the resonance and intercombination lines of F VIII ($\lambda/\Delta\lambda \sim 120$). TAP was chosen for its high reflectivity, five times that of KAP, of about 12.5% for the F VIII resonance line (16.81 Å) and about 17% for the F VIII $1s3p\text{-}1s^2$.

SOFT X-RAY CRYSTAL SPECTROMETER

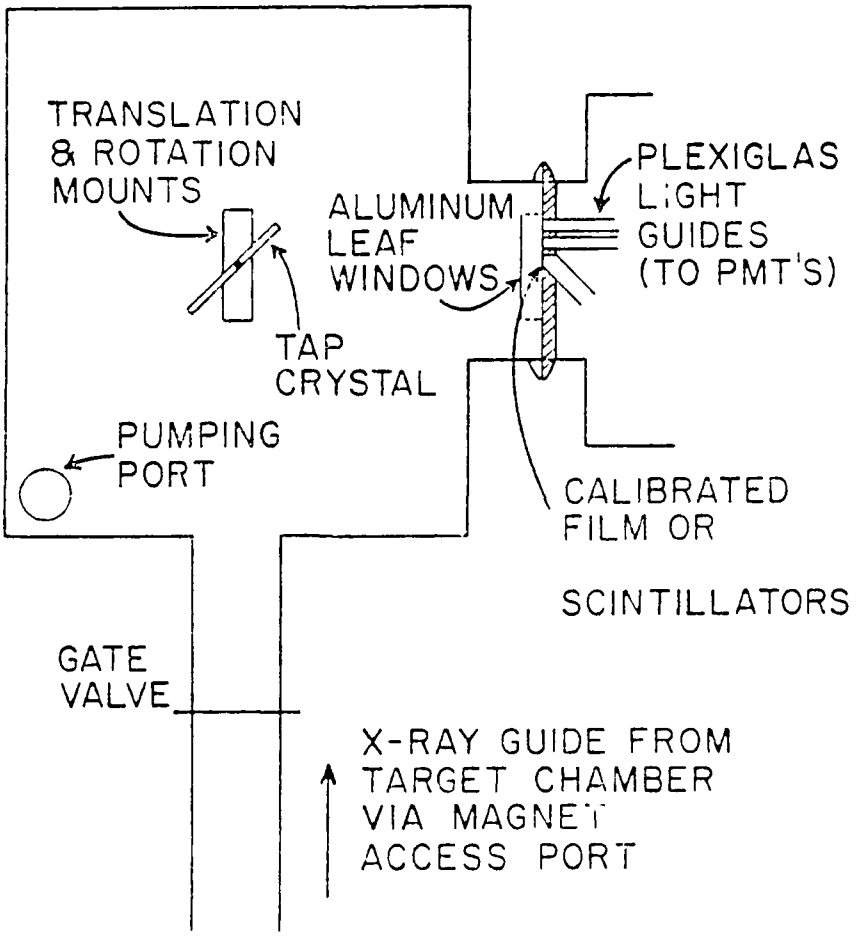

Fig. II-9. Schematic of the soft x-ray spectrometer.

With the configuration of Fig. (II-6), one limitation on the range of wavelenghts that can be scanned in a single spectrum arises from the width of the magnet's access port. With the inside width of the pipe 7/16" at a distance of $6\frac{1}{2}$" from the plasma, the range of Bragg angles is $\Delta\theta \approx .67$ radian = 3.8°. The length of the crystal itself is the other limit; for central Bragg angle θ_o the range is given by

$$\Delta\theta = \frac{6.3\sin\theta_o}{R} \qquad \text{(II-20)}$$

where R is the separation of the crystal and plasma. Thus, for $\theta_o = 40.74^{\circ}$ ($\lambda = 16.807$ Å, the resonance line) and R = 100 cm, $\Delta\theta = .041$ radian, which is more stringent than the limitation imposed by the channel width but it is still enough to get the resonance line and all its satellites. However, for $\theta_o = 17.5^{\circ}$ ($\lambda = 7.757$ Å, the Al XII resonance line), if R = 100 cm, $\Delta\theta = .019$ radian $\approx 1.1^{\circ}$. Hence the crystal was moved as close to the plasma as possible when aluminum spectra were taken.

The crystal was mounted on a shaft whose angle was set by a worm-and-wheel assembly Fig. (II-7). For time-resolved spectra, the exact location of the lines at the detector is critical, so the worm-and-wheel assembly was mounted atop a translation stage. Unlike the worm, the translation stage could be controlled from outside the spectrometer box without breaking vacuum.

The axial spatial resolution attainable in the configuration of Fig. II-6 is of course equal to the entrance slit width. This was set at 1.0, 1.5 or 2.5 mm. No spatial resolution could be obtained in the radial direction of this configuration.

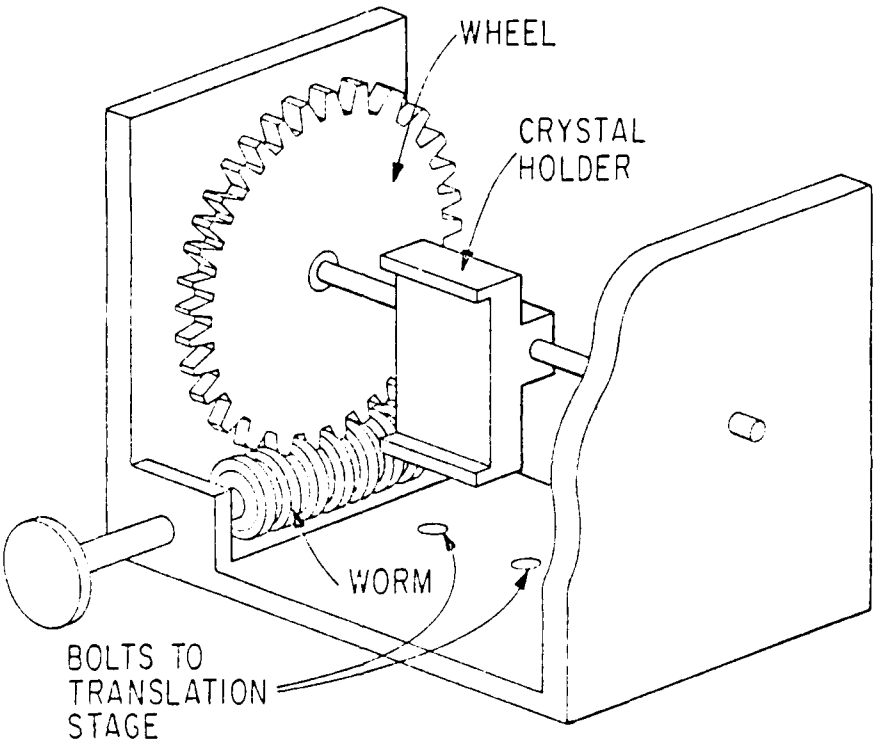

Fig. II-7 TAP crystal mount. Crystal angle set by worm and wheel. One turn of worm rotates the wheel by 1°.

For time-integrated spectra with radial "imaging" of the line-emitting region, the crystal was mounted with its rotation axis parallel to the magnetic axis fig. (II-8). In this configuration the lines are brodened by the diameter of the plasma column plus the width of the crystal rocking curve. The latter contribution, expressed in terms of Bragg angle ($\Delta\theta$), is independent of R, whereas that from the plasma size decreases linearly with distance. Thus, to minimize the effect of the crystal rocking curve on the line profile, the crystal was positioned as close as possible to the plasma (~ 50 cm). This also maximized the range of X-ray wavelengths covered in a single spectrum, which was no longer limited by the size of the magnet access port. The resolution (rocking curve width) was then ~ .45 mm for $\theta_o = 33^o$. The size of the "image" is magnified from the plasma diameter by sec $(90^o - 2\theta_o)$.

a. Time-integrated detection

Several film holders were made up for studies of time-integrated spectra (Fig. (II-9)). These are simply two metal plates which sandwich the film. One has an X-ray window; the other has felt or O-ring baffling surrounding the film to keep visible light out and to allow the filmholder to be pumped out and re-exposed to atmosphere without rupturing the windows. The windows consist of two layers of not-quite-pinhole free aluminum leaf, each of thickness of 0.8 μm or 1.05 μm.

The windows are longer than the crystal; thus the film records all lines reflected by the crystal.

The filmholders were normally mounted from a flange on the side of the box. Between the crystal and the film was a plate with a

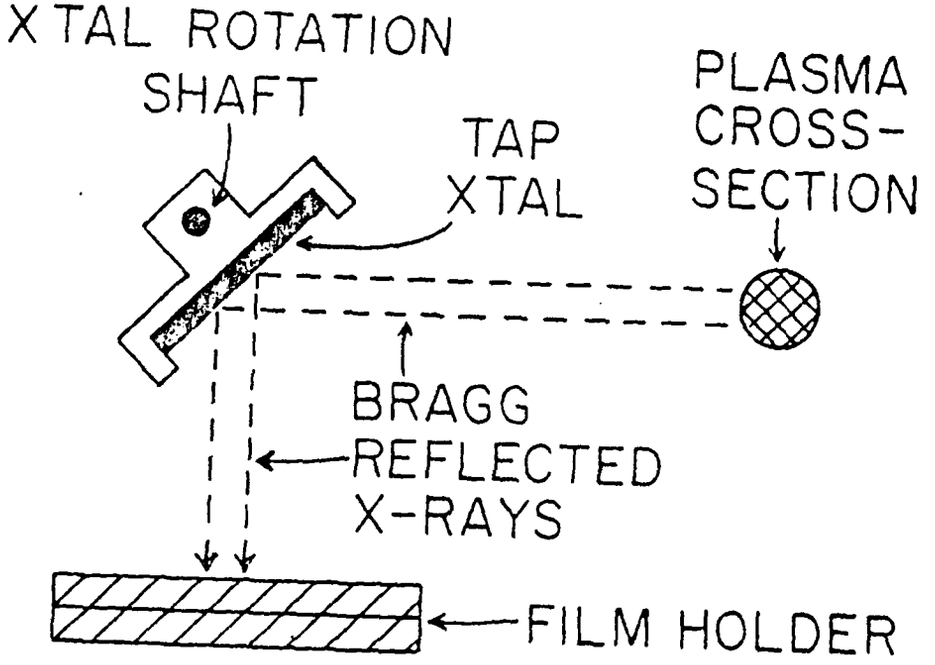

Fig. II-8 Configuration of spectrometer used for obtaining profile of line-integrated line emission vs. plasma radius.

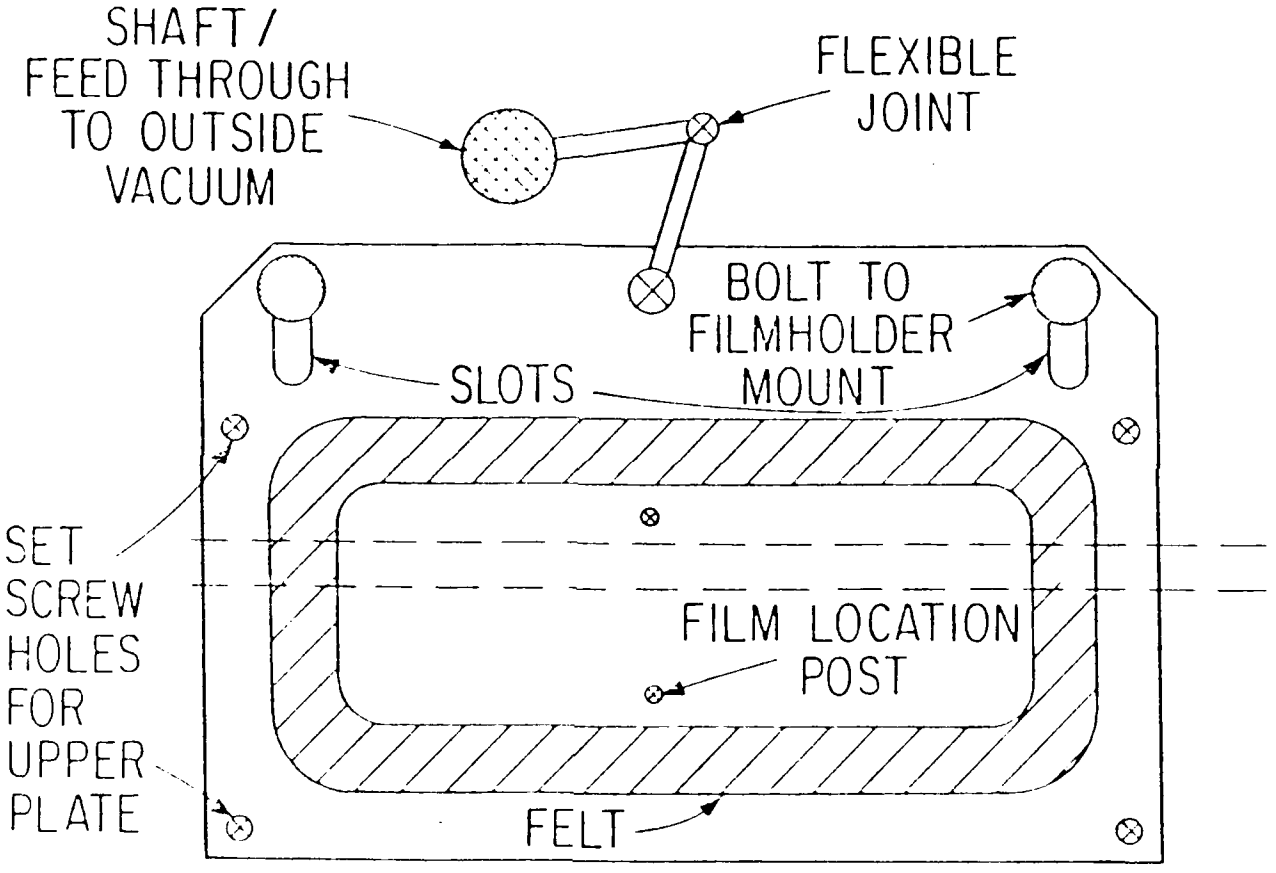

Fig. II-9 Lower plate of typical filmholder. Dashed lines indicate position of slit in fixed plate located between filmholder and crystal. Rotation of shaft raises or lowers filmholder, thus exposing a different part of the film.

horizontal slit; the filmholder could be moved up or down from outside the box without breaking vacuum. In this manner two spectra could be taken on the same piece of film.

A different mount had to be used for taking aluminum spectra. When the filmholder is mounted perpendicular to the magnetic axis line intensities are attenuated by exp $(-\mu\rho d/\sin 2\theta)$, where d is the window thickness, ρ the mass density, μ the mass attenuation coefficient, and θ the Bragg angle. For the Al XII resonance line, $\sin 2\theta = \sin 35^\circ$ .574, thus increasing the attenuation by 2.1 μm of Al from 2.4 to 4.2 e-foldings. Hence the filmholder is mounted at 45° with respect to the magnetic axis (incidentally restricting us to one spectrum per piece of film).

Kodak 2490 film was used in these experiments, for both imaging and spectroscopy. The response of this film to soft X-rays has been calibrated. If exposure is not high enough to cause saturation it is of the form[23]

$$\log_{10} (10^D - 1) = A(\varepsilon) \log_{10} H + B(\varepsilon) \qquad \text{(II-21)}$$

where D is the diffuse film density, H is the exposure in photons/$(\mu m)^2$, ε the photon energy, and $A(\varepsilon)$ and $B(\varepsilon)$ were interpolated from experimental values reported in ref. 23 : A(16.3 Å) = .889, B(16.8 Å) = -.33; A(7.76 Å) = 1.25, and B(7.76 Å) = .03. The response curves are not truly linear at low density; $D \to H^A$ as $D \to 0$. Film density is determined with a Jarrell-Ash specular microphotometer. As a rough check on the film calibration, one-and-five shot exposure spectra were taken of teflon

targets on the same piece of film under identical conditions of laser focus, target position, magnetic field and crystal angle.

b. Time-resolved detection

The time-resolved detection system (Fig.(II-10)) has two closely-spaced channels for simultaneous measurements of two X-ray lines. Each channel consists of a scintillator, plastic lightguide, and a photomultiplier tube. The scintillators are covered by masks which define the spectral bandpass, and two layers of 0.6 μm thick Al leaf to keep out visible light.

The two-channel capability is useful beyond the resonance-to-intercombination and resonance-to-satellite ratios described above. For example, simultaneous measurement to the F VIII $1s3p-1s^2$ and F IX Lyman α lines (14.458 and 14.984 Å, respectively) can provide an estimate of the relative populations of helium-like and hydrogen-like ions. The F VIII $1s4p-1s^2$ and $1s5p-1s^2$ lines (13.78 and 13.32 Å) could be monitored to determine if three-body recombination ever becomes an important process for populating the upper states. However, the only results of simultaneous measurements of two lines reported here involve the resonance and intercombination lines.

The NE-102 plastic scintillators are 0.25 mm thick, 1.3 cm wide and 2.3 cm high (which exceeds the height of the X-ray beam reflected off the 2.1 cm wide crystal). The thickness is sufficient to stop all X-rays of these energies incident upon the scintillator.

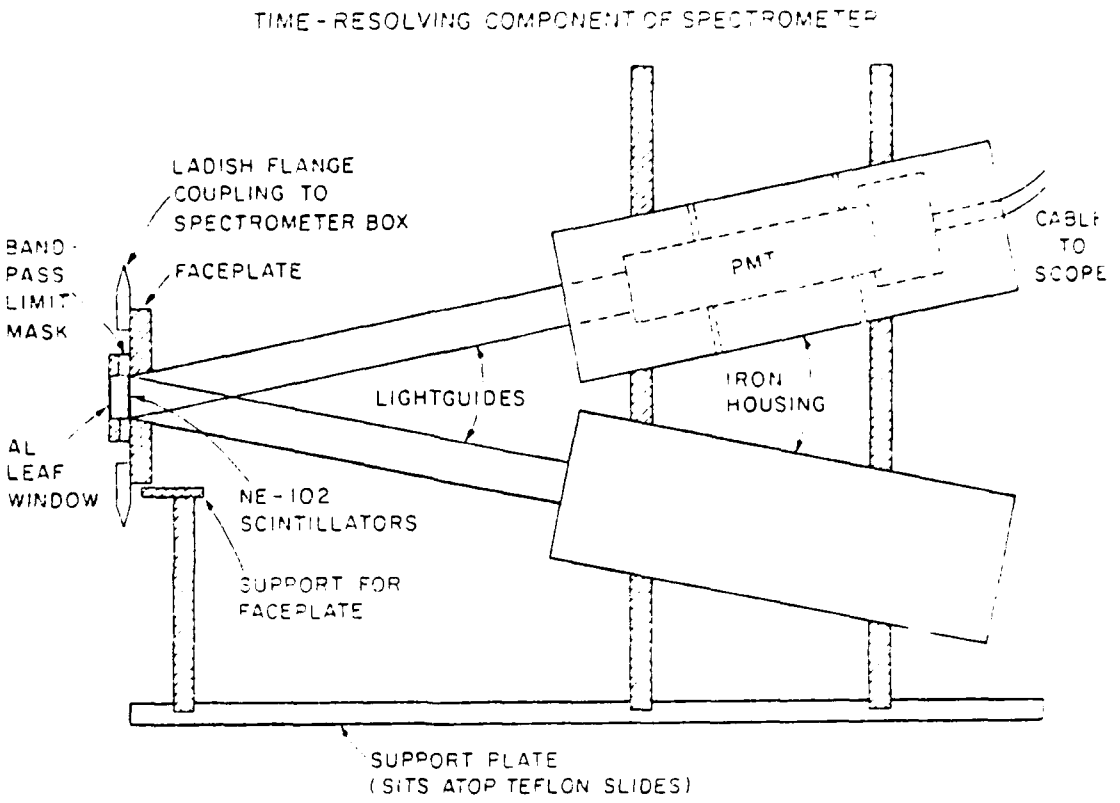

Fig. II-10 Photomultiplier tube assembly as part of the time-of-flight spectrometer for making time resolved measurements.

The lightguides are glued into a faceplate which attaches onto the spectrometer by means of a 4" ladish fitting. The two channels are 0.25 cm apart. The lightguides are mounted at $\pm$ 11^{o} from horizontal. However, the ends have been angle-cut; the scintillators are thus parallel to the inner surface of the faceplate, though slightly recessed from it. A hole for a third channel has also been cut in the faceplate, the third lightguide would be mounted in the horizontal plane 45^{o} from the other lightguides. For the experiments described here, this hole was covered over.

The cross-sectional dimensions of the lightguides were 1.3 x 2.4 cm; the length, 28 cm. The lightguides were wrapped in aluminum foil to keep scintillator light in and room light out. The entire lightguide assembly was also wrapped in felt.

Each lightguide couples to an Amperex XP2010 photomultiplier tube. Each phototube is shielded from stray magnetic fields by an iron housing. The diameter of the phototubes is about 3.0 cm, just slightly larger than the diagonal of the lightguides.

Masks were prepared for each line pair based on line separations observed in time-integrated spectra. The mask used for observations of F VIII resonance and intercombination radiation had two slits with a center-to-center separation of 3.3 mm. For these lines, the nearby satellites make it impossible to integrate over the entire linewidths; hence the slits were 2.0 mm wide, not much larger than the spectrometer entrance slit. In contrast, the mask prepared for the better separated F VIII $1s^2$-1s4p and $1s^2$-1s5p lines had 4.8 mm wide slits. (Channel separation was 16.5 mm). Portions of the masks in contact with the

faceplate were lined with felt to keep out stray light and to prevent crosstalk between the two channels (i.e., visible photons from one scintillator reflecting off the window into the other channel). Also for the prevention of crosstalk, the mask thickness was reduced from .125" to .040" in the vicinity of the slits, and the front surface was painted black.

Wavelength calibration was accomplished with the aid of a third filmholder. Small posts were screwed into its bottom plate to allow precision placement of the film. However, final wavelength alignment was performed by translating the crystal and seeking the position of maximum signal.

The response time of the scintillators is ~ 2 ns. The transit time for electrons across the photomultiplier tubes is ~ 40 nsec, but the spread in arrival times is only 2 nsecs. Thus, the net time resolution attainable using a Tektronix 7844 oscilloscope with 7A16A plug-ins is 5 nsec.

The relative response of the two channels was determined by translating the crystal from its normal position so that the F VIII resonance line was recorded on the long wavelength channel (normally used for the intercombination line). Comparison of signals for identical conditions of magnetic field and target position showed the short wavelength channel to be 2.4 times as sensitive as the long wavelength channel. By rotating the crystal and then translating it to get the same line back on the short wavelength channel, it was also verified that there is no substantial variation in crystal reflectivity along its surface.

3. Experimental Measurements

a. Time-integrated spectra with crystal rotation axis perpendicular to $\vec{B}$

The bulk of the time-integrated spectra taken with the crystal rotation axis perpendicular to $\vec{B}$ involved the F VIII resonance and intercombination lines and associated F VIII satellites. In spectra obtained with the target surface lining up with one edge of the 2.5 mm wide slit the lines are wider with B = 100 kG than with B = 0 because of source broadening, since as with the continuum emission recorded with X-ray pinhole photography, most of the line radiation comes from near the surface at B = 0, but not when strong magnetic fields are present. Peak line intensity near the surface is maximized at 70-80 kG, although quantitative analysis is difficult because of the large density gradients and the optical thickness of the resonance line.

Figures (II-11) and (II-12) are plots of time-integrated intensity vs. B for the resonance and intercombination lines at 0.6 and 1.05 cm from the surface. Intensities displayed are for the points of maximum film density, with no attempt made to correct for optical depth of underlying satellites. Line emission is maximized 30 kG. These values are listed in Table II-1. Also listed are intensity ratios for F VIII resonance to F VIII satellite and the values of T_e, n_e and z they imply at z = 0.6 cm. The high values of z (particularly z = 5.3 at B = 30 kG) imply that the estimates of n_e and T_e are of dubious value. (Note that applying corrections for underlying satellites to the resonance and intercombination lines would increase the ratio, and thus the estimated density.

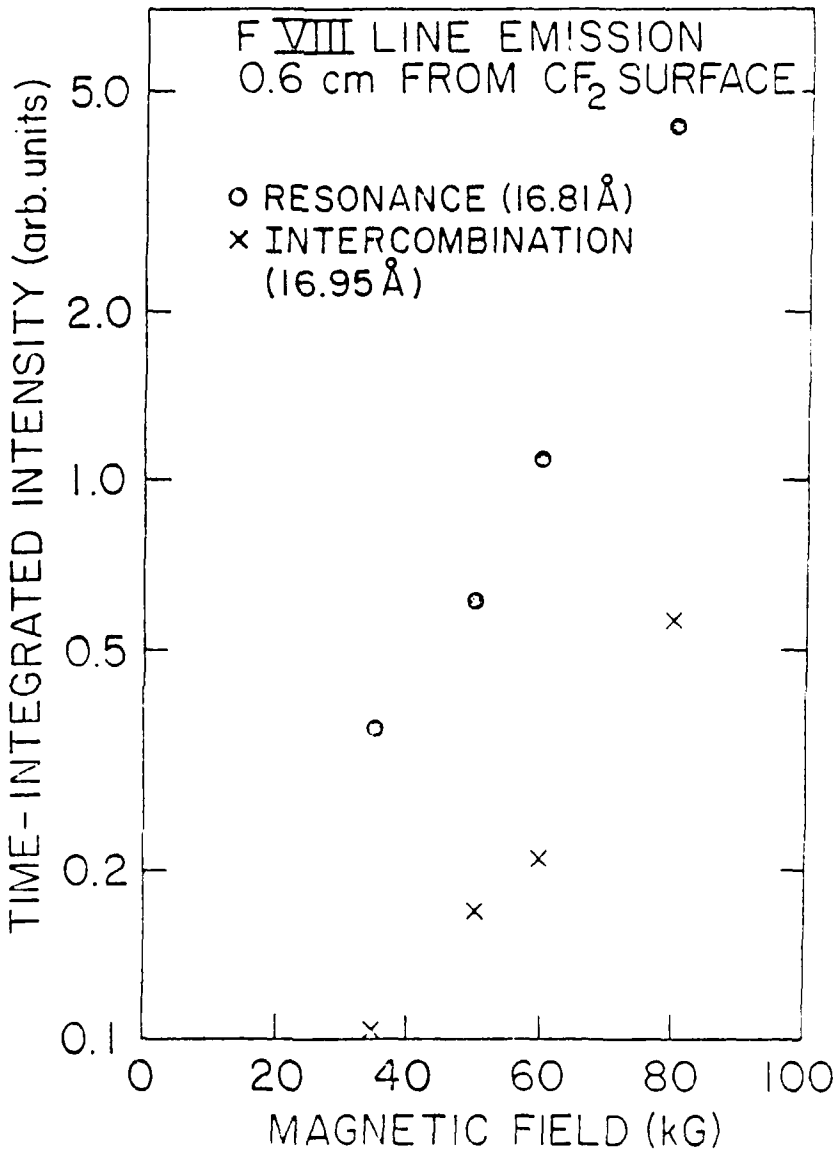

Fig. II-11. Time-integrated intensities of resonance and intercombination lines from plasma 0.6 cm from the [illegible]

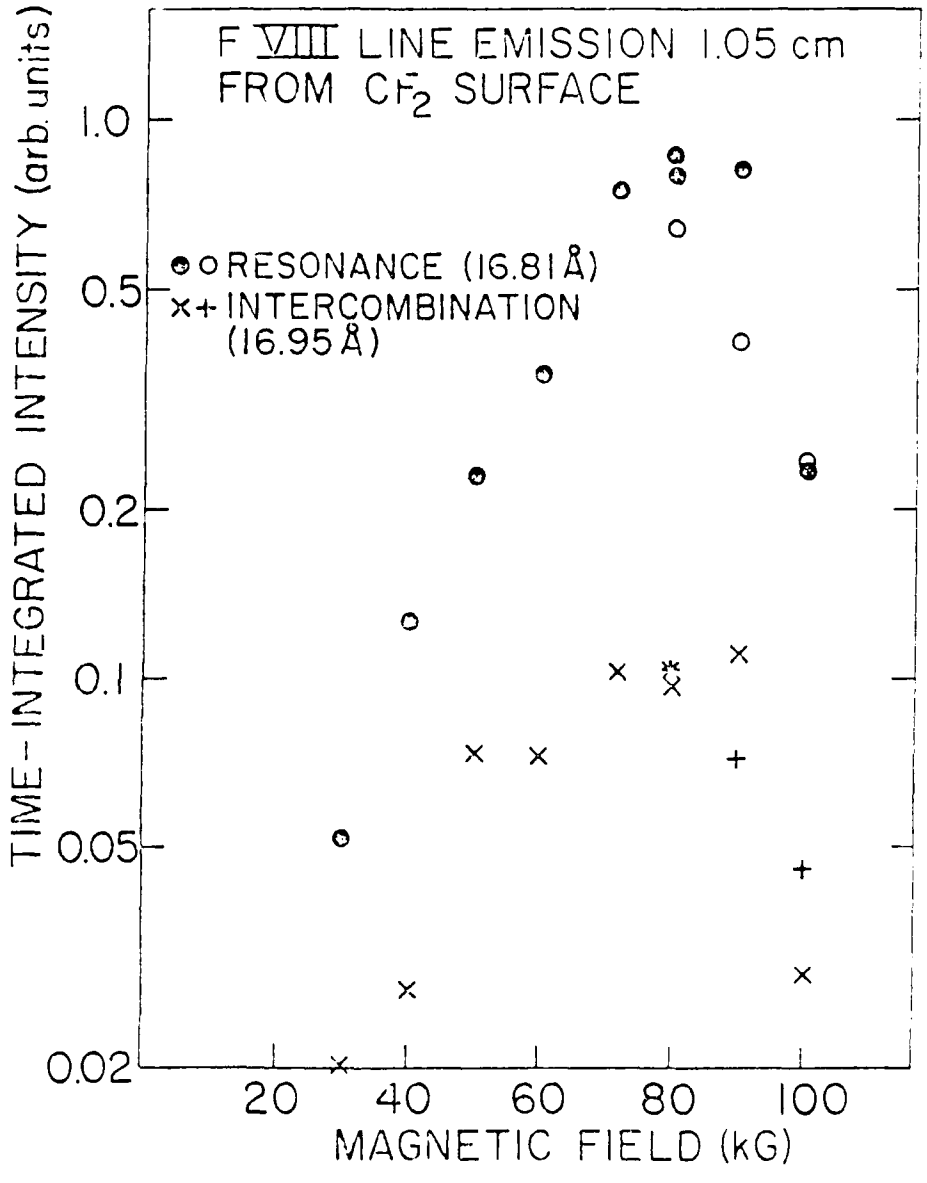

Fig. II-12. Time-integrated intensity of the resonance line (1s^2 ^{1}S$_0$ - 1s2p ^{1}P$_1$) and intercombination line (1s^2 ^{1}S$_0$ - 1s2p ^{3}P$_1$) of F VIII as a function of magnetic field strength. The data points were obtained from three different discharges.

TABLE II-1 TIME-INTEGRATED FLUORINE SPECTRA SLIT

CENTERED 0.6 cm FROM CF_2 TARGET SURFACE

B(kG)	-Peak exposure, photons/μm^2, 12 shots*- H_r(16.81 Å)	H_i(16.95 Å)	H_s(17.17 Å)	R_{ri}	$n_e(10^{18}$ $cm^{-3})$	R_{rs}	T_e(eV)	β
35	.32	.09	.013	3.5	1.00	25	125	5.0
50	.42	.12	.017	3.5	1.00	25	125	2.5
60	.87	.16	.013	5.4	1.80	75	220	5.5
80	3.20	.40	.032	8.0	2.85	100	260	5.3

* Normalized to slit width of 1.5 mm (See Appendix B).

† Data obtained using 1.6 μm Al window; exposure normalized to 2.1 μm.

Spectra were also obtained from aluminum using no slit. In these spectra, the resonance line was actually weaker than the intercombination line, probably because of optical thickness. The resonance line intensity monotonically decreased with magnetic field. The lack of source broadening of the lines regardless of magnetic field is consistent with pinhole pictures of Al plasmas showing intense X-ray emission only from the region very close to the target surface.

b. Crystal rotation axis parallel to $\overline{B}$

Time-integrated intensities of F VIII and F IX lines, other than the F VIII resonance and intercombination lines (which are too closely spaced), were obtained using the "radial imaging" configuration. With B = 0 the width of the F VIII $1s3p-1s^2$ 14.458 Å line is 1.2 mm (FWHM) after correcting for the film non-linearity and the magnification arising from the crystal geometry (sec $(90^\circ - 2\theta_o)$ = 1.1). Since the width that would be observed if the plasma were infinitely narrow would be .43 mm (from the crystal rocking curve), this is roughly consistent with the 0.6 mm (FWHM) diameter observed with B = 0 using pinhole photography. With B = 40 kG, the FWHM of the 14.458 Å line only increases to 1.5 mm; but there is nonetheless a substantial increase in line emission further away from the focal point, well above what is observed in pinhole photographs. Finally, with B = 100 kG the line emission profile expands to a diameter of 2.8 mm (FWHM). Even after subtracting the crystal rocking curve component, this is significantly above the 1.7 mm plasma diameter observed in pinhole pictures. No significant difference in the widths of the line emission

profiles of the F VIII $1s3p\text{-}1s^2$ (14.458 Å) and F IX Lyman α (14.984 Å) lines is observed between B = 0 and B = 100 kG, although the peak of the F IX line profile is flatter. Continuum emission just beyond the He-like series limit increases with B up to 80 kG. The range of photon energies covered on these spectra was insufficient to give a good estimate of T_e based on the slope of the continuum.

c. Time resolved spectra

F VIII resonance and intercombination line intensity was recorded as a function of time for a variety of magnetic fields and axial positions through a 1.5 mm wide slit. From the time of first deflection from zero intensity vs. position, front velocities can be inferred. The front velocity is 2-2.5 x 10^7 cm/sec regardless of magnetic field, which corresponds to fluorine ion energies of 4-6 kev. Application of magnetic fields of less than 50 kG actually decreases line emission from the surface, with peak intensity minimized with B = 30 kG (down ~ 30% from B = 0). Resonance line emission is maximized at about 70 kG at the surface, and 80 kG away from it.

Peak resonance line intensity is plotted as a function of magnetic field at the surface and at z = 5 and z = 10 mm in Fig. (II-13). Direct comparison of intensity measurements made at the surface with those at other positions would not be meaningful, since the effective slit width in the former case was very small. Moving the target back ~ 1 mm from the z = 0mm position at B = 80 kG caused the resonance line intensity to increase by more than a factor of five.

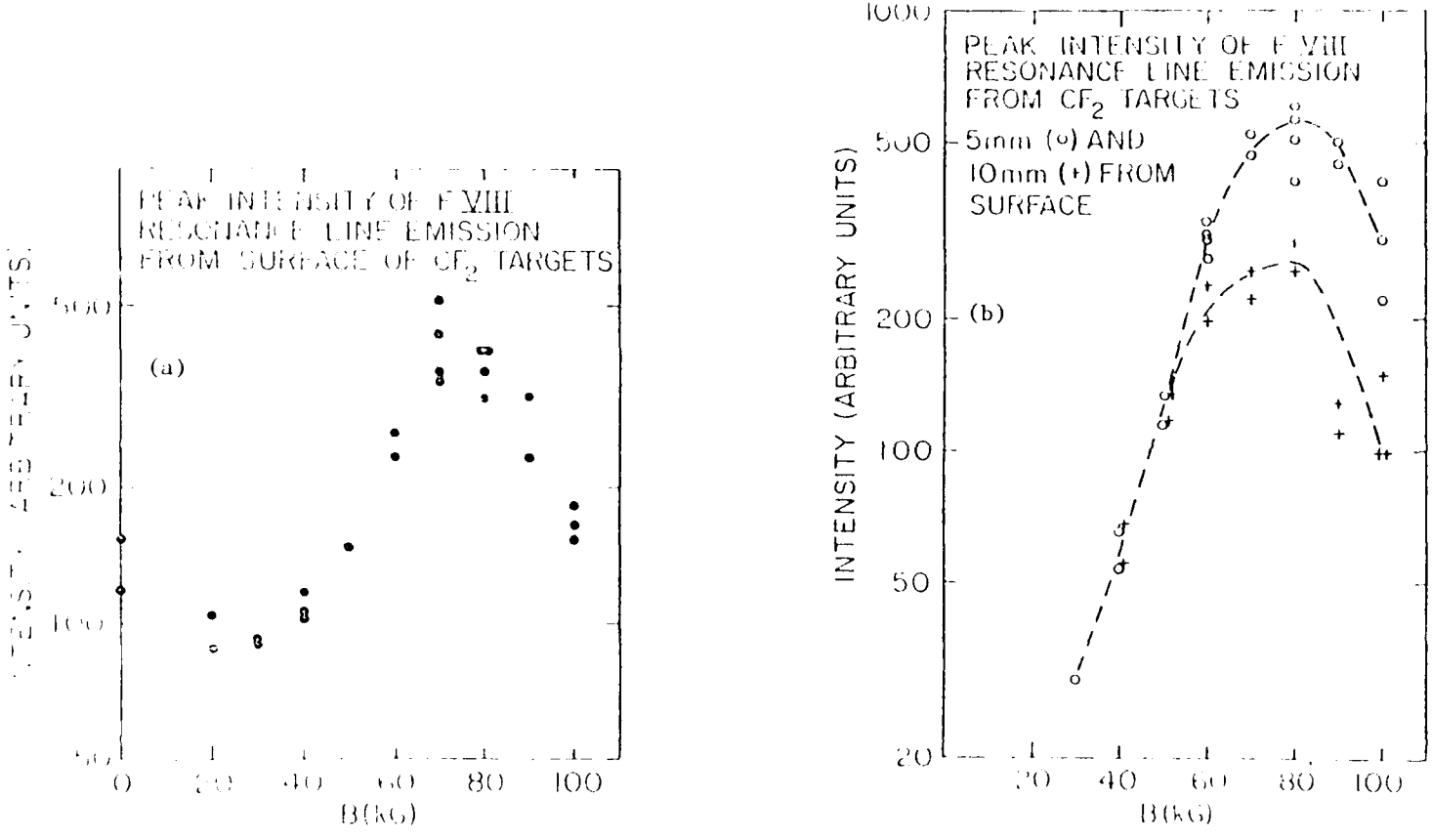

Fig. II-13 Peak intensity of resonance line emission vers. magnetic field (a) from the surface and (b) 0.5 and 1.0 cm from the surface.

At z = 5 mm, a second feature is evident in the resonance emission after the main peak. Its separation in time from the first peak decreases with increasing magnetic field; it appears as a plateau for B $\leq$ 70 kG, a second peak at higher magnetic fields, and merges with the first peak when B = 100 kG. The time of this second feature is plotted in Fig. (II-14) relative to (a) time of breakdown at the surface, and (b) time of first deflection of signal intensity from zero at z = 5 mm. Power law fits are obtained for $t_2 \propto B^{-1}$ in case (a) and $t_2 \propto B^{-6/5}$ in case (b).

It is not immediately obvious which, if either power law is physically relevant; we must consider the possibility that this second feature represents a phenomenon which originates near the surface and then propagates away from it (case b), although there is no clear sign of such a propagating second feature at z = 0 or z = 10 mm.

Estimates of the electron density can again be made from the resonance to intercombination line intensity ratio R_{ri}. In Fig. (II-15), R_{ri}-1.8 is plotted vs. time for B = 60, 80, and 100 kG at z = 5 and 10 mm from the target surface. At times later than those for which points are displayed, line intensities drop rapidly and the ratio becomes less meaningful; however, it should be noted that no significant change was seen in the ratio for B = 60 kG, z = 5 mm at later times, up to and including the time of the plateau in the resonance line. Ratios obtained from the surface region are smaller than those obtained at z = 5mm; this is more likely a consequence of optical thickness of the resonance line than a real increase in electron density with increasing distance from the target. Time-resolved ratios

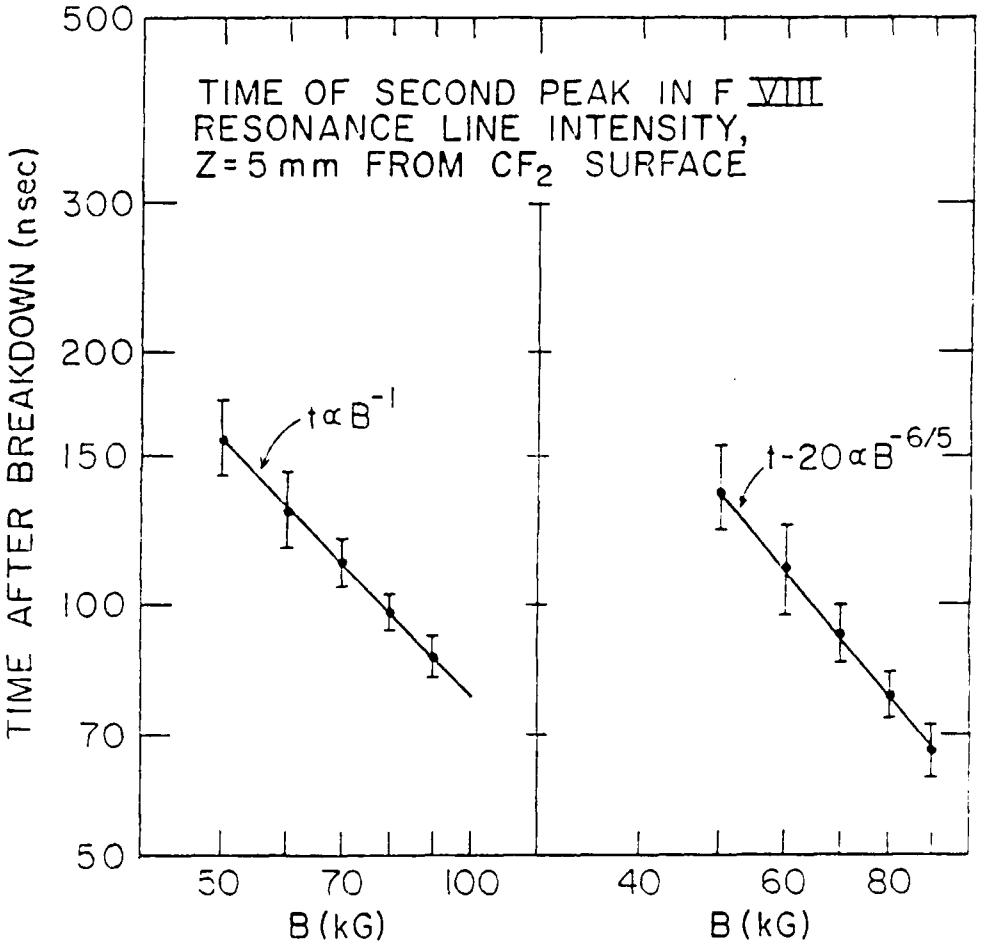

Fig. II-14 Time of the second peak in the resonance line emission versus field relative to the time of breakdown at the surface and relative to the appearance of a signal at 0.5 cm from the surface.

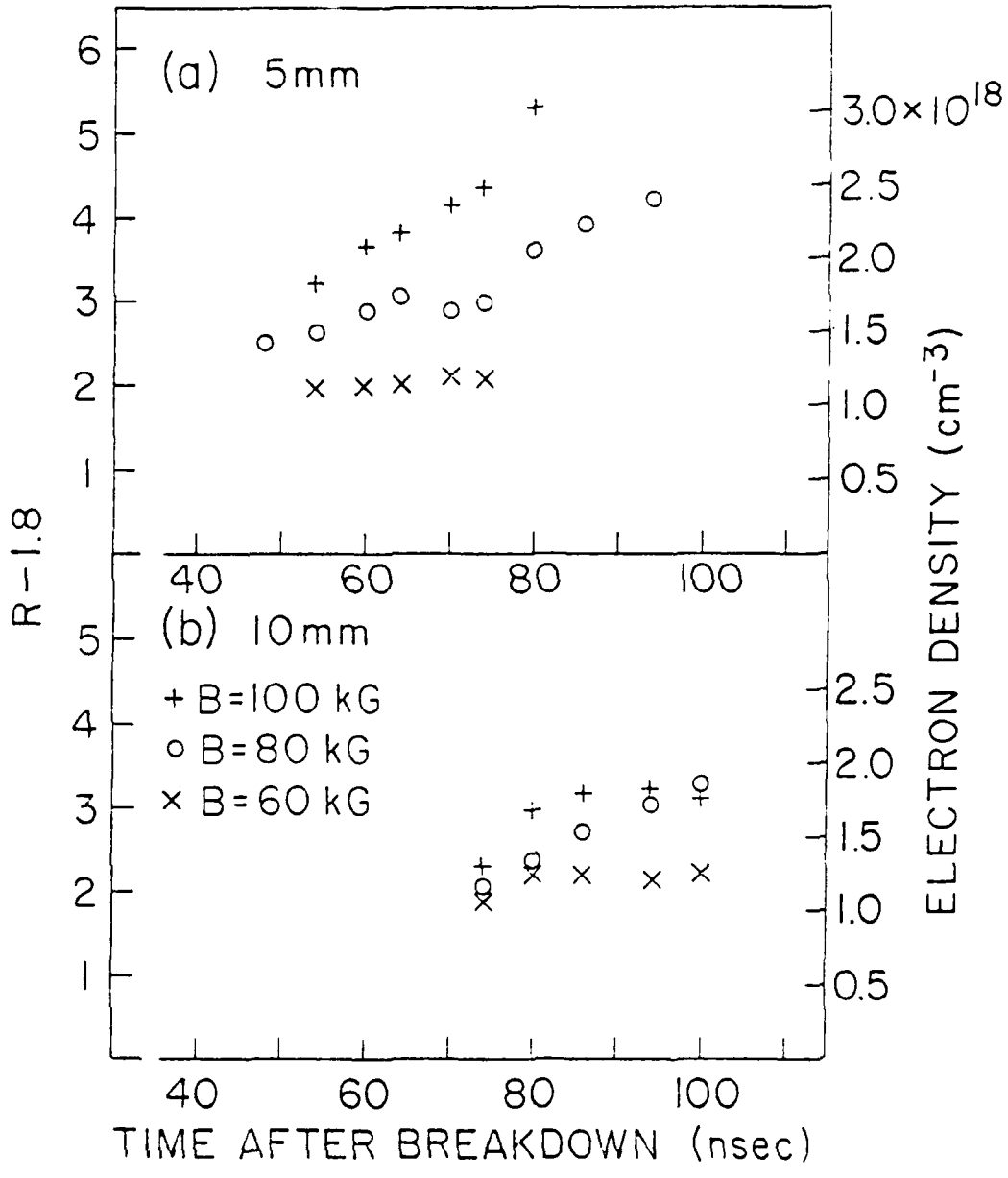

Fig. II-13 F VIII resonance to intercombination line intensity ratios, minus 1.8, observed 5 and 10 mm from CF, surface. Associated values of electron density for T_e = 100 eV at right.

are consistently lower than those obtained from time-integrated spectra.

Estimated electron density, based on a value of $(R_{ri}-1.8)/n_e = 1.75 \times 10^{-18}$ cm^3, is also indicated in Fig. (II-15). This is the value of the Gabriel and Jordan[14] proportionality factor for $T_e \sim 130$ eV; adjustments would be less than $\pm$ 10% for $100 < T_e < 170$ eV. Taken together with values of T_e obtained from the fast diodes, these densities indicate $\beta > 2$ at B = 80 kG.

Time resolved measurements of F IX Lyman α emission were also carried out, although not simultaneously with F VIII $1s3p-1s^2$. Peak intensity is plotted vs. B in Fig. (II-16) at the surface and 3 mm from the surface. Once again line emission intensity is maximized ~ 70-80 kG. Emission at B = 100 kG is seen to be very weak and non-reproducible. F IX line emission appears to decrease more rapidly with increasing distance from the surface than does F VIII line emission.

II.B. Fast X-Ray Diodes

Broadband X-ray emission above 1 keV was monitored with two Quantrad model 100 PIN 250 silicon p-i-n detectors. The diodes were mounted in the focusing box within the hollow of the laser beam, looking end-on at the plasma column 1.5 m away (See Fig. (II-3)). Thus X-ray emission from the entire plasma was detected. The diodes each have an active area of ~ 1.0 cm^2; however, the 31 μm Be window covering one of them was mounted on a holder with an opening of only half that area. Visible light was blocked from the other diode by a 33 μm Be foil covering the entire active area. Risetime of the diodes themselves is about 1 nsec with a bias of

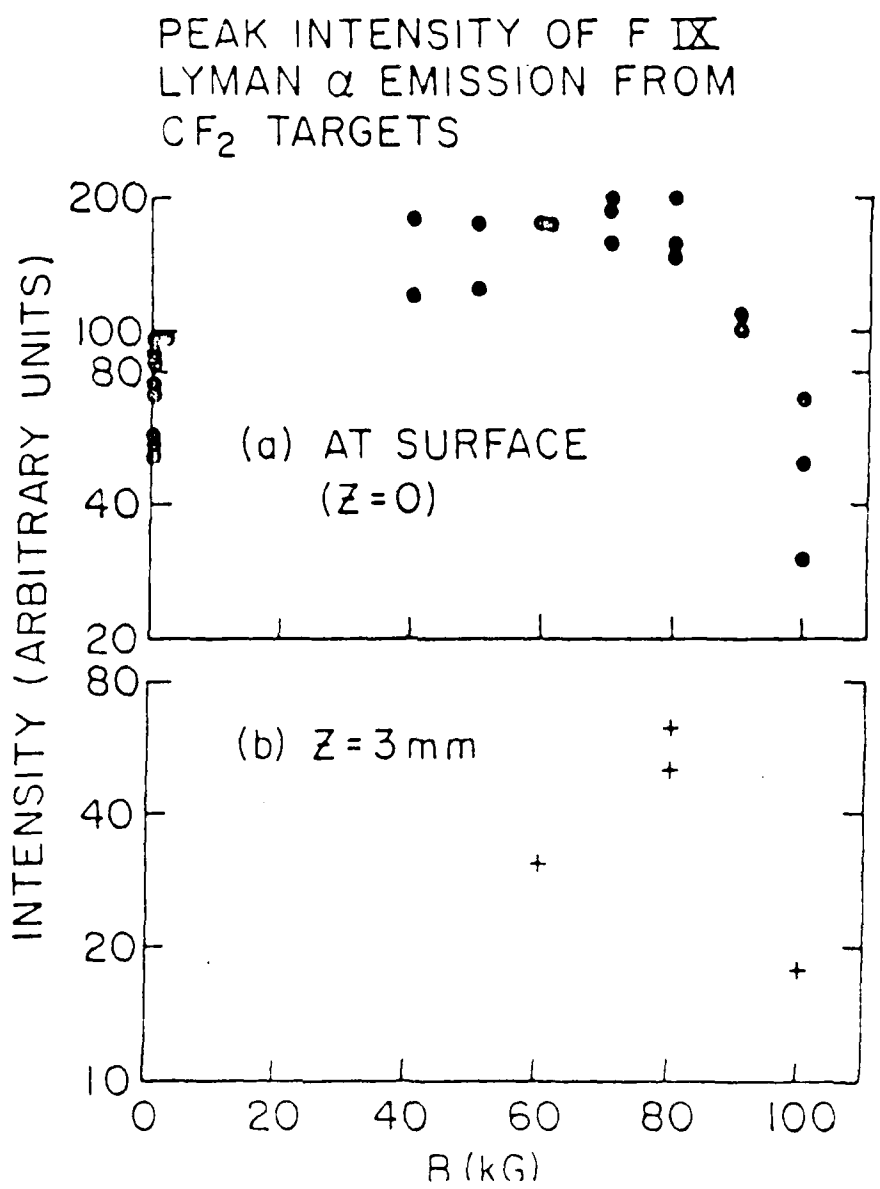
PEAK INTENSITY OF F IX
LYMAN α EMISSION FROM
CF_2 TARGETS
INTENSITY (ARBITRARY UNITS)
200
100
80
40
20
(a) AT SURFACE
(Z = 0)
80
40
20
10
(b) Z = 3 mm
0
20
40
60
80
100
R (kG)

[illegible]

300 volts. Actual time resolution was thus limited primarily by the oscilloscope, which is a Tektronix 7844 operated with 7A16A plug-ins. As both scope and plug-ins have 225 MHz bandwidth, time resolution is thus ~ 3 nsec.

The absolute sensitivity of a p-i-n diode is given by [24]

$$S(E) = \frac{e}{E_{si}} [1 - \exp(-\mu_D d_a)] \exp(-\mu_D d_a - \Sigma \mu_w d_w) \quad \text{Amps/Watt} \qquad \text{(II-21)}$$

where e is the electron charge, E_{si} is the average energy required to create an electron-ion pair in silicon (3.6 eV), μ_D is the Si photoelectric absorption coefficient for photons of energy E, d_a is the thickness of the dead layer (0.8 μm in the present case), and μ_w and d_w the absorption coefficient and thickness of each window. The function S(E) is tabulated. The net output current is then given by

$$I = \frac{A}{4\pi R^2} \int P(E)\ S(E)\, dE \qquad \text{(II-22)}$$

where A is the active area, P(E) the power spectrum emitted by the plasma, and R the distance from plasma to detector. If one then assumes a Maxwellian continuum spectrum, an estimate of the plasma electron temperature (spatially averaged over the entire plasma) can then be obtained by comparing signals from two diodes with different absorber thicknesses. For these experiments, this variation was carried out by placing a 2.27 or 1.2 g/cm^2 CH_2 foil over one of the diodes in addition to its beryllium window. Integration of equation (II-22) was performed by computer to obtain the calibration curves

for T_e vs. the current ratio. Figures (II-17a) and (II-17b) show results of this calculation for CF_2 (recombination edge at ~ 950 eV) and graphite (no recombination edge above 500 eV). Effects of small uncertainties in the Be window thickness are also shown.

The fast silicon diodes were used to monitor spatially-integrated soft X-ray emission from CF_2, LiF, aluminum, and graphite targets, with varying attenuator thickness.

Several interesting features of the signals recorded without additional CH_2 filtering (i.e., Be attenuation only) are observed. With magnetic fields of 50 kG or less, high intensity short duration (as low as 100 nsec FWHM), X-ray bursts are sometimes seen; peak signal strength can vary by two orders of magnitude from shot to shot. Figure (II-18) is a histogram of peak X-ray intensity vs. B from aluminum target plasmas recorded during a single run. Since most of the X-ray emission of aluminum target plasmas is in the form of Al XII line radiation, signal voltage is easily converted to total X-ray power output using equation (II-21) for the diode response and the measured transmission of the X-rays through the 31 μm Be window and 0.8 μm Si dead layer. Maximum observed X-ray signals thus indicate total X-ray energy of about 0.5 joule, and overall conversion efficiency of laser energy to X-rays about 1.5×10^{-3}; however, the maximum observed peak instantaneous conversion efficiency is about .03.

With higher magnetic fields, there is a monotonic decrease in peak intensity with increasing magnetic field. X-ray pulses from aluminum plasmas are always of short duration (~ 30 nsec FWHM), with negligible

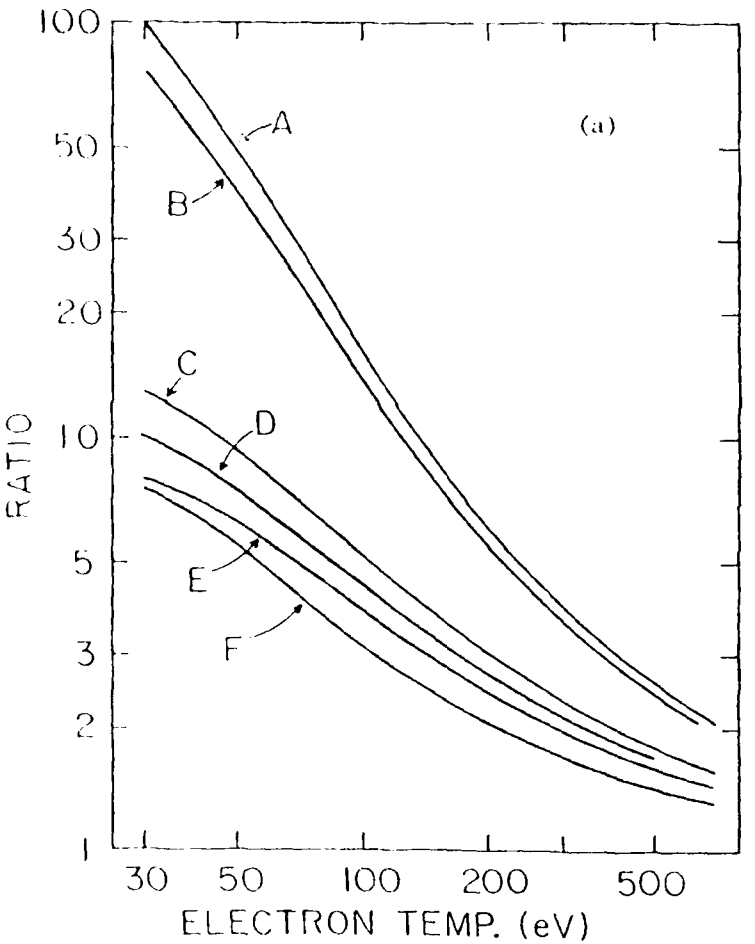

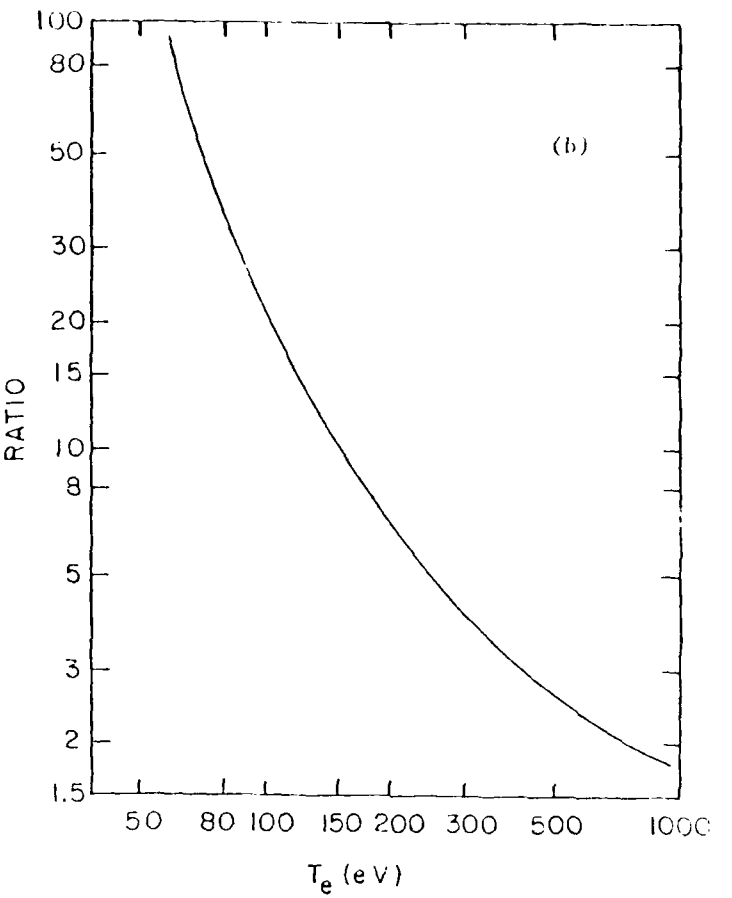

Fig. II-17 Calculated ratios of PIN diode signals versus temperature for (a) CH_2 targets and (b) graphite targets (with 33 μm Be on one and 33 μm Be plus 23 μm CH_2 on the second).

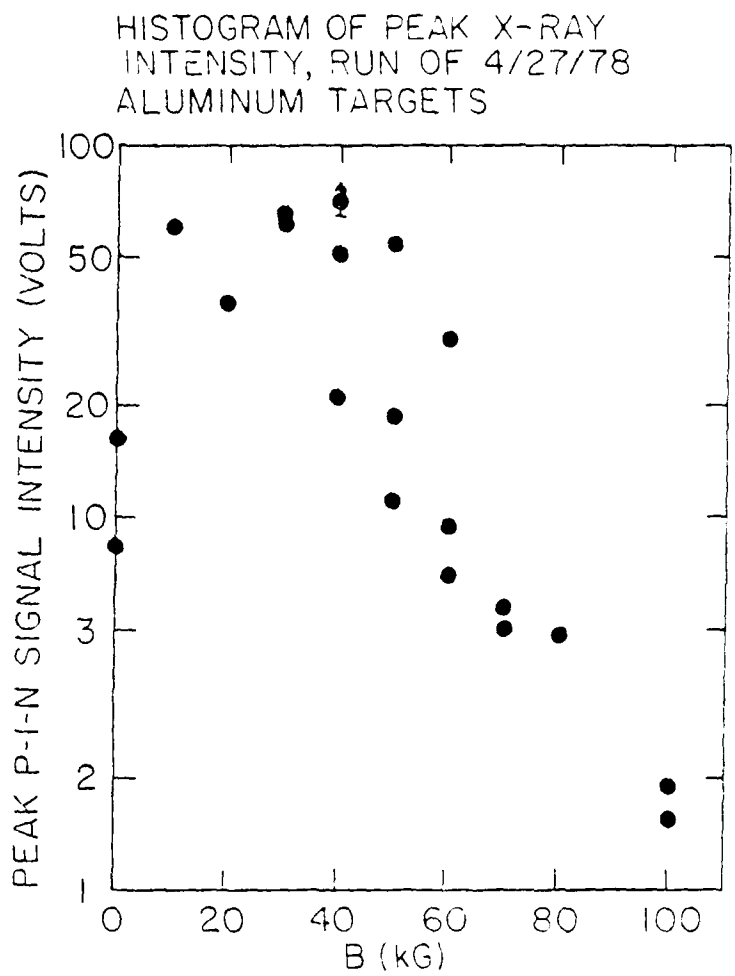

Fig. II-13 Peak X-ray intensity from PIN diodes versus field. 1.0 Volt corresponds to 5 x 10^5 W total X-ray emission into 2π steradians.

intensity recorded after the gain-switched laser spike. However, considerable X-ray flux emerges from teflon target plasmas during the tail of the laser pulse. In Fig. (II-19) intensity is plotted vs. B for several times after breakdown. Emission beyond the peak of the X-ray pulse is maximized for B = 80 kG; and a prominent shoulder is seen in the X-ray emission at B=80 kG, but not at B = 100 kG at about 40 nsec after the peak. However, a greater percentage of the total X-ray output comes during the tail of the laser pulse with B = 100 kG than with B = 80 kG. Emission from graphite targets is of intermediate duration between that from CF_2 and that from aluminum, and is less intense than either. A small amount of data was taken with LiF targets at B = 80 kG. The X-ray intensity was about 20% below that of CF_2, with no obvious change in temporal structure.

When a polypropylene absorber is placed in front of either diode in addition to the 31 or 33 μm Be foil, high frequency oscillations are observed during the first 100 nsec of the X-ray pulses emitted by teflon target plasmas in the presence of strong magnetic fields. The amplitude of these oscillations usually exceeds the upper limit for any oscillations on the diode having no CH_2 filter; in some cases the signal becomes negative. Further evidence that these oscillations are probably not simply pickup was obtained when operating bias voltage was reduced to 50 volts and the oscillations disappeared. (Reducing bias voltage from 300 to 50 volts lengthens the response time to greater than 10 nsec). The frequency of the oscillations is usually about 150 MHz, about the same as that of the laser mode-locking.

AD-A084 201 MASSACHUSETTS INST OF TECH CAMBRIDGE FRANCIS BITTER --ETC F/G 20/9
LASER-PRODUCED PLASMAS AND RADIATION SOURCES.(U)
JAN 80 D W SCUDDER, H C PRADDAUDE F44620-76-C-0002
UNCLASSIFIED AFOSR-TR-80-0335 NL

2 OF 2
AD
AD84201

END
DATE FILMED
6-80
DTIC

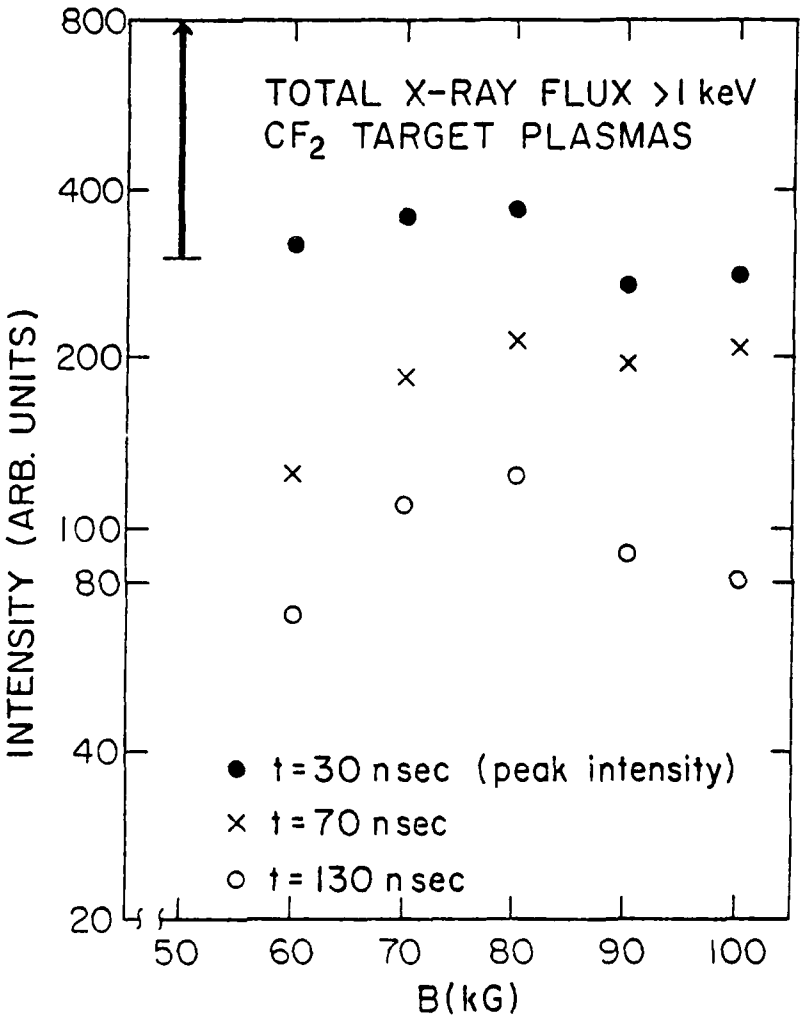

Fig. II-19 PIN signal level in millivolts at various times after breakdown. Conversion of signal level to X-ray emissivity not straightforward for CF_2. Peak intensity often is very large for B< 60 kg.

The primary motivation for using the CH_2 filters is to obtain an estimate of the electron temperature. Figures (II-20) and (II-21) are plots of CF_2 plasma electron temperatures vs. time for various magnetic fields based on the calibration curves of Fig. (II-17a). For Fig. (II-20), diode 31 (that is, the diode with the 31 μm thick Be window) had no CH_2 filter, and diode 33 was covered with 1.2 mg/cm^2 or 2.27 mg/cm^2 of CH_2. Values of the diode 33 signal were obtained by taking the mid-point of the oscillations at $t < 100$ nsec. (At times earlier than those displayed, the oscillations totally dominated the signal). Fig. (II-21) was obtained by comparison of signals from Diode 33 observed during different runs with different CH_2 thickness (1.2 or 2.27 mg/cm^2, as above). That is, ratios of the ratios used for the values of T_e in Fig. (II-20) were also used to deduce electron temperatures. Only shots with similar diode 31 signals were analyzed in this manner; sufficient data for this purpose was obtained only for B = 80 kG and B = 100 kG.

Values of T_e obtained with different pairs of absorber thicknesses increase strongly with increasing absorber thickness, indicating a very non-Maxwellian spectrum. Despite the data used for Fig. (II-21) coming from different runs, the electron temperatures plotted there probably bear the closest resemblance to reality for the following reasons:

1. 31 μm of Be is not enough to completely exclude line emission. Transmission is still 1.44% at the F IX - F VIII recombination edge (954 eV). An increase in "apparent temperature" at times shortly after the peak of the X-ray pulse may be a manifestation of this. It is possible that the more intense "harder" X-ray emission at early times may be counter balanced by the F IX line radiation which occurs mainly in the first 30 nsec.

2. Comparison of the two diodes introduces uncertainties of its own. One would expect the signal ratios to be nearly constant in time when diodes having different absorbers record X-ray emission from aluminum plasmas.

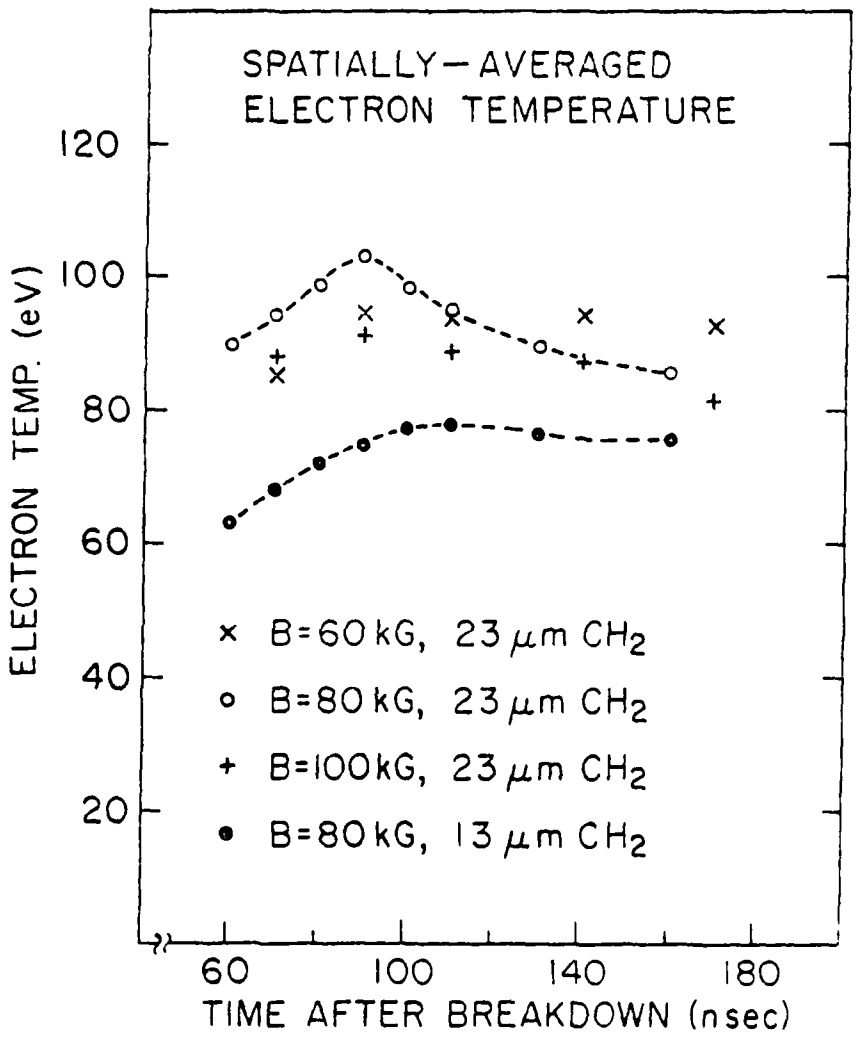

Fig. II-3. Estimates of electron temperature obtained for direct comparison of signal strengths recorded by two PIN diodes, one of which has no CH_2 foil.

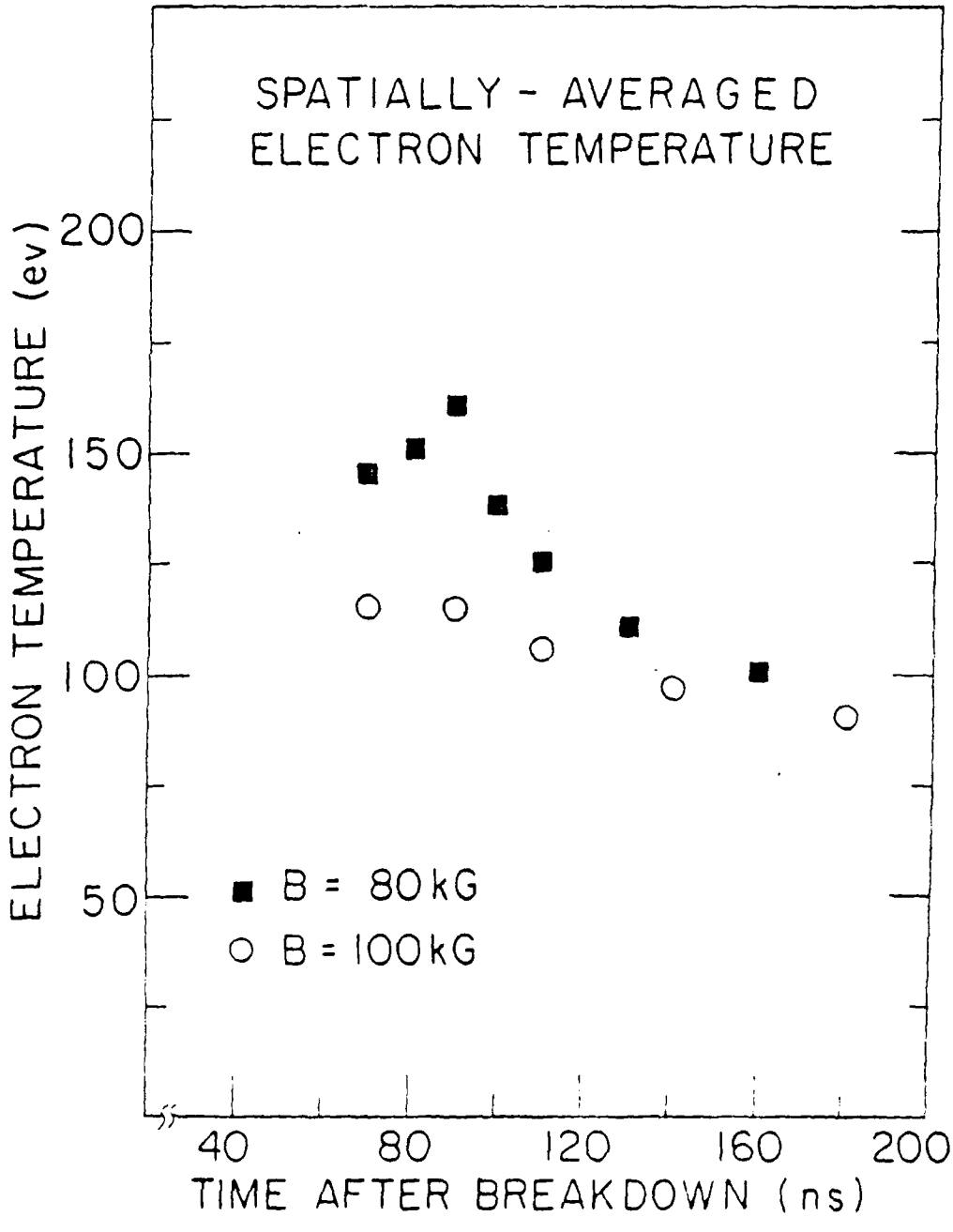

Fig. II-21 Electron temperatures of CF, plasmas obtained by comparison of signal levels recorded by diode 23 with 13 and 23 m thick CH, filters.

Not only is this not the case, but sometimes the ratio indicates average X-ray energies well below the Al XII resonance line energy of 1.6 keV.

Figure (II-21) shows T_e to be substantially greater with B = 80 kG than with B = 100 kG. The increase in T_e from 145 eV at 70 nsec to 160 eV at 90 nsec for B = 80 kG corresponds to an increase in the average flux of harder X-rays during the shoulder of the non-CH_2 diode signal.

X-ray emission from graphite target plasmas recorded with 2.27 mg/cm^2 of CH_2 over diode 33 was even more heavily dominated by oscillations than that from teflon. Comparison of peak emission at B = 80 kG, in conjunction with the calibration curve indicates an early electron temperature of 200 eV.

II.C. X-Ray Imaging

Two imaging systems for time-integrated flux were constructed: a pinhole camera utilizing one of the magnet's radial access ports, and a collimator plate set-up inserted in the experimental cell. Both are diagrammed in Fig . (II-22).

The pinhole camera assembly consists of an evacuated pipe with a Nikonos III underwater camera body at one end, and, inserted into the other end, a narrower pipe on which the window and pinhole are mounted. The length of the inner pipe was chosen such that the length of plasma imaged onto the film was maximized. The primary constraints were the dimensions of the access port, finite thicknesses of the pipe walls, and maximum image size recordable with the camera. The pinhole and film are respectively 3" and 12" from the plasma, for an image magnification of three. Up to 8 mm of the plasma column can be imaged on a single shot. Recording the full diameter is simply a matter of alignment. The 35 mm film is Kodak 2490.

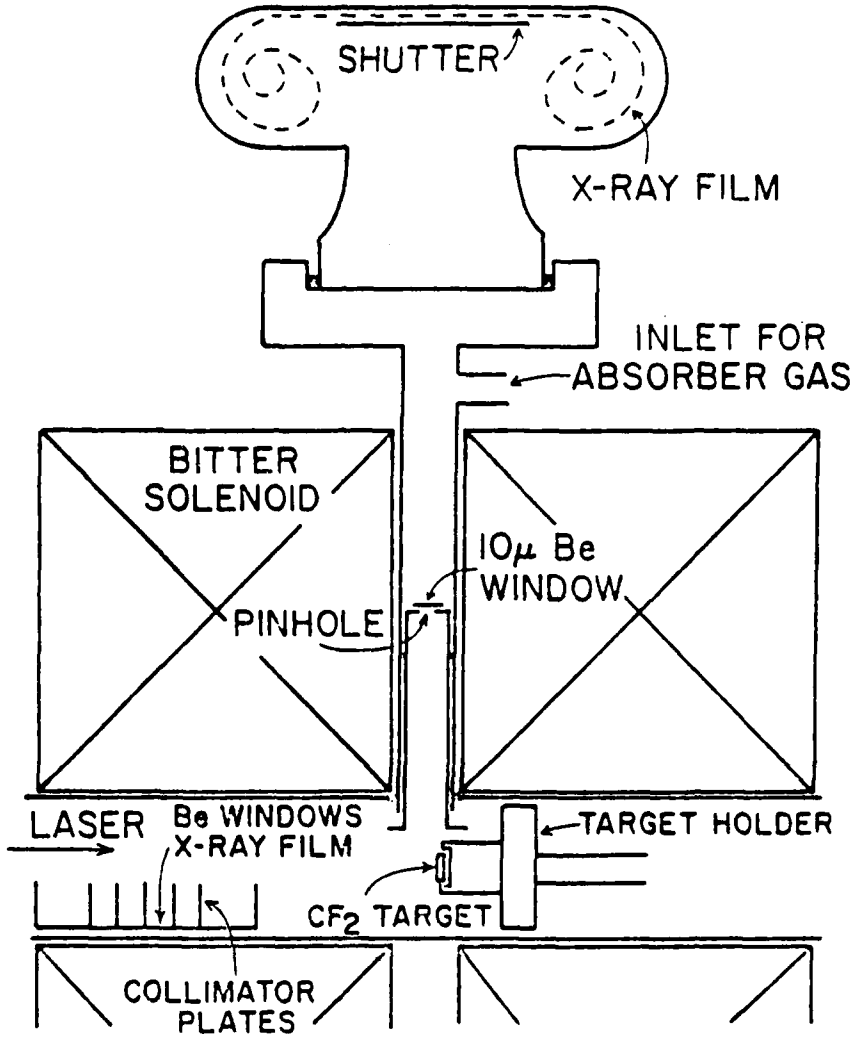

Fig. II-22 Schematic of the X-ray pinhole camera and the collimator plate set-up.

Pinholes of 50 μm and 200 μm were used behind a 10 μm Be window for experiments reported here. The pinhole assembly includes an O-ring seal between inner and outer pipes and a gas inlet between the pinhole and film. Spectral information could thus in principle be obtained by the differential gas absorber method. However, the complex dependence of the film sensitivity on X-ray energy would make interpretation difficult, so no absorber gas was used.

The total length of the X-ray emitting region of the plasma was estimated using an X-ray filmpac mounted under a set of collimator plates within the experimental cell. The mount is a half-cylindrical shell into which grooves were cut for the collimator plates. The film-holder is simply a piece of aluminum foil into which holes were cut at 1 cm intervals and then covered with Be foil. With five collimator plates spaced 1 cm apart being run on a given shot, film underneath the windows could respond to X-rays from a segment of the plasma column up to two cm long. Since replacing the film requires removing the cell from the bore of the magnet (and this is a very time consuming operation if other X-ray diagnostics are plugged into the cell), this diagnostic was used rather infrequently.

200 μm pinhole pictures were taken of teflon, aluminum, and graphite target plasmas. One shot is sufficient to adequately expose the film when imaging the target surface region. Up to 2 cm from the surface 200 μm pinhole photographs were taken of the teflon target plasma column with exposure on four shots. With a 50 μm pinhole, images were obtained of the surface and nearby regions of teflon plasmas by integrating over twelve shots.

Perhaps the most striking aspect of the X-ray imaging studies is the effect of magnetic field on the time-integrated radial emission profile at the target surface, and its variation with target material. Figure (II-23) consists of microphotometer traces obtained by scanning the surface (most intense) section of various pinhole photographs perpendicular to the magnetic field axis. The scanning beam was 0.3 mm ($\parallel\vec{B}$) x 3 μm ($\perp\vec{B}$), corresponding to a 0.1 mm x 1 μm section of the plasma. At zero field the diameter is about the same for all three target materials. With graphite, no radial expansion is seen as the magnetic field is increased to 100 kG; peak film density increases with increasing field. For teflon targets, the diameter of the bright surface region (corrected for film non-linearity) expands from 0.6 mm to 1.7 mm FWHM as the magnetic field is increased from 0 to 100 kG; this is plotted in Fig. (II-24). Furthermore, peak intensity decreases with magnetic field, as shown in Fig.(II-25). These effects are even more pronounced for aluminum targets; not only does the image become dimmer and wider with increasing magnetic field, but a deep on-axis minimum also appears in the emission profile when the magnetic field exceeds 30 kG. At B = 60 kG, the intensity from the on-axis minimum is about 40% of the average of the two peaks. The separation of the peaks is 1.4 mm which is much greater than the focal spot size (~ .4 - .5 mm), and the diameter (based on the intensity at the on-axis minimum) is 2.3 mm.

Microphotometer scans parallel to $\overline{B}$ show that the on-axis minimum does not persist very far from the surface. With graphite and aluminum targets, time-integrated intensity drops very rapidly as one moves away from the

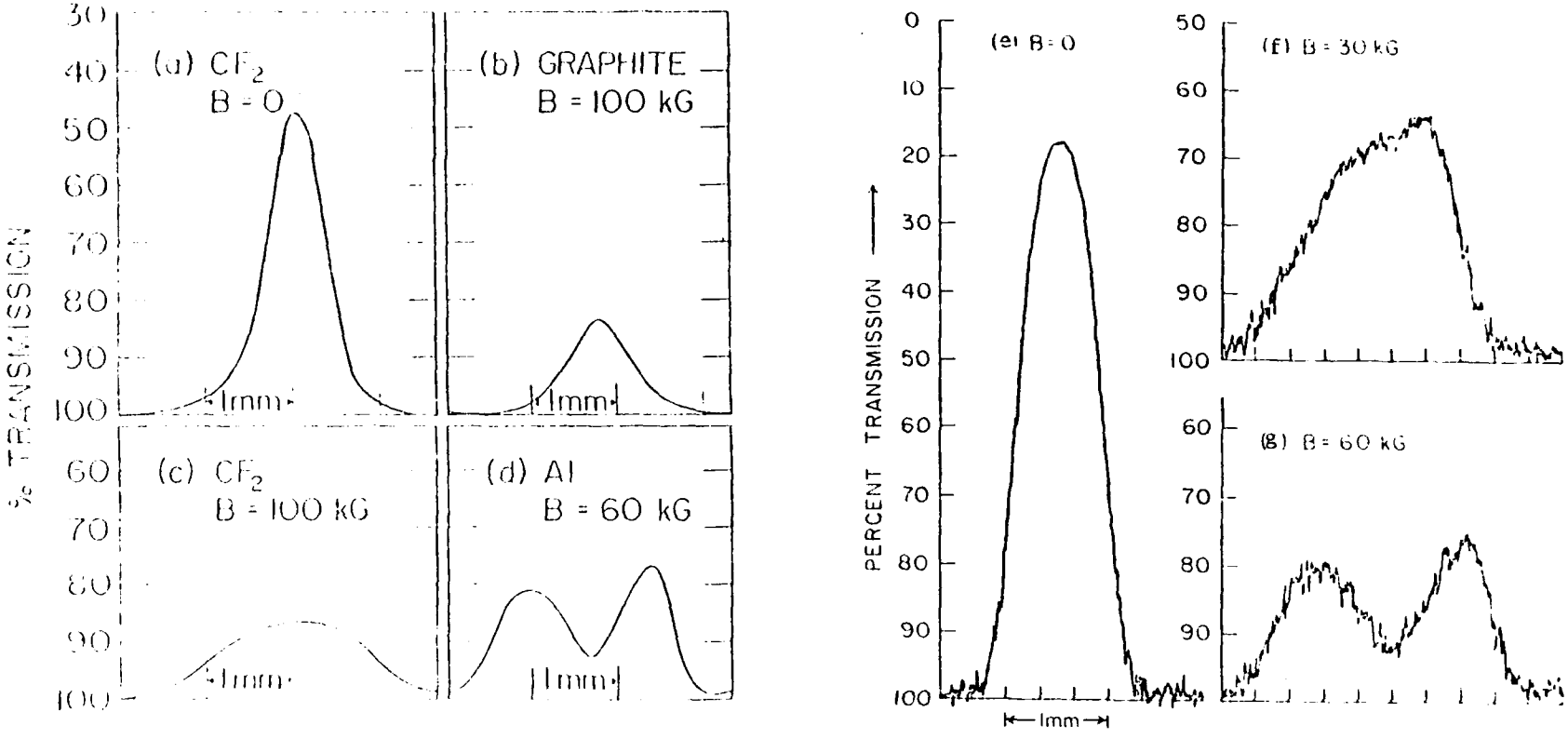

Fig. II-23 Microphotometer scans of 200 μm X-ray pinhole photographs, at target surface, perpendicular to magnetic axis. The diameters are about equal for all three target materials with B = 0. Each photograph represents one shot. (a) and (c) are with CF_2 targets, (b) is with graphite, and (d) - (g) are with Al.

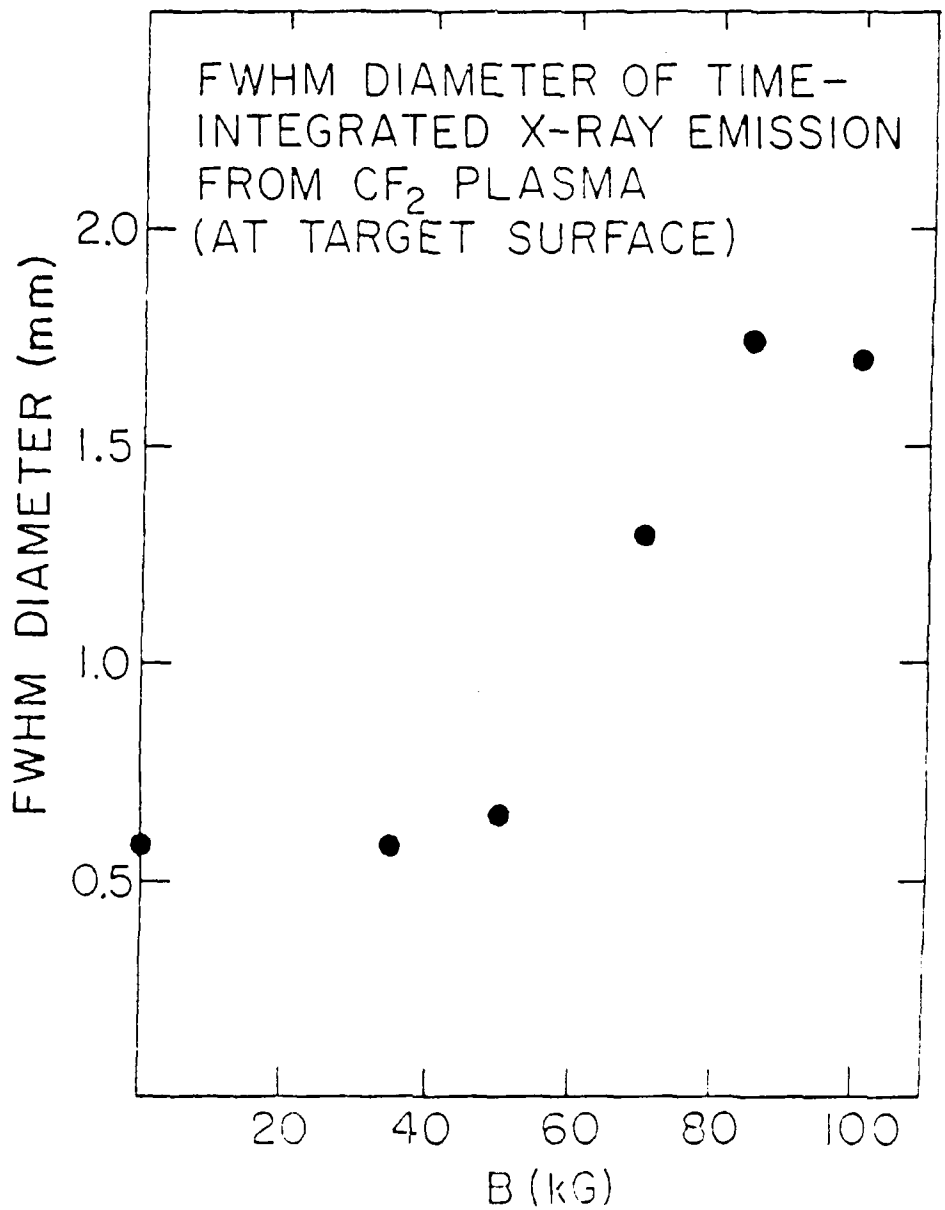

Fig. II-24 Diameter of X-ray emission profile vs. B obtained from surface region of 50 μm pinhole photographs of CF_2 plasmas.

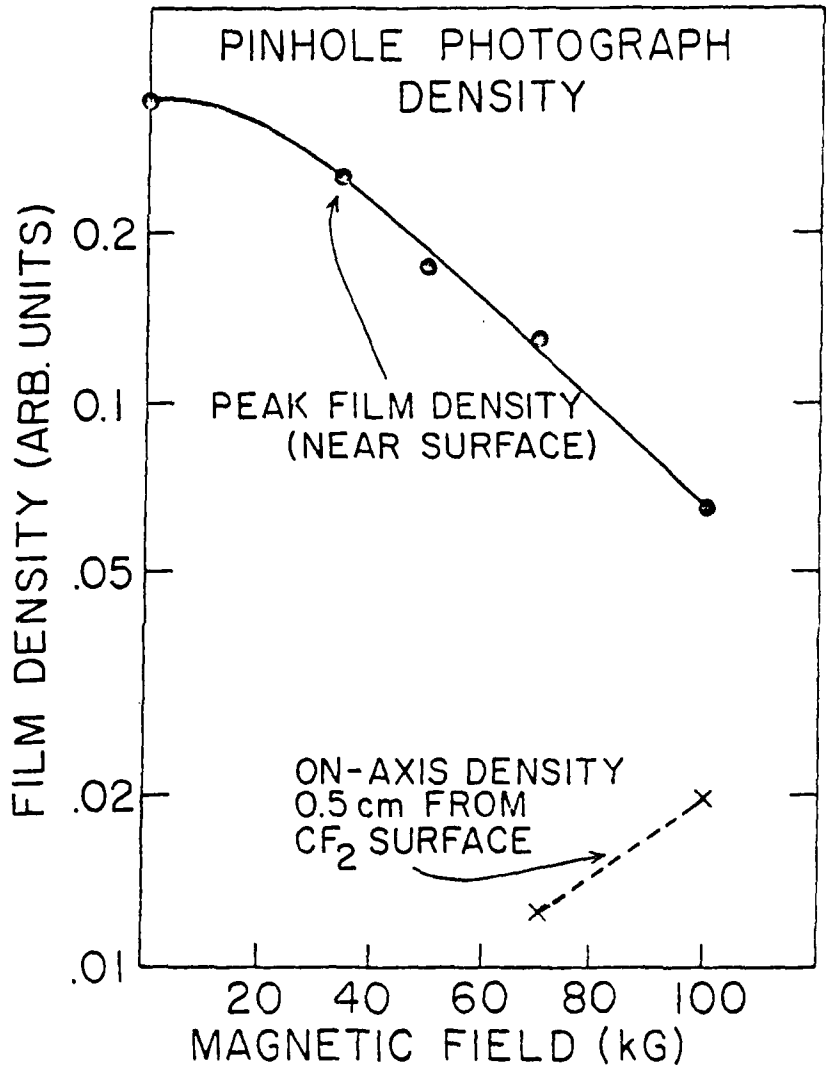

Fig. II-25 Maximum photographic density observed on 50 μm pinhole photographs of CF_2 target plasmas after 12 shots.

surface for all magnetic fields. With no magnetic field, the width of the emission peak appears to be 0.3 mm FWHM for aluminum targets. This indicates a very small emission region, since the pinhole size is 0.2 mm.

With CF_2, however, with magnetic fields stronger than 50 kG considerable X-ray emission is seen at distances greater than 2 mm away from the surface. This increases with B up to about 80 kG. Indeed, when very strong magnetic fields are present a local maximum is seen in the axial emission profile ~ 3 mm from the surface. At the axial position of the local miximum, the radial profile is more strongly peaked on axis than elsewhere.

When the collimator plate system was used with teflon targets, the plasma column caused saturation of the film up to 12 cm from the surface when fields of 50 kG or greater were applied. No exposure was seen with B = 0 or B = 25 kG at 4 cm from the surface. Saturation was not observed with aluminum targets.

II.D. Conclusion

In conclusion, several useful X-ray diagnostics of solid target plasmas have been built and demonstrated. Spectrographic techniques have provided the space and time resolved electron density in fluorine plasmas, and somewhat less reliably the temperature. The space integrated temperature has been observed with X-ray continuum detectors. Finally, X-ray imaging has allowed the spatial distribution of the luminous plasma to be determined.

III. Schlieren Photography Density Diagnostic

An extremely powerful class of diagnostic techniques for measuring plasma density involves photography using light transmitted through a plasma. This class includes schlieren photography and interferometry of which double-pulse holographic interferometry[25] is just one variation. These techniques have in common their use of optical phase front distortion introduced into a beam by the plasma to somehow modulate an image which provides two dimensions of spatial resolution. For the most part the results are easy to analyze and do not depend on the plasma temperature, assumptions about equilibrium, or poorly known coefficients, all of which plague spectroscopic techniques. These advantages coupled with the good time resolution possible with pulsed laser sources are responsible for the popularity these techniques have enjoyed in recent years.

Schlieren photography utilizes the lensing effect of density gradients to deflect part of a collimated beam. When the beam is subsequently focused on a slit the deflected part is blocked. Thus a schlieren photograph consists of an image of the plasma in which regions of significant gradient are dark and the rest of the image is light. By measuring relative darkness quantitative information can be obtained. The choice of a schlieren system rather than, say, a holographic system for use with this experiment was largely dictated

by economic considerations. The schlieren system requires a bright, short-pulse source, but its mode quality and coherence need not be nearly so good as an interferometric system requires. Thus an inexpensive "home made" gas laser can be used rather than an expensive, "holographic quality" solid state laser.

In this chapter we will describe the nitrogen laser used as the source, the schlieren camera, and the analysis of the schlieren photographs.

A. Nitrogen Laser

A nitrogen laser was chosen as a source for these studies because it is easy to build and has a short pulse length, of 10 nsec FWHM, compared to the CO_2 pulse length and the characteristic times for plasma motion. Originally it was planned to use the laser on the 5401 Å transition of neon rather than the ultraviolet nitrogen line. This laser transition has a pulse length comparable to nitrogen and has the advantage of being in the visible part of the spectrum. However, it was found to be much weaker than the nitrogen transition and thus could not be used.

The design of the nitrogen laser initially followed a very familiar parallel plate Blumlien design giving a transverse discharge along a 110 cm cavity. This design was subsequently modified to reduce the triggering inductance and to provide a true traveling

wave excitation. The final design consists of a Blumlein circuit made from 26 lengths of coaxial cable (RG8). The braid of each cable is separated at approximately midway along its length and connected to either side of the laser cavity. The center conductors are charged to high voltage, typically 20 kV, then shorted to the braids at one end of the cables through a common spark gap. The resulting voltage pulse travels along the braids to the laser cavity, where a Blumlein erection occurs. The distance that the pulses must travel to reach the cavity is graduated along the cavity, so that the voltage wave moves along the cavity at the speed of light.

The voltage rise time of the circuit is estimated to be 4 nsec compared to 50 nsec for the parallel plate system. The cables are 3.05 m long giving a 15 nsec pulselength to match the natural 10 nsec laser pulselength.

The cable discharge laser produces pulses of 200 μJ compared to 900 μJ for the parallel plate system. However, the beam divergence improves dramatically with the cable system going from 3.3 mrad to 1.3 mrad perpendicular to the discharge (the beam is a rectangle elongated parallel to the discharge).

A schematic diagram of the laser is shown in Fig. (III-1), and the laser characteristics are shown in Fig. (III-2). Fig. (III-3) is an electrical schematic of the laser circuit.

The cable discharge laser design is inherently much safer

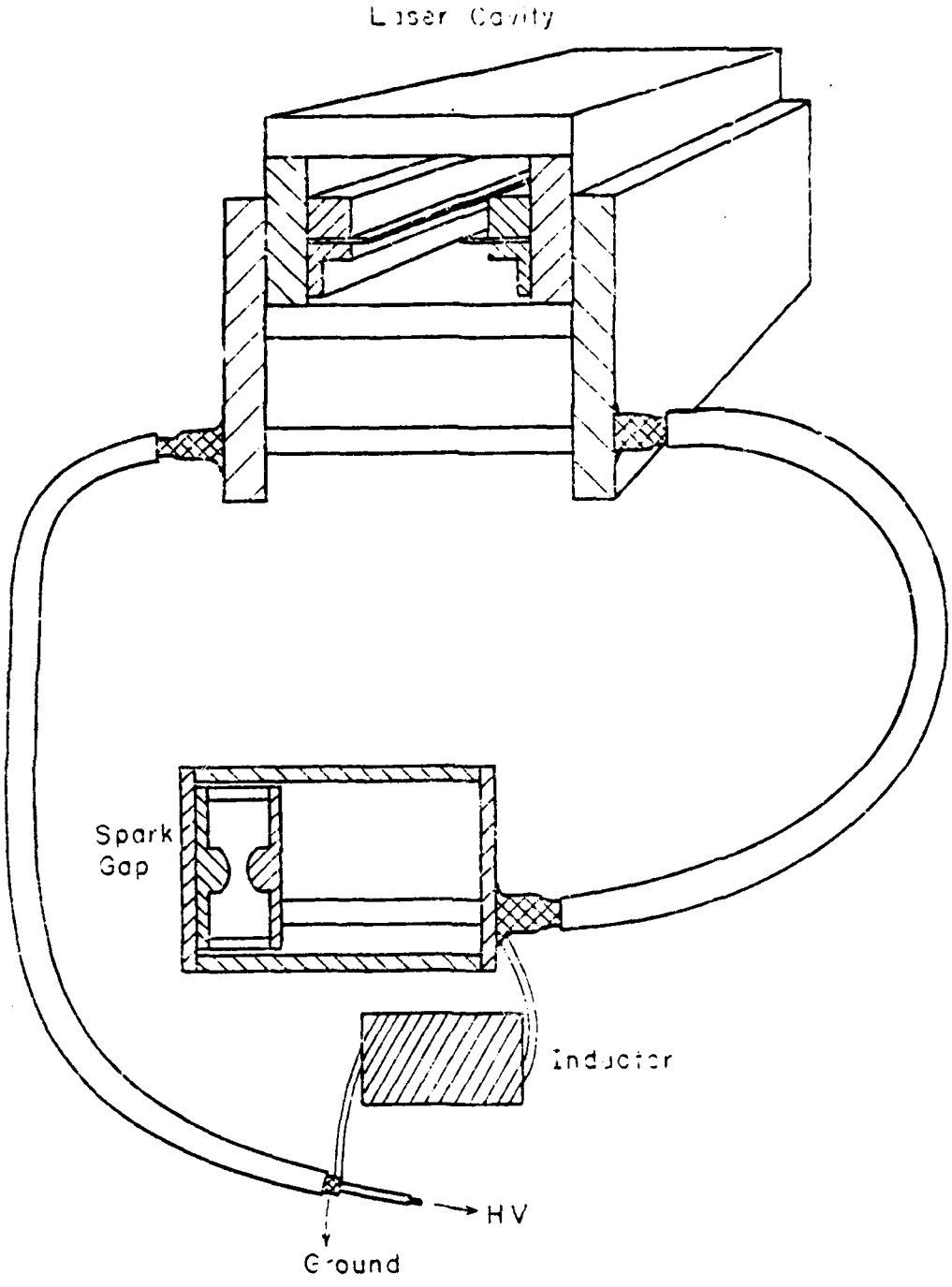

Fig. III-1 Schematic diagram of the nitrogen laser showing the cable discharge system and its connection to the cavity.

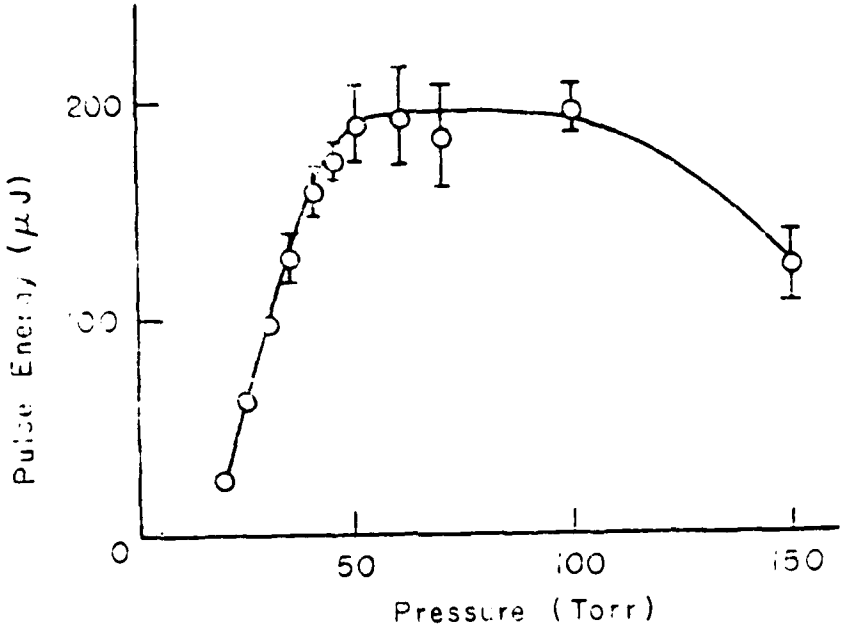

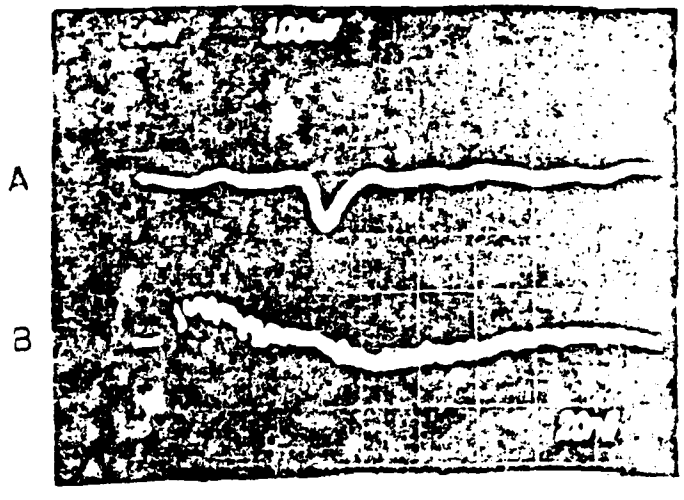

Fig. III-2 Laser characteristics. The output energy as a function of the pressure, and the oscilloscope trace showing the temporal profile of the pulse.

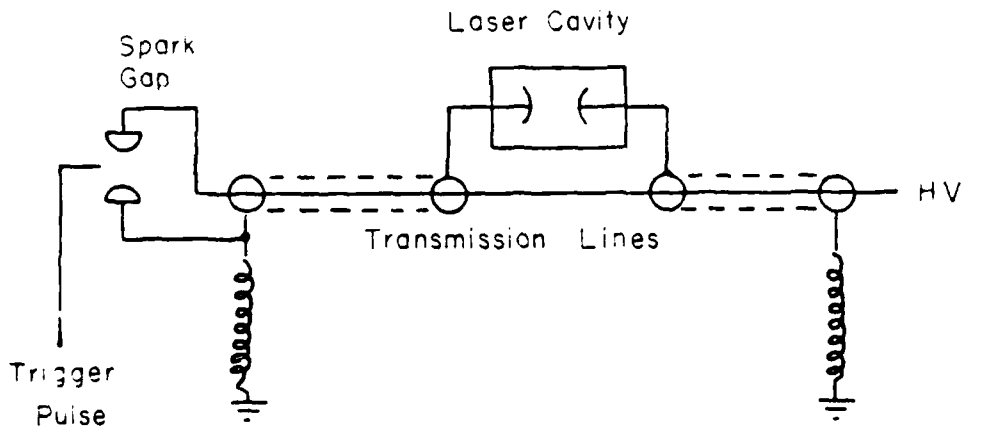

Fig. III-3 Electrical schematic of the laser excitation circuit.

than the parallel plate system, making it much more attractive for experimental use.

B. Schlieren Camera

A schematic of a schlieren system is shown in Fig. (III-4). A beam of light, in this case from a laser, is focused onto a ground glass diffuser and an input slit located at the focal plane of a second lens. The light that passes through the slit expands to the lens which approximately collimates the beam. The collimated beam passes through the plasma and through a third lens which focuses it onto a second slit, at its focal plane, thus forming an image of the input slit. The film plane is located beyond the second slit at the image plane of the plasma.

Any rays which are deflected by the plasma will not be imaged directly onto the second slit. Thus the illumination of that part of the image field will be attenuated, and that part of the plasma will appear dark in the photograph. If the deflection angle of a ray is ε, at the second slit it will be moved a distance $\Delta = \varepsilon f_3$ where f_3 is the focal length of the third lens. The relative brightness at the film plane due to deflected rays compared to undeflected ones will be $I_d/I_o = (S - \Delta)/S$ where S is the slit width.

A diagram of the schlieren camera is shown in Fig. (III-5). The optical components are mounted on an aluminum plate which is

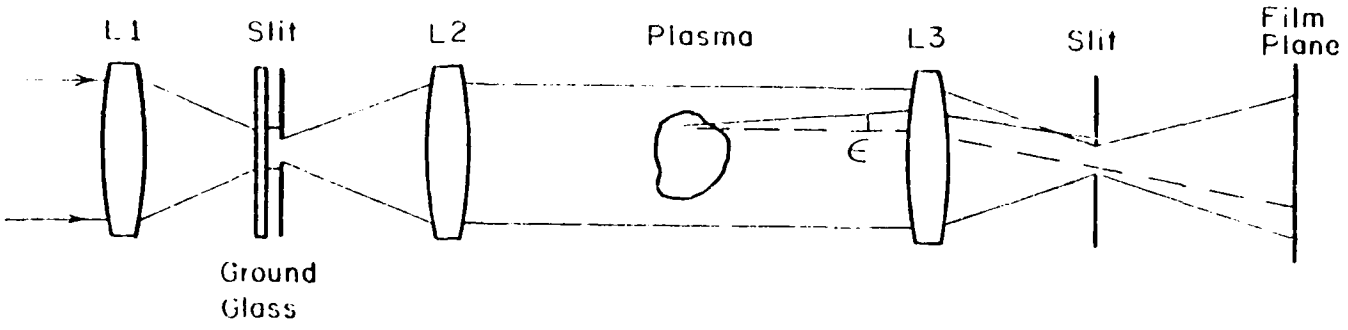

Fig. III-4 Schematic of a typical schlieren system.

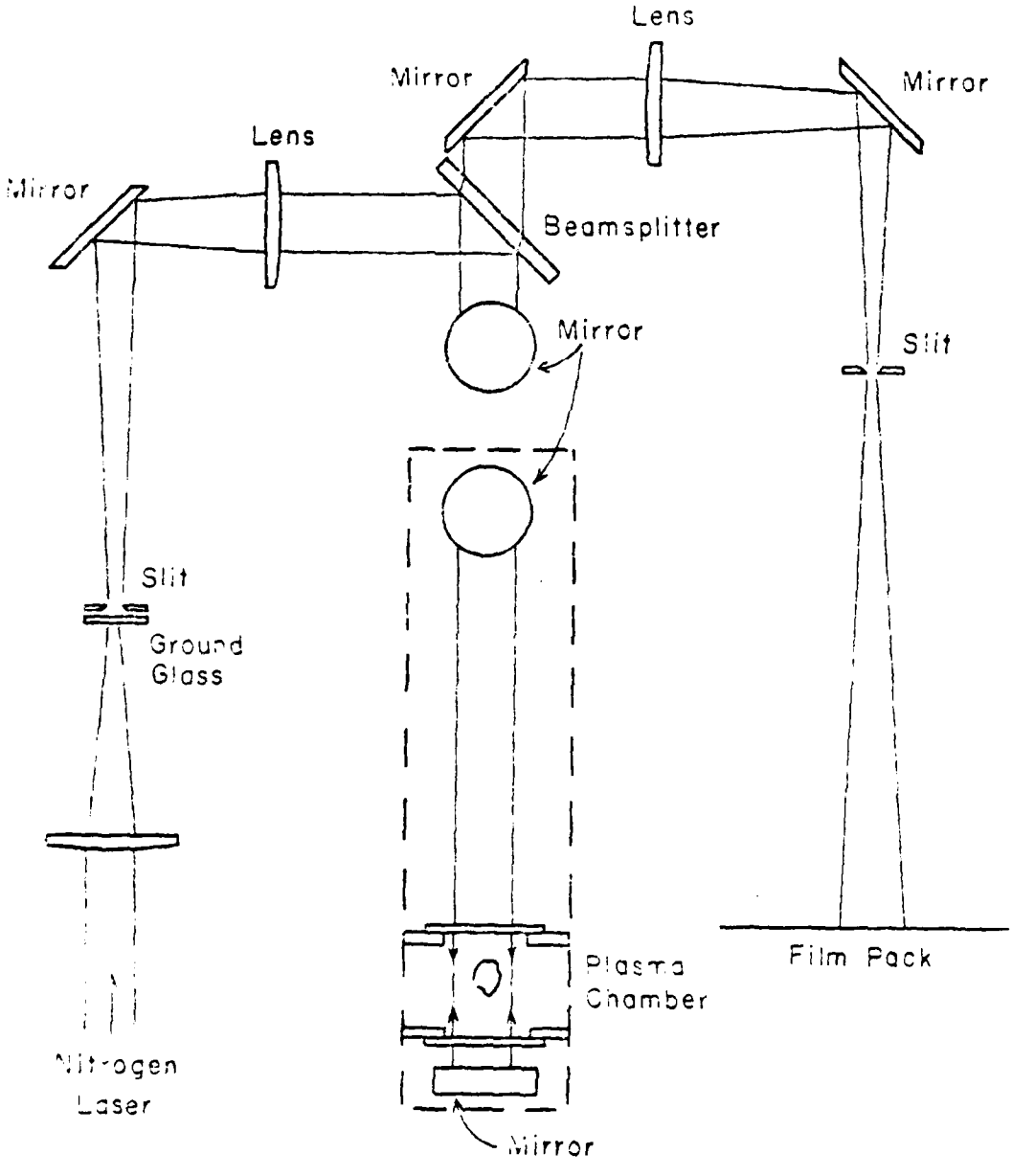

Fig. III-3 Experimental arrangement of the schlieren camera. The insert shows the part of the optical path perpendicular to the plane of the rest of the figure.

clamped atop the Bitter solenoid in which plasmas are generated. After passing through the first slit and being collinated by the second lens the beam is incident on a beamsplitter. The transmitted part of the beam (50%) is discarded, and the reflected part is directed down (into the plane of the page in Fig. (III-5) through vacuum windows on the plasma cell. A mirror below the cell reflects the beam back through the cell along the same path to the beamsplitter where now the transmitted part is used to take the picture. Beyond the second slit an interference filter is used to attenuate radiation from the luminous plasma. A Polaroid(R) film pack at the image plane is used with type 665 negative-positive instant film. This is a medium contrast continuous tone film with ASA75.

The radiation from the plasma is significant and measures had to be taken to minimize fogging of the film. The use of a second slit rather than a knife-edge at the focal spot of the third lens is the most important measure, since it makes the effective f/ number for collecting plasma light very large (~ f/400). Also, the laser line filter eliminates nearly all of the plasma light not in a narrow spectral range near the laser wavelength. Finally, a horizontal slit was added to the vertical slit to further restrict the collection angle. Of course the horizontal slit had to be much wider than the vertical one; it

was 5 mm compared to 200 μm.

Even with these measures the plasma luminousity exposed the central 4-5 mm^2 of the image. A further measure which could further attenuate the plasma emission would involve a fast electro-optic shutter which could limit the exposure to 15 - 20 nsec. Such a shutter was, however, not available.

C. Analysis of the Data

A number of schlieren photographs were obtained in the plasma geometry used in the stimulated Brillown backscattering study described in Chapter I. All of the schlieren photographs were taken at zero magnetic field in 11 Torr of nitrogen.

1. Qualitative Results

Fig.(III-6) shows several photographs taken at various times after initiation of the laser pulse. The dark cylinder coming into the bottom of the pictures is a threaded tube through which the CO_2 laser beam enters the plasma chamber. The breakdown initiates at a 3 mm orifice at the upper end of the tube. The bright region adjacent to the orifice is due to plasma radiation.

The plasma is seen to move outward rapidly after being heated by the laser pulse forming an approximately hemispherical

Fig. III-6 here

S18—10/2

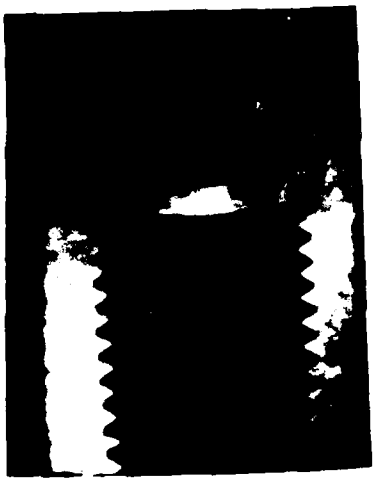

S12—10/2

S12—10/1

S 2—10/1

shock or blast wave. Apparently, significantly lower plasma densities persist behind the shock than are present in it or in the original breakdown. This is indicated by a bright line visible in some of the shocks caused by a change in direction of the density gradient.

2. Quantitative Results

Schlieren photography is best suited for studying strong discontinuities such as the outgoing shock waves in the pictures of Fig. (III-6). The diameter of the plasma was measured from a series of shots perpendicular to the CO_2 laser beam in a plane 1 mm from the orifice. These diameters are plotted in Fig. (III-7) as a function of time after the initial breakdown.

The solid curve in Fig. (III-7) is a best fit to the data assuming that the blast wave radius varies as $R \propto t^{2/5}$, which is the theoretical dependence for a spherical blast wave[26]. The best fit is

$$d = 605(\text{cm sec}^{-2/5})t^{2/5} \qquad \text{(III-1)}$$

Ideally, the coefficient in Eq. III-1 could be used to extract the energy deposited in the gas by the laser. However, the observed shock is so strong that it gives rise to a significant degree of ionization which invalidates the simple hydrodynamic model. For

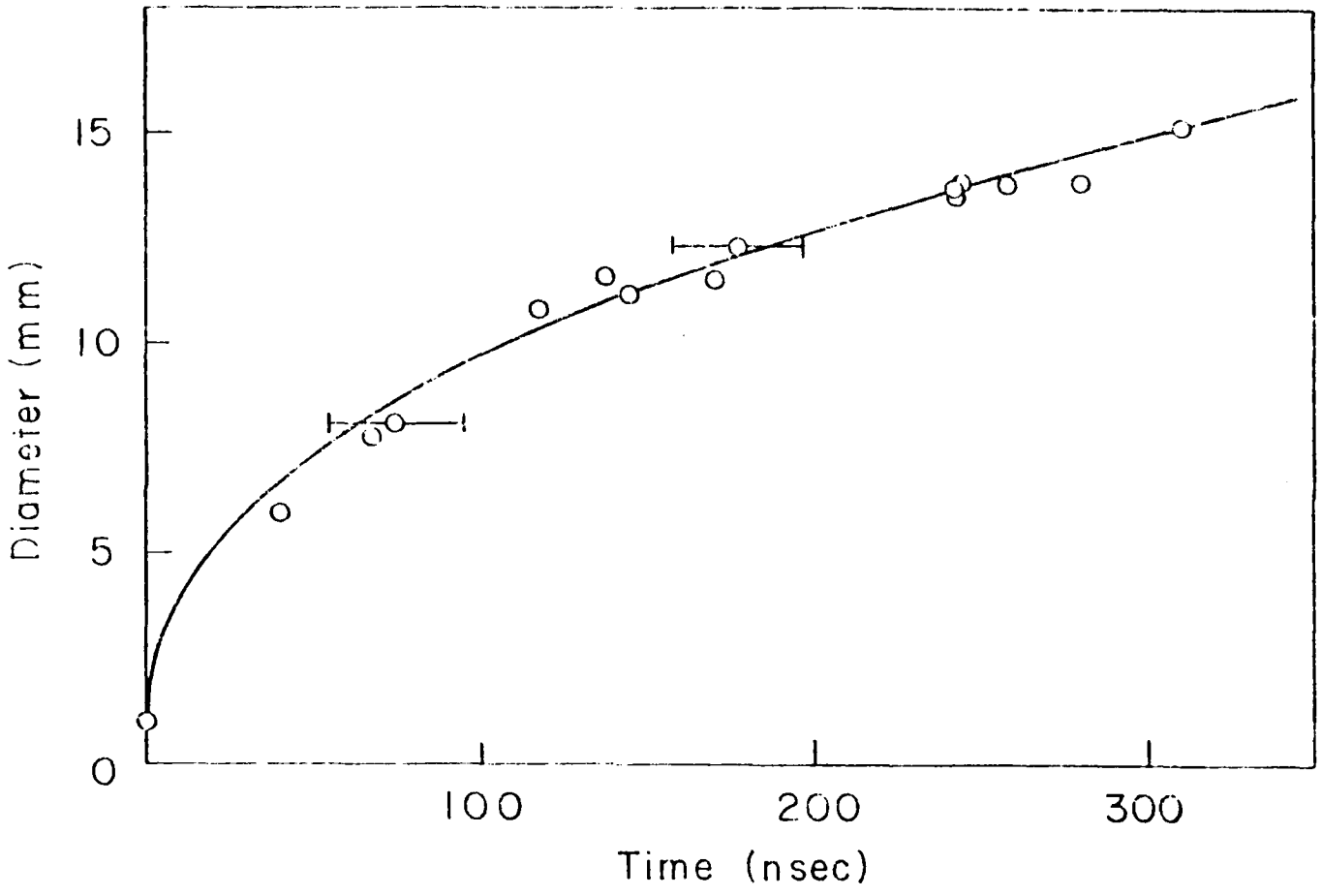

Fig. III-7 Shock front diameter versus time from schlieren pictures. The solid curve is a best fit assuming $d \propto t^{2/5}$.

an unionized gas with $\gamma = 7/5$ the observed expansion would imply that 39 J out of the 300 J laser pulse were deposited in the gas. However, the effects of ionization would require significantly greater deposition.

It is possible to estimate plasma temperatures just behind the shock based on variable γ technique described by Ahlborn[27] and the Rankine-Hugoniot relations for a strong shock. Shock velocities taken from the curve in Fig. (III-7) would imply temperatures of approximately 60 eV at 20 nsec dropping (approximately as v^2) to 2.5 eV at 300 nsec.

It is possible to unfold schlieren photographs to obtain the plasma electron density. This has been done for several of the photographs, although the accuracy of the results is poor. The procedure consists of scanning the photograph on a microphotometer to obtain the photographic density as a function of position. A sample microphotometer trace is shown in Fig (III-8). Using the tabulated characteristics of the film, the density is related to the exposure level, from which the deflection of the rays passing through the plasma can be calculated.

To the extent that the plasmas being studied are axially symmetric, the deflection angles are proportional to the line integral of the transverse density gradient through a cylinder.

$$\varepsilon(y) = \frac{r_o^2}{2} \int_{\text{ray path}} \frac{dn_e}{dy}\, dx \qquad \text{(III-2)}$$

$$= \frac{r_o^2 y}{} \int_y^R \frac{dn_e}{dr} \frac{dr}{\sqrt{r^2 - y^2}}$$

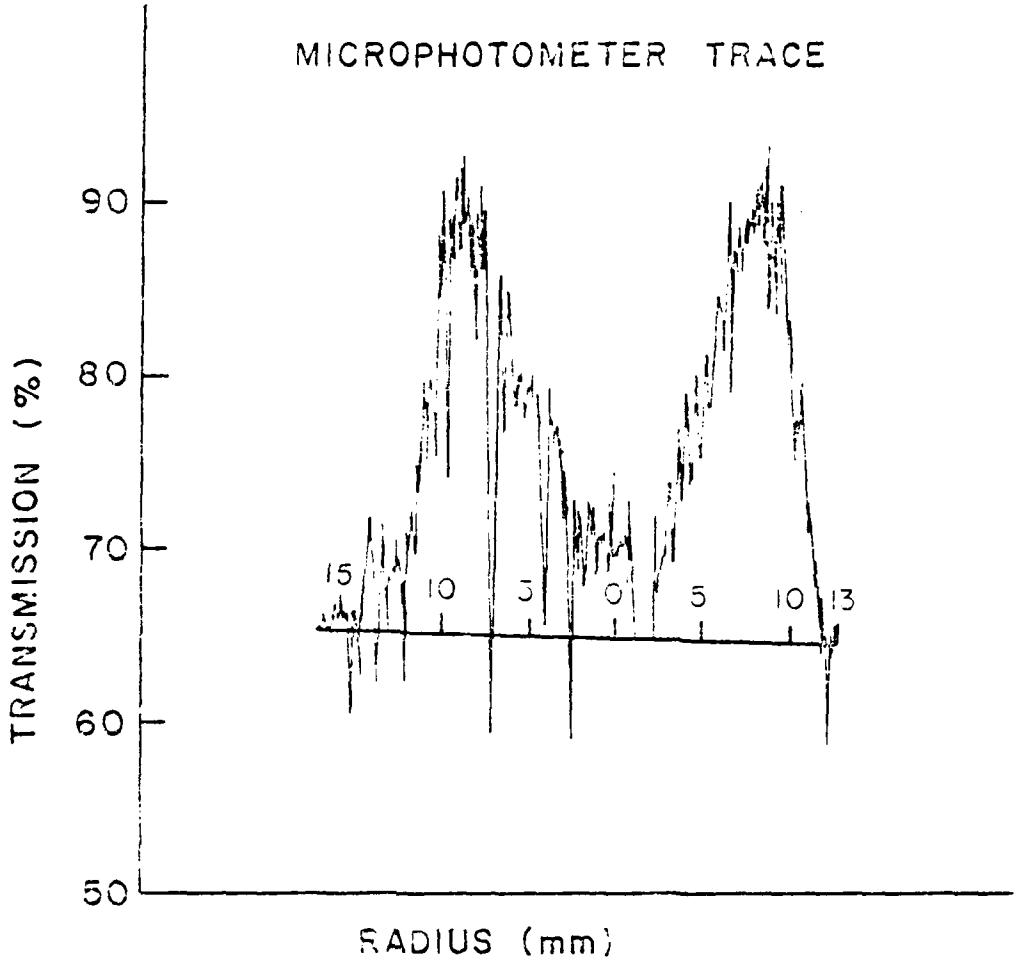

Fig. III-3 Microphotometer scan of a schlieren photographic negative and summary. The curve gives the percent transmission of the negative versus radial position. The solid line is the assumed baseline.

where y is the distance from the center of symmetry in the photograph and x is along the line of sight.

The solution of this integral equation is most easily accomplished by dividing the plasma into a number of concentric rings and assuming a simple functional form for $n_e(r)$ in each ring. The integral can then be performed analytically in each ring yielding a series of linear equations of the form

$$\varepsilon_j = a_{1j}n_1 + a_{2j}n_2 + \ldots + a_{ij}n_i + \ldots \qquad \text{(III-3)}$$

where ε_j and n_i are values of the angle and density at discrete intervals. The a_{ij} can be regarded as a matrix A, whose inverse A^{-1} gives the n_i as linear combinations of the ε_j

$$n_i = a^{-1}_{i1}\varepsilon_1 + a^{-1}_{i2}\varepsilon_2 + \ldots + a^{-1}_{ij}\varepsilon_j + \ldots \qquad \text{(III-4)}$$

Such a matrix and its inverse were generated assuming that $n_e(r)$ is quadratic in r.

Plots of radial density profiles read from photographs taken at three different times after the start of the laser pulse are shown in Fig. (III-9). Fig. (III - 9a) taken during the earliest part of the laser pulse shows densities corresponding to full single ionization of the nitrogen, $n_e = 7.8 \times 10^{17}$ cm^{-3}. In Fig. (III-9b)

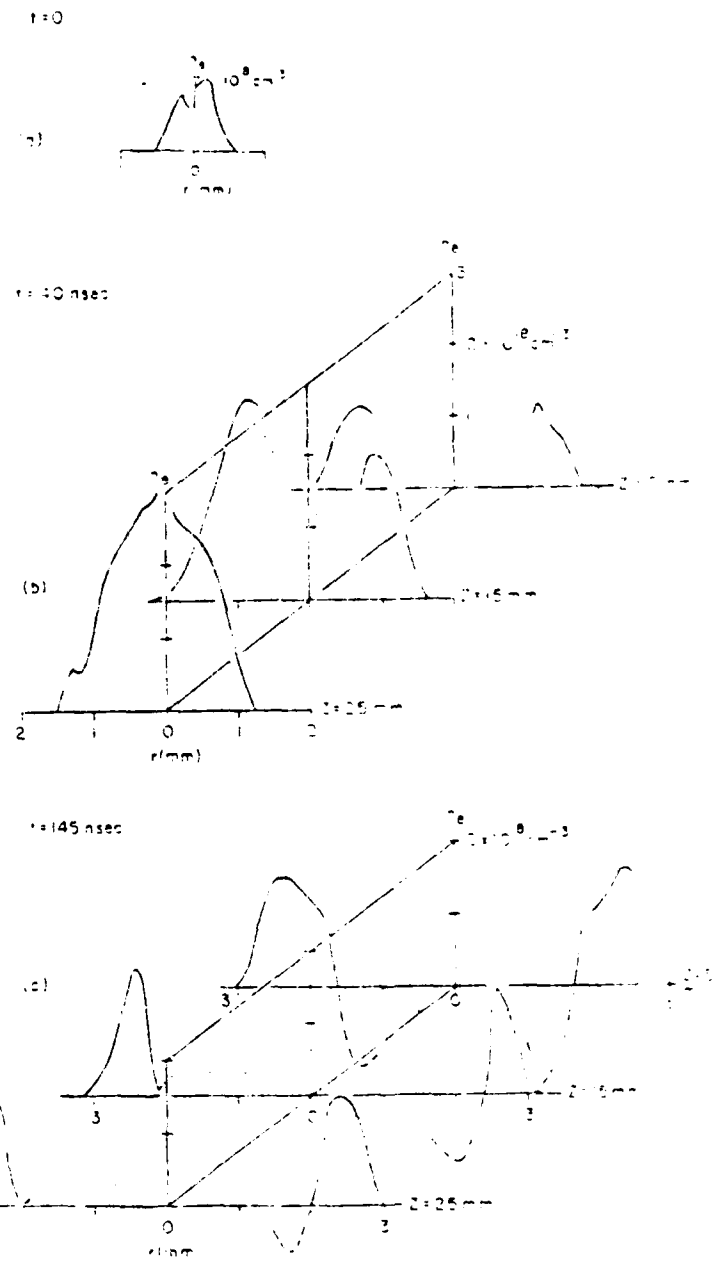

[illegible] radial density profiles from Abel inversions of Schlieren photographs at different times after initial breakdown.

the peak density has climbed shortly after the peak of the laser pulse to three times this value. By 145 nsec in Fig. (III-9c) a radially moving blast wave has become well formed.

In parts b and c of Fig. (III-9) the center of the photographs could not be read accurately because of the plasma luminosity and because the changes in the exposures due to the presence of the plasma were too small to be distinguished from fluctuations in the background exposure. The dotted lines show the density in the center region obtained from assuming that the deflection angles in the center were zero. They should not be taken very seriously. The negative density values, which are clearly non-physical, and the lack of symmetry from one side to the other are due to some combination of two sources of errors: variations in the background exposure due to non-uniform illumination of the field, which could be improved with further refinement of the experimental system; and deviations from cylindrical symmetry in the plasma, which introduces errors in the Abel inversion.

Measurements in unmagnetized nitrogen have shown that during the laser pulse at least some fraction of the plasma becomes triply-ionized. The expansion after the spike of the laser pulse is seen to behave as a spherical blast wave.

D. Summary

In summary, a schlieren photography system capable of providing quantitative, time and space resolved density measurements has been designed, built, and demonstrated. This system is inherently well-suited for the study of shock structures and sharp boundaries frequently seen in laser-produced plasmas, but it is less well-suited for absolute measurements of slowly varying density structures.

Interesting measurements have been made with this system of unmagnetized nitrogen plasmas, but time has not permitted other experiments.

IV. Four-Wave Scattering Diagnostics

A. Introduction.

There is a great deal of interest in plasma diagnostic techniques which measure more or less directly the temperature of the plasma species. In nuclear fusion research both the electron and ion temperatures are of interest, since the former determines much of the dynamical behavior, and the latter determines the reaction rate.

The classic technique for measuring the electron temperature is Thomson scattering of laser radiation. However, Thomson scattered power levels are very small, which has contributed to reducing its usefulness when measuring ion temperatures. Clearly, any technique which could significantly enhance the scattered power would be of great practical importance.

Nonlinear interactions are candidates for such enhancement techniques since they produce scattering proportional to the product of two or more laser powers, which can easily be made very large. This chapter describes a theoretical analysis of one such nonlinear scattering interaction which is cubic in the pump powers, involving four wave interactions. Section IV.B. outlines the kinetic theory of "weak" third order nonlinearities. Section IV.C. discusses the results of the theory relevant to plasma diagnostics, and Section IV.D. discusses their application to plasma experiments in terms of the plasma parameters and available laser sources.

Interactions between three electromagnetic waves in a plasma give rise to, and are mediated by, an electrostatic plasma wave. It is through the dispersion characteristics of this wave that the interaction gains its diagnostic value.

In a simple picture two laser fields beat with each other and drive a coherent plasma wave at their difference frequency. The density fluctuations associated with the plasma wave scatter the third laser field. The scattered radiation is coherently collimated, which is one of the advantages of the technique.

B. Solution of the Vlasov-Maxwell Equations

Kinetic behavior of a collisionless plasma is described by the Vlasov equation. If that equation is Fourier analyzed in space and time it becomes

$$i(\omega_j - \bar{k}_j \cdot \bar{v})\, f_{j\mu}(\bar{v}) + \frac{q_\mu}{m_\mu}(\bar{E}_j + \bar{v} \times \bar{B}_j) \cdot \nabla_{\bar{v}} f_{o\mu}(\bar{v}) + \frac{q_\mu}{m_\mu} \sum_m (\bar{E}_m + \bar{v} \times \bar{B}_m) \cdot \nabla_{\bar{v}} f_{j-m\mu}(\bar{v}) = 0 \qquad \text{(IV-1)}$$

where $f_{o\mu}(\bar{v})$ is the distribution function of the μ'th species in the absence of perturbing fields, $f_{j\mu}(\bar{v})$ is the component of the perturbed distribution at $(\bar{k}_j, \omega_j)$, and $f_{j-m\mu}(\bar{v})$ is its component at $(\bar{k}_j - \bar{k}_m, \omega_j - \omega_m)$.

We look first at the Vlasov equation in which $(\bar{k}_j, \omega_j)$ satisfy

$$\bar{k}_j = \bar{k}_1 - \bar{k}_2 + \bar{k}_3$$

$$= \quad - \qquad \text{(IV-2)}$$

where $(\bar{k}_1, \omega_1)$, $(\bar{k}_2, \omega_2)$ are the wave vectors and frequencies of two electromagnetic waves

$$\tilde{E}_1 = \bar{E}_1 \exp[-i(\bar{k}_1 \cdot \bar{r} - \omega_1 t)] + c.c.; \quad \tilde{B}_1 = \frac{\bar{k}_1 \times \tilde{E}_1}{\omega_1}$$
$$\tilde{E}_2 = \bar{E}_2 \exp[-i(\bar{k}_2 - \bar{r} - \omega_2 t)] + c.c.; \quad \tilde{B}_2 = \frac{\bar{k}_2 \times \tilde{E}_2}{\omega_2} \qquad \text{(IV-3)}$$

where $\tilde{E}_{1,2}$ is a real vector field with twice the amplitude of $\bar{E}_{1,2}$. This equation is

$$i(\omega_5 - \bar{k}_5 \cdot \bar{v}) \; f_{5u} + \frac{q_u}{m_u} \; \bar{E}_5 \cdot \nabla_{\bar{v}} f_{ou}$$
$$+ \frac{q_u}{m_u} \left[\left(\bar{E}_1 + \frac{\bar{v} \times (\bar{k}_1 \times \bar{E}_1)}{\omega_1} \right) \cdot \nabla_{\bar{v}} f_{-2u} + \left(\bar{E}_{-2} + \frac{\bar{v} \times (\bar{k}_2 \times \bar{E}_{-2})}{\omega_2} \right) \right. \qquad \text{(IV-4)}$$
$$\left. \cdot \nabla_{\bar{v}} f_{1u} \right] = 0$$

Here $\bar{E}_{-2}$ and f_{-2u} are the coefficients of the complex conjugates of $\bar{E}_2$ and f_{2u}.

If the nonlinearities are assumed to be weak then f_{1u} and f_{-2u} can be taken to be the familiar solutions to the linearized Vlasov equation

$$f_{1u} = -\frac{q_u}{im_u} \; \frac{\bar{E}_1 \cdot \nabla_{\bar{v}} f_{ou}}{\omega_1 - \bar{k}_1 \cdot \bar{v}}$$
$$\qquad \text{(IV-5)}$$
$$f_{-2u} = \frac{q_u}{im_u} \; \frac{\bar{E}_{-2} \cdot \nabla_{\bar{v}} f_{ou}}{\omega_2 - \bar{k}_2 \cdot \bar{v}}$$

The cross terms in the brackets in Eq. (IV - 4) at first glance seem to make the problem very complicated. However, in most cases of interest these terms reduce to a surprisingly simple form. The simplification will be described in subsection 1.

1. The Ponderomotive Force

The assumptions that must be made to effect the simplification are: (a) the phase velocity of the electromagnetic waves is much greater than the particle thermal velocities, thus terms of order v_T^2/c^2 will be ignored while those of order v_T/c will be kept (v_T is the thermal velocity); (b) the particle distribution is isotropic; and (c) ω_5 is comparable or less than $k_5 v_T$, i.e., the plasma waves interact strongly with thermal particles.

Denoting the term with brackets in (IV-4) by $im_\mu^2 M_\mu/q_\mu^2$, substituting (IV-5), performing the gradients of the denominators, and expanding the gradient of a dot product where advantageous, it is found useful to break M_μ into the five pairs of terms.

$$M_\mu^1 = \frac{\bar{E}_1 \cdot \nabla_{\bar{v}}(\bar{E}_{-2} \cdot \nabla_{\bar{v}} f_{o\mu})}{\omega_2 - \bar{k}_2 \cdot \bar{v}} - \frac{\bar{E}_{-2} \cdot \nabla_{\bar{v}} (\bar{E}_1 \cdot \nabla_{\bar{v}} f_{o\mu})}{\omega_1 - \bar{k}_1 \cdot \bar{v}} \qquad \text{(IV-6)}$$

$$M_\mu^2 = \frac{\bar{E}_1 \cdot \bar{k}_2 \, \bar{E}_{-2} \cdot \nabla_{\bar{v}} f_{o\mu}}{(\omega_2 - \bar{k}_2 \cdot \bar{v})^2} - \frac{\bar{v} \times (\bar{k}_2 \times \bar{E}_{-2}) \cdot (\bar{E}_1 \cdot \nabla_{\bar{v}}) \nabla_{\bar{v}} f_{o\mu}}{\omega_2 (\omega_1 - \bar{k}_1 \cdot \bar{v})} \qquad \text{(IV-}$$

$$M_{-}^{3} = \frac{-\bar{E}_{-2} \cdot \bar{k}_1 E_1 \cdot \nabla_{\bar{v}} f_{o\mu}}{(\omega_1 - \bar{k}_1 \cdot \bar{v})^2} + \frac{\bar{v} \times (\bar{k}_1 \times \bar{E}_1) \cdot (\bar{E}_{-2} \cdot \nabla_{\bar{v}}) \nabla_{\bar{v}} f_{o\mu}}{\omega_1 (\omega_2 - \bar{k}_2 \cdot \bar{v})} \qquad \text{(IV-8)}$$

$$M_{-}^{4} = \frac{\bar{v} \times (\bar{k}_1 \times \bar{E}_1) \cdot (\bar{E}_{-2} \times (\nabla_{\bar{v}} \times \nabla_{\bar{v}} f_{o\mu}))}{\omega_1 (\omega_2 - \bar{k} \cdot \bar{v})} \qquad \text{(IV-9)}$$

$$- \frac{\bar{v} \times (\bar{k}_2 \times \bar{E}_{-2}) \cdot (\bar{E}_1 \times (\nabla_{\bar{v}} \times \nabla_{\bar{v}} f_{o\mu}))}{\omega_2 (\omega_1 - \bar{k}_1 \cdot \bar{v})}$$

$$M_{-}^{5} = \frac{\bar{v} \times (\bar{k}_1 \times \bar{E}_1) \cdot \bar{k}_2 (\bar{E}_{-2} \cdot \nabla_{\bar{v}} f_{o\mu})}{\omega_1 (\omega_2 - \bar{k}_2 \cdot \bar{v})^2} \qquad \text{(IV-10)}$$

$$- \frac{\bar{v} \times (\bar{k}_2 \times \bar{E}_{-2}) \cdot k_1 (\bar{E}_1 \cdot \nabla_{\bar{v}} f_{o\mu})}{\omega_2 (\omega_1 - \bar{k}_1 \cdot \bar{v})^2}$$

The term M_{-}^{4} vanishes because the curl of a gradient is taken. Term M_{-}^{5} is of order

$$M_{-}^{5} \approx O\left(\frac{k_L^2}{\omega_L^3}\right) = O\left(\frac{1}{\omega_L u^2}\right)$$

where ω_L and k_L are typical of the imposed electromagnetic fields and u is their phase velocity in plasma

$$u = \frac{c}{\sqrt{1 - \omega_p^2/\omega_L^2}} \cdot c$$

We ignore terms of this order by assumption (a).

Term M_{μ}^{1} can be rewritten

$$M_{\mu}^{1} = \left(\frac{1}{\omega_2 - \bar{k}_2 \cdot \bar{v}} - \frac{1}{\omega_1 - \bar{k}_1 \cdot \bar{v}} \right) \frac{\nabla_{\bar{v}}}{2} \cdot \left[\bar{E}_1 (\bar{E}_{-2} \cdot \nabla_{\bar{v}} f_{ou}) + \bar{E}_{-2} (\bar{E} \cdot \nabla_{\bar{v}} f_{ou}) \right] = \frac{\omega_5 - \bar{k}_5 \cdot \bar{v}}{(\omega_1 - \bar{k}_1 \cdot \bar{v})(\omega_2 - \bar{k}_2 \cdot \bar{v})}$$

$$\times \frac{\nabla_{\bar{v}}}{2} \cdot \left[\bar{E}_1 (\bar{E}_{-2} \cdot \nabla_{\bar{v}} f_{ou}) + E_{-2} (E_1 \cdot \nabla_{\bar{v}} f_{ou}) \right] \qquad \text{(IV-11)}$$

When this term is substituted into IV-4, the velocity dependence outside the divergence cancels (since $\bar{k}_L \cdot \bar{v} \ll \omega_L$) and the remaining divergence in velocity space prevents it from contributing to any charge or current density. Thus M_{μ}^{1} can be ignored.

The two remaining terms are of the same form so that we need study only one for the time being. Using, from assumption (b),

$$(\bar{E} \cdot \nabla_{\bar{v}}) \nabla_{\bar{v}} f_{ou} = 2\bar{E}_1 \frac{\partial f}{\partial v^2} + 2\bar{v} (\bar{E}_1 \cdot \nabla_{\bar{v}}) \frac{\partial f}{\partial v^2}$$

The part proportional to $\bar{v}$ vanishes when dotted into the cross product, leaving

$$M_{\mu}^{2} = \frac{\bar{E}_1 \cdot \bar{k}_2 \, \bar{E}_{-2} \cdot \nabla_{\bar{v}} f_{ou}}{(\omega_2 - \bar{k}_2 \cdot \bar{v})^2} - \frac{\bar{E}_1 \cdot \bar{k}_2 \, \bar{E}_{-2} \cdot \nabla_{\bar{v}} f_{ou}}{\omega_2 (\omega_1 - \bar{k}_1 \cdot \bar{v})} + \frac{E_1 \cdot E_{-2} \, \bar{k}_2 \cdot \nabla_{\bar{v}} f_{ou}}{\omega_2 (\omega_1 - \bar{k}_1 \cdot \bar{v})} \qquad \text{(IV-12)}$$

The difference between the first two terms is of order $k_L(\omega_1-\omega_2)/\omega_L^3 v_T$. But this is of order $k_L^2/\omega_L^3 = 1/u^2\omega_L$ by assumption (c), which can be ignored by assumption (a). Thus the only terms remaining are

$$M_- \cong M_-^2 + M_-^3$$

$$\cong \frac{\bar{E}_1 \cdot \bar{E}_2\, \bar{k}_2 \cdot \nabla_v f_{0e}}{\omega_2(\omega_1 - \bar{k}_1 \cdot \bar{v})} - \frac{\bar{E}_1 \cdot \bar{E}_2\, \bar{k}_1 \cdot \nabla_v f_{0e}}{\omega_1(\omega_2 - \bar{k}_2 \cdot \bar{v})} \qquad \text{(IV-13)}$$

$$\cong -\frac{\bar{E}_1 \cdot \bar{E}_{-2}}{\omega_1\omega_2}\, \bar{k}_5 \cdot \nabla_v f_{0e}$$

where again $\bar{k}_L \cdot \bar{v} \ll \omega_L$. This term gives rise to the well-known ponderomotive force, and assumptions (a), (b) and (c) are completely sufficient to make it the only term to order v_T/c.

2. Plasma Fluctuation Distribution

Equation (IV-4) can now be readily solved

$$f_{5e}(\bar{v}) = \frac{iq_-}{m_-}\left(\bar{E}_5 + \frac{iq_-}{m_-}\frac{\bar{E}_1\cdot\bar{E}_{-2}}{\omega_1\omega_2}\,\bar{k}_5\right) \cdot \frac{\nabla_v f_{0e}}{\omega_5 - \bar{k}_5\cdot\bar{v}} \qquad \text{(IV-14)}$$

If $\bar{E}_5$ is assumed to be longitudinal (transverse solutions do not couple to the ponderomotive force and are therefore uninteresting) the charge density is

$$\rho_5 = \sum_- q_- \int f_{5-}(\bar{v})\, d\bar{v}$$

$$= \frac{iq_i^2}{m_i}\int d\bar{v}\, \frac{\bar{E}_5 \cdot \nabla_v f_{0i}}{\omega_5 - \bar{k}_5\cdot\bar{v}} + \frac{ie^2}{m_e}\int d\bar{v}\, \frac{\bar{E}_5 \cdot \nabla_v f_{0e}}{\omega_5 - \bar{k}_5\cdot\bar{v}} \qquad \text{(IV-15)}$$

$$+ \frac{e^2}{m_e^2}\frac{\bar{E}_1\cdot\bar{E}_{-2}}{\omega_1\omega_2}\int d\bar{v}\, \frac{\bar{k}_5\cdot\nabla_v f_{0e}}{\omega_5 - \bar{k}\cdot\bar{v}}$$

The effect of the ponderomotive force on the ions has been ignored because it is smaller than for electrons by m_e/m_i. The integrals in (IV-15) are proportioned to the ion and electron plasma susceptibilities described, for instance, by Fried and Conte[1].

$$\rho_5 = i\varepsilon_o (\chi_{5i} + \chi_{5e}) \bar{k}_5 \cdot \bar{E}_5 + \frac{\varepsilon_o e k_5}{m_e} \frac{\bar{E}_1 \cdot \bar{E}_{-2}}{\omega_1 \omega_2} \chi_{5e} \qquad \text{(IV-16)}$$

The solution to the Fourier analyzed Maxwell equations for a longitudinal electric field in a conducting medium is

$$\bar{E}_5 = \frac{i\bar{k}_j \rho_j}{\varepsilon_o k_j^2} \qquad \text{(IV-17)}$$

Thus

$$\bar{E}_5 = \frac{i\chi_{5e}}{1 + \chi_{5e} + \chi_{5i}} \frac{e \bar{E}_1 \cdot \bar{E}_{-2}}{m_e \omega_1 \omega_2} \frac{\bar{k}_5}{k_5} \qquad \text{(IV-18)}$$

Inserting this result in (IV-14) gives

$$f_{5e} = -\frac{e^2/m_e^2}{\omega_5 - \bar{k}_5 \cdot \bar{v}} \frac{1 + \chi_{5i}}{1 + \chi_{5i} + \chi_{5e}} \frac{\bar{E}_1 \cdot \bar{E}_{-2}}{\omega_1 \omega_2} \bar{k}_5 \cdot \nabla_v f_{oe} \qquad \text{(IV-19)}$$

This is essentially a result found by Drake, et. al.[2], who introduced the ponderomotive force in a more ad hoc manner.

3. The Scattered Field

The electromagnetic field scattered by these plasma fluctua-

tions when a field

$$\bar{E}_3 = \bar{E}_3 \exp[-i(\bar{k}_3 \cdot \bar{r} - \omega_3 t)] + \text{c.c.}, \quad B_3 = \frac{\bar{k}_3 \times \bar{E}_3}{\omega_3} \qquad \text{(IV-3.5)}$$

is present in the plasma is found by solving the Vlasov-Maxwell equations at

$$\begin{aligned} \bar{k}_4 &= \bar{k}_3 \pm (\bar{k}_1 - \bar{k}_2) \\ \omega_4 &= \omega_3 \pm (\omega_1 - \omega_2) \end{aligned} \qquad \text{(IV-20)}$$

since mixing terms appear under these conditions.

$$\begin{aligned} i(\omega_4 - \bar{k}_4 \cdot \bar{v}) f_{4e} - \frac{e}{m_e} \bar{E}_4 \cdot \nabla_v f_{oe} - \frac{e}{m_e} \bar{E}_3 \cdot \nabla_v f_{5e} &= 0 \\ i(\omega_4 - \bar{k}_4 \cdot \bar{v}) f_{4i} + \frac{q_i}{m_i} \bar{E}_4 \cdot \nabla_v f_{oi} &= 0 \end{aligned} \qquad \text{(IV-21)}$$

The ion mixing terms are again small enough to be neglected. For a transverse field the Fourier transformed Maxwell equations are solved by

$$\bar{E}_i = \frac{i \mu_o \bar{k}_j \times (\bar{k}_j \times \bar{J}_j)}{k_j^2 (k_j^2 - \omega_j^2/c^2)} \qquad \text{(IV-22)}$$

Substituting (IV-19) into (IV-21), and using the solution to find $\bar{J}_4$, the field $\bar{E}_4$ is found to be, in Fourier space,

$$\bar{E}_4 = \frac{e^2/m_e^2}{k_4^2 c^2 - \omega_4^2 + \omega_p^2} \frac{(1 + \chi_{5i}) \chi_{5e}}{1 + \chi_{5i} + \chi_{5e}} k_5^2 \frac{\bar{E}_1 \cdot \bar{E}_2}{\omega_1 \omega_2} \frac{\bar{k}_4 \times (\bar{k}_4 \times \bar{E}_3)}{k_4^2} \qquad \text{(IV-23)}$$

In transforming this field to time and space variables use is made of the faltung theorem, which states that the transform of the product of two functions in Fourier variables is a convolution in time and space variables

$$\left(\frac{1}{2\pi}\right)^2 \int F(\bar{k}, \omega)\, G(\bar{k},\omega)\, e^{-i(\bar{k}\cdot\bar{r} - \omega t)}\, d\bar{k}\, d\omega = \left(\frac{1}{2\pi}\right)^2 \int f(\bar{r}', t')\, g(\bar{r} - \bar{r}', t - t')\, d\bar{r}'\, dt' \tag{IV-24}$$

where f and g are the transforms of F and G.

The field $\bar{E}_4$ is just such a product of the two functions

$$G(\bar{k}_4,\omega_4) = \frac{\bar{k}_4 \times \bar{k}_4 \times}{k_4^2 c^2 + \omega_p^2 - \omega_4^2} \tag{IV-25}$$

$$F(\bar{k}_4,\omega_4) = \frac{e^2}{m_e^2} \frac{(1 + \chi_{5i})\,\chi_{5e}}{1 + \chi_{5i} + \chi_{5e}} \frac{k_5^2}{k_4^2} \frac{\bar{E}_1 \cdot \bar{E}_{-2}}{\omega_1 \omega_2} \bar{E}_3 \tag{IV-26}$$

The transforms of G and F are

$$g(\bar{r},t) = \frac{1}{u^2} \frac{\bar{r}}{r} \times \frac{\bar{r}}{r} \times \frac{\delta(t - r/u)}{r} \tag{IV-27}$$

$$f(\bar{r},t) = \frac{e^2}{m_e^2} \frac{(1 + \chi_{5i})\,\chi_{5e}}{1 + \chi_{5i} + \chi_{5e}} \frac{k_5^2}{k_4^2} \frac{\bar{E}_1 \cdot \bar{E}_{-2}}{\omega_1 \omega_2} \times \bar{E}_3\, e^{-i(\bar{k}_4\cdot\bar{r} - \omega_4 t)} \tag{IV-28}$$

The transform of F results from the presence of an implied delta function in $(\bar{k}_4, \omega_4)$ which forces satisfaction of the matching conditions. To make that delta function explicit it could have been carried as factor of $\bar{E}_{-2}$, for instance. It was omitted here only for simplicity.

$\bar{E}_4$ can now be calculated where the convolution in (IV-24) is taken over the volume in the plasma of the intersection of three beams, and the observation point is taken outside of the plasma, $\bar{r} >> \bar{r}'$.

$$\bar{E}_4(\bar{r},t) = \frac{1}{c^2} \frac{e^2}{m_e^2} \frac{k_5^2}{k_4^2} \frac{(1+\chi_{5i})\,\chi_{5e}}{1+\chi_{5i}+\chi_{5e}} \frac{\bar{E}_1 \cdot \bar{E}_{-2}}{\omega_1 \omega_2} \frac{a^3 j_1\left(|\bar{k}_4 - \frac{\omega_4}{c}\hat{r}|\right)}{|\bar{k}_4 - \frac{\omega_4}{c}\hat{r}|} \times \nabla_{\bar{r}} \times \left(\nabla_{\bar{r}} \times \frac{\bar{E}_3\, e^{-i(\bar{k}_4 \cdot \bar{r} - \omega_4 t)}}{R} \right) \qquad \text{(IV-29)}$$

where a is the radius of the scattering volume, assumed spherical, j_1 is the spherical Bessel function of the first kind, $\hat{r}$ is the unit vector in the observation direction, and $R = |\bar{r}|$, the distance from the center of the plasma to the observation point.

The spherical Bessel function is strongly peaked about $\hat{r} \cdot \bar{k}_4$, such that 95% of the power is scattered into the angle corresponding to the first zero of j_1,

$$\theta = \frac{3.99(\text{rad})}{k_4 a} = 32°(\lambda_4/a) \qquad \text{(IV-30)}$$

The Poynting vector is calculated from $\bar{E}_4$ keeping in mind that by definitions (IV-3) the $\bar{E}_j$ are only half the amplitude of E_j, and that there is an equal contribution to E_4 at its complex conjugate. Integrating the Poynting vector over the angle Ω gives the scattered power

$$P_4 = \frac{2r_0^2 \omega_p^4 P_1 P_2 P_3}{a^2 \omega_1^2 \omega_2^2 \omega_4^2 (k_B T_e)^2} \left| \frac{(1 + \chi_{5i}) \chi_{5e} / \epsilon^2}{1 + \chi_{5i} + \chi_{5e}} \right|^2 \left| \hat{\epsilon}_1 \cdot \hat{\epsilon}_2 \right|^2 \left| \hat{k}_4 \times \hat{\epsilon}_3 \right|^2 \qquad \text{(IV-31)}$$

where r_o is the classical electron radius $r_o = e^2/(4\pi\varepsilon_o m_e c^2)$, ω_p is the plasma frequency, T_e is the electron temperature, a is the scattering parameter $a = (k_5 \lambda_D)^{-1}$, λ_D the plasma Debye length, and the $\hat{\epsilon}_i$ and $\hat{k}_4$ are unit vectors in the polarization directions of the fields and the observation direction, respectively.

This result should be valid under the assumptions enumerated earlier, and as long as the incident fields are small enough to allow (IV-5) to be used. Other authors[28] have shown that this requires

$$v_i = \frac{eE_i}{m_e \tilde{\omega}_i} \ll v_T \qquad \text{(IV-32)}$$

that is, the quiver velocity should be much less than the thermal velocity.

C. Diagnostic Possibilities for Four Wave Scattering

For the scattered power (IV-31) to be of value as a diagnostic tool it must contain information about the plasma state. This information

is contained in the factor containing the plasma susceptibilities, which we shall denote by the function S

$$S(k_5, \omega_5) = \left| \frac{(1 + \chi_{5i}) \chi_{5e}}{1 + \chi_{5i} + \chi_{5e}} \right|^2 \qquad \text{(IV-33)}$$

where the susceptibilities are

$$\chi_{j\mu} \equiv \frac{q_\mu^2}{\epsilon_o m_\mu} \frac{1}{k_j^2} \int \frac{d\bar{v}\ \bar{k}_j \cdot \bar{\nabla}_{\bar{v}} f_{o\mu}}{\omega_j - \bar{k}_j \cdot \bar{v}} \qquad \text{(IV-34)}$$

For a Maxwellian distribution function χ_μ is found to be

$$\chi_\mu = -\alpha_\mu^2 \sqrt{\pi}\, i\, x_\mu\, e^{-x_\mu^2} + \alpha_m^2 \left(1 - 2x_\mu\, e^{-x_\mu^2} \int_o^{x_\mu} e^{t^2}\, dt \right) \qquad \text{(IV-35)}$$

$$x_\mu = \frac{\omega}{k v_{T\mu}} \quad , \quad v_{T\mu} = \sqrt{\frac{2k_B T_\mu}{m_\mu}} \qquad \text{(IV-36)}$$

This expression applies to any species μ so long as α_μ is evaluated using the Debye length of the species. However, by convention α usually represents the electron scattering parameter, so that α_i can be replaced by

$$\alpha_i = \sqrt{\frac{ZT_e}{T_i}}\ \alpha \qquad \text{(IV-37)}$$

For a plasma of electrons and one ion species S depends on the two variables x_e and x_i, both of which are proportional to ω_5/k_5. Because of the mass dependence of these variables, x_i will become large

for relatively small values of ω_5 compared to x_e. Since for x_i large, χ_{5i} goes to zero, the ion dynamics will have an effect on only the part of the spectrum, $S(\omega_5)$, for ω_5 relatively small. Electron dynamics alone will determine the spectrum for larger ω_5. The division of the spectrum into these two parts makes it possible to distinguish electron and ion contributions. For more than one ion species the larger mass ions will contribute at smaller ω_5.

In Fig. (IV-1) S is plotted versus x_i for $\alpha = 10$ and various values of T_e/T_i for a Maxwellian plasma. For $\alpha \gg 1$ the ion spectrum is nearly independent of α, whereas for $\alpha \ll 1$ ion contributions are swamped by electron contributions. It is clear that if the ion spectrum could, with confidence, be measured with considerable accuracy with α large, it would provide both T_i and the ratio of T_e/T_i.

Also in Fig. (IV - 1) an ion spectrum due to Thomson scattering has been plotted normalized at $x_i = 0$. It shows that there is considerable similarity between the two types of spectra, although in general the four-wave spectrum has larger values for $x_i \gtrsim 1$.

The electron contribution to the spectrum S is plotted versus x_e in Fig. (IV - 2). This part does not depend on T_e/T_i (except for the appearance of the ion-acoustic resonance when $T_e \gg T_i$) but varies considerably with α. The structure at small x_e is due to the ions and is included for comparison. Like the ion part, the electron spectra have many similarities to Thomson scattered spectra although they are

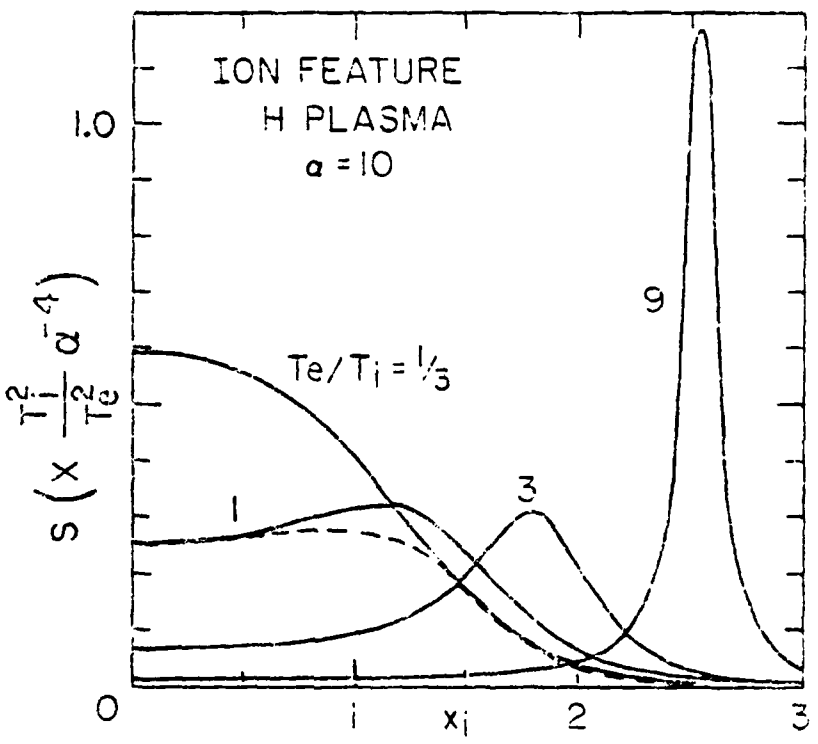

Fig. IV-1 Spectral function for four-wave scattering versus $x_i = \omega_s/(k_s v_{ti})$ for hydrogen with $\alpha = 10$ and various values of T_e/T_i. The dashed line is a Thomson scattering spectrum for $\alpha = 10$ and $T_e/T_i = 1$ normalized to $x_i = 0$.

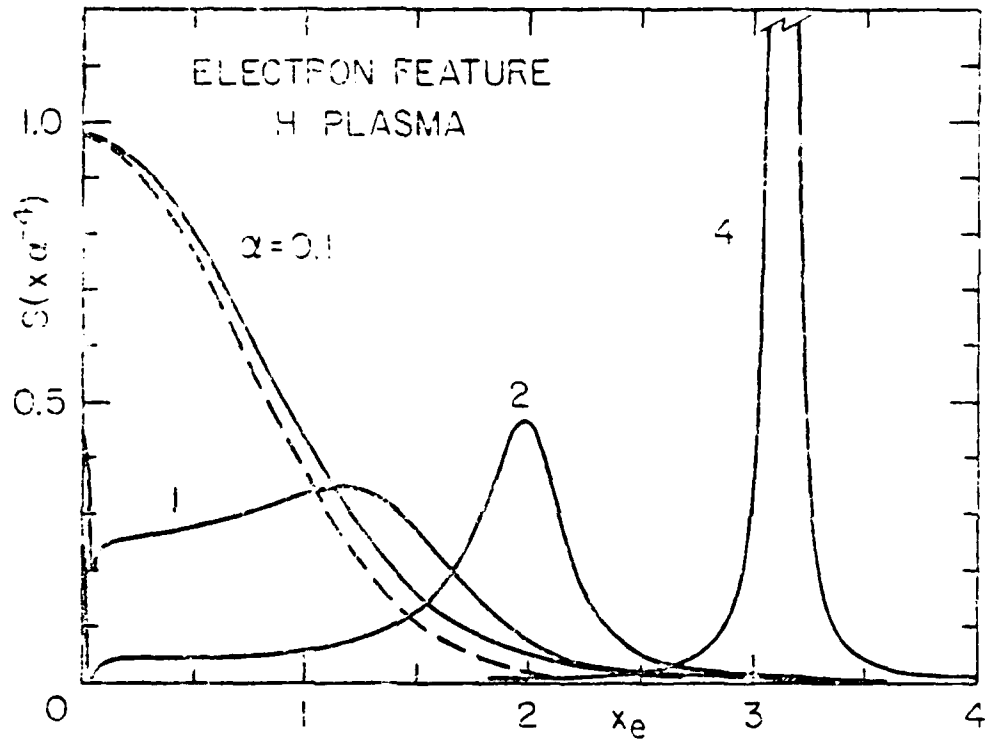

Fig. IV-2 Spectral function for $x_e = \frac{1}{2}(x^2 - y^2)$ for angle $\theta = \pi/2$ for various values of α. The dashed curve is a Thomson scattering spectrum for $\alpha = 1$. The intermediate peak at $x_e = 1$ is due to the ion part of the spectrum.

not identical.

This analysis of the spectral function S shows that four wave scattering has the ability to provide diagnostic access to both the electron and ion temperatures. Additionally, it might provide information about the presence of different ion species and, if the spectrum could be fit to a specific value of α, even the particle density.

D. Applying Four Wave Scattering to Experiments

In order to apply four-wave scattering to a plasma physics experiment, a number of choices have to be made regarding the characteristics of the sources used and the experimental configuration. Indeed, it needs to be determined under what conditions four-wave scattering can give an appreciable advantage over Thomson scattering. Plasma physics experiments span some thirteen or fourteen orders of magnitude in particle density and four orders of magnitude in temperature. Thus much of the discussion in this section will be directed towards identifying experimentally significant issues and exploring their parametric dependences.

The choices of source wavelength, power, bandwidth, and the experimental configuration are, of course, all strongly coupled. For several reasons, however, the choice of wavelength plays a central role. Thus this section will be divided into several subsections dealing with: (1) choice of wavelength; (2) source bandwidth; (3) comparison with Thomson scattering; (4) scattered power; and (5) possible

experimental configurations.

1. Source Wavelength

The power due to four wave scattering (IV-31) is proportional to the product

$$P_4 \propto \frac{1}{\omega_1^2 \omega_2^2 \omega_4^2}$$

where ω_1 and ω_2 are the frequencies of two of the imposed fields and ω_4 that of the scattered field. Depending on the plasma parameters and the choice of experimental configuration, the relative values of ω_1, ω_2 and ω_4 can vary considerably. For many experiments of interest, however, and for purposes of estimation it is useful to assume

$$\omega_1 \sim \omega_2 \sim \omega_4 \sim \omega_L = 2\pi c/\lambda_L$$

where ω_L and λ_L are the source frequency and wavelength. Thus $P_4 \propto \lambda_L^6$.

This wavelength dependence strongly favors use of the longest wavelength sources possible. However, wavelengths longer than the critical wavelength

$$\lambda_c = \frac{2\pi c}{e}\sqrt{\frac{\varepsilon_o m_e}{n_e}}$$

cannot propagate in plasma, and wavelengths near this value are subject to strong absorption and refraction. An upper limit that we have thus chosen for estimates is $\lambda_L = \lambda_c/10$. Taking this upper limit for λ_L, Fig. (IV-3) shows the wavelengths appropriate to various plasma densities, with examples of experiments and sources included .

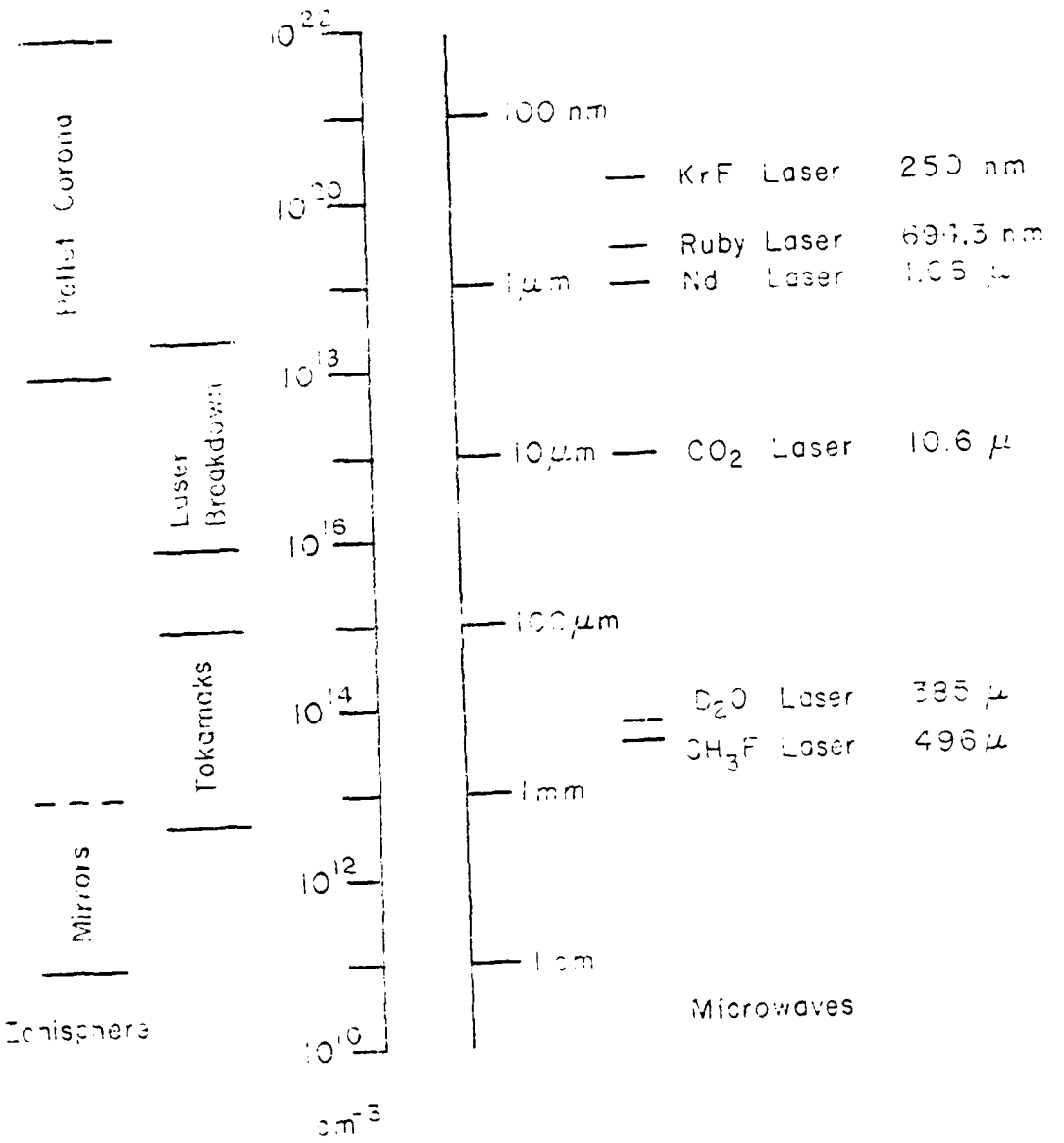
Pellet Corona
Laser Breakdown
Tokamaks
Mirrors
Ionisphere
10^{22}
10^{20}
10^{18}
10^{16}
10^{14}
10^{12}
10^{10}
cm^{-3}
100 nm
1 μm
10 μm
100 μm
1 mm
1 cm
KrF Laser 250 nm
Ruby Laser 694.3 nm
Nd Laser 1.06 μ
CO_2 Laser 10.6 μ
D_2O Laser 385 μ
CH_3F Laser 496 μ
Microwaves

This choice $\lambda_L = \lambda_c/10$ is appropriate for another reason when the ion spectrum is being studied. As was shown in Section C, it is necessary to have $\alpha \gtrsim 10$ in this case. Taking $|\bar{k}_1 - \bar{k}_2| = 2k_L \sin(\theta_{12}/2)$ where θ_{12} is the angle between $\bar{k}_1$ and $\bar{k}_2$ this requirement on α implies

$$\frac{1}{2k_L \lambda_D \sin(\theta_{12}/2)} \gtrsim 10 \qquad \text{(IV-38)}$$

which, using $\lambda_D = \sqrt{\epsilon_o k_B T_e / n_e e^2}$, reduces to

$$\sin\left(\frac{\theta_{12}}{2}\right) \lesssim \frac{1}{20} \frac{\lambda_L}{\lambda_c} \sqrt{\frac{k_B T_e}{\epsilon}} \qquad \text{(IV-39)}$$

Thus the maximum scattering angle θ_{12}^{max} that can be used for a given temperature depends on the ratio λ_L/λ_c.

For T_e = 100eV and $\lambda_L = \lambda_c/10$ the maximum angle is $\theta_{12}^{max} = 42°$, and raising T_e to 1 keV lowers θ_{12}^{max} to 13°. These angles are not unreasonable experimentally, but clearly the choice of λ_L significantly smaller than $\lambda_c/10$ would lead to experimentally unacceptably small angles. Thus in the case of ion scattering we must use long wavelength sources both to maximize the scattered power and to allow a reasonable scattering angle.

The choice of wavelength has the additional effect of imposing a lower bound on a, the focal radius of the imposed fields and hence the radius of the scattering volume. Diffraction sets the limit

$$a \gtrsim 1.22 f \lambda_L. \qquad \text{(IV-40)}$$

where f is the focussing f number. Whether this limit is approached

depends on the particular source, and f will be constrained by the experiment. It is significant to note, however, that if $\underline{a}$ is set equal to this lower limit and ℓ_L is assumed to be $\ell_c/10$, the scattered power, P_4, becomes independent of density!

$$P_4 = 3.4 \times 10^{-6} \quad \frac{r_o^2 P_1 P_2 P_3}{c^2 f^2 (k_B T_e)^2} \quad \frac{S(k_5, \omega_5)}{A^4} \quad \left| E_1 \cdot E_2 \right|^2 \left| k_4 \times E_3 \right|^2 \quad \text{(Watts)} \qquad \text{(IV-41)}$$

2. Source bandwidth

Four wave scattering and Thomson scattering differ in the sense that the scattered field in Thomson scattering inherently has a finite spectral width characteristic of the plasma parameters if the bandwidth of the source is narrow. On the other hand, four-wave scattering because it obeys the frequency matching condition (IV-20) produces an output beam whose spectral width is determined solely by the spectral widths of the input beams. If it is desired to obtain a complete spectrum on one shot with four-wave scattering, one of the input sources should have a spectral width comparable to the width of the function $S(\bar{k}_5, \omega_5)$, while the other source or sources should have a much narrower width.

As discussed in Section C, the width of the ion part of $S(\bar{k}_5, \omega_5)$ is much less than that of the electron part. In both cases the (one-sided) spectrum is contained within

$$\Delta\omega \approx 2.5$$

unless the ion-acoustic or electron-plasma resonance is strong. Thus to obtain a full (two-sided) spectrum one of the sources should have the bandwidth

$$\Delta f_L = \frac{2.5}{\tau} k_5 v_{Tu} = 10 f_L \frac{v_{Tu}}{c} \sin\left(\theta_{12}/2\right) \qquad \text{(IV-42)}$$

where v_{Tu} is the electron or ion thermal velocity. Thus the ratio $\Delta f_L/f_L = \Delta\lambda_L/\lambda_L$ depends only on the particle velocity and the scattering angle.

For hydrogen at T_i = 100eV for the ion spectrum this ratio is $\Delta f_L/f_L = 3.3 \times 10^{-3} \sin(\theta_{12}/2)$, and for T_i = 1 keV $\Delta f_L/f_L = 1.0 \times 10^{-2} \sin(\theta_{12}/2)$. These bandwidths are reasonable to expect from some laser sources, and the much narrower width needed from the other source or sources is also achievable. For the electron spectra the widths become very large so that few laser sources could provide them.

3. Comparison with Thomson Scattering

We've seen in Section C that the spectral functions of four-wave scattering and Thomson scattering, while not identical, do not differ greatly in interesting parameter ranges, i.e., $x \ll 1$ for the ion spectrum and $x \gg 1$ for the electron spectrum. In these ranges, the spectra have their maximum or nearly maximum values at the center, $x = 0$. Thus we will compare the scattered powers by taking their ratios at this point.

The power available from Thomson scattering[29] per unit frequency is

$$\frac{dP_T}{df} = r_o^2 n_e \ell d\Omega P_i S_T(\bar{k},\omega) \left| \hat{k}_4 \times \hat{\varepsilon}_i \right|^2 \qquad \text{(IV-43)}$$

where n_e is the electron density, ℓ is the length of the scattering volume, $d\Omega$ is the collection solid angle, P_i is the source power, and $S_T(\bar{k}, \omega)$ is the Thomson scattering spectral function. At $\omega = 0$, $S_T(\bar{k}, \omega)$ assumes the values

$$S_T(\bar{k},o) = \begin{cases} \dfrac{2\pi Z}{k v_{Ti}} \dfrac{\alpha^4}{|\varepsilon(o)|^2} & \alpha \gg 1 \\ \dfrac{2\pi}{k v_{Te}} & \alpha \ll 1 \end{cases} \qquad \text{(IV-44)}$$

where $\varepsilon(o)$ is the value at $\omega = 0$ of $1 + \chi_i(k, \omega) + \chi_e(k, \omega)$.

The spectral function from four-wave scattering, $S(\bar{k}_5, \omega_5)/4\pi$ assumes the values at $\omega_5 = 0$

$$S(k,10) = \begin{cases} \left(\dfrac{ZT_e}{T_i}\right)^2 \dfrac{\alpha^4}{|\varepsilon(o)|^2} & \alpha \gg 1 \\ 1 & \alpha \ll 1 \end{cases} \qquad \text{(IV-45)}$$

If it is assumed that the four-wave scattering power is distributed over the bandwidth Δf_L given by (IV-42), then the ratio of four-wave to Thomson scattering powers assuming $P_i = P_3$ is

$$\frac{P_4/\Delta f_L}{dP_T/df} = \frac{N_e a^2 \lambda_4^2}{5.6\, \ell\, d\Omega} \left| \frac{\bar{v}_1}{v_{Te}} \cdot \frac{\bar{v}_2}{v_{Te}} \right|^2 \left[Z \frac{T_e^2}{T_i^2} \right] \qquad \text{(IV-46)}$$

for $\alpha >> 1$. The factor in brackets is omitted for $\alpha << 1$. Here again, $\bar{v}_i = e\bar{E}_i/m_e\omega_i$ is the electron quiver velocity. This way of writing the ratio emphasizes the role of the ratio v_i/v_{Te} which should be small to avoid strong nonlinearities. The coefficient of the velocity factor can easily be very large so that four-wave scattering exceeds Thomson scattering for a broad range of input powers.

Figure (IV-4) is a plot of the lines

$$\frac{P_4/\Delta f_L}{dP_T/df} = 1$$

in the space of plasma density and input power (assuming $P_1 = P_2 = P_3 = P_i$) for two plasma temperatures in hydrogen. The dashed curves are the lines $v_i/v_{th} = 1$ showing the upper limit on source powers imposed by strong nonlinear effects. The wavelengths are chosen to be $\lambda_L = \lambda_c/10$ as discussed in subsection 1. For lower densities the focal radius is taken as $a = 1.22f\lambda_L$ with a conservative choice of f=30. For higher densities and shorter wavelengths $\underline{a}$ is arbitrarily set to $\underline{a}$ = 1 mm. The factor $d\Omega$ from Thomson scattering is limited by spectral distortion and imaging effects. For our estimates it is taken to be 10^{-2} cm·sr.

Figure (IV-4) illustrates dramatically the advantage that can be gained from four-wave scattering, particularly when it is noted that

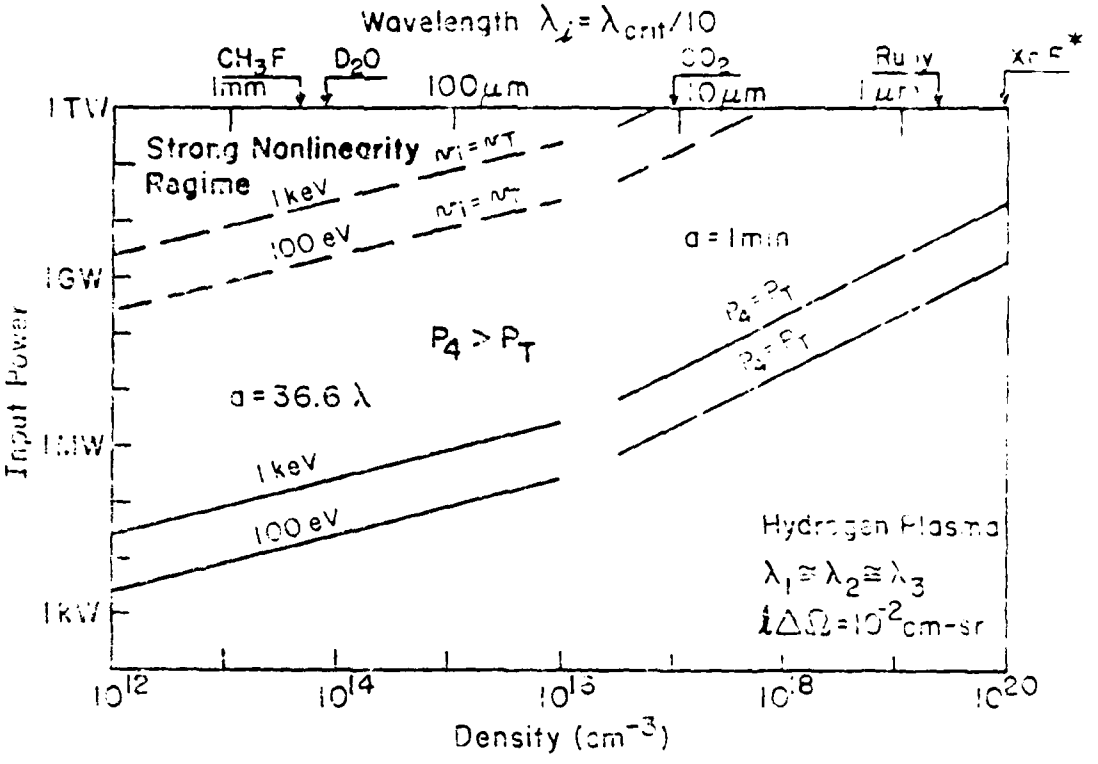

Fig. IV-4 The input power for which four-wave stimulated Raman scattering are equal. The break in the curve is where [illegible] assumption for a Debye radius. The dashed lines are the powers at which other non-linear effects become important.

above the solid lines enhancements increase as the square of the input power. A wide range of sources are available which can provide sufficient power ranging from, for instance, commonly used ruby and Nd-glass lasers, to CO_2 lasers in the infrared, to optically pumped submillimeter lasers such as D_2O and CH_3F, to conventional microwave sources. Thus plasmas over a very broad range of density are accessible to this diagnostic. In the case of Tokamak plasmas, for instance, Thomson scattering from the ions requires power levels above the solid line in Fig. (IV-4) just to overcome background, so that anytime Thomson scattering can be performed at the wavelength given, four wave scattering would be advantageous.

4. Scattered Power

The power scattered due to four-wave interactions, eq.(IV-31), is plotted in Fig. (IV - 5) for the same assumptions as were used in Fig. (IV - 4). The input wavelengths are all taken as $\lambda_c/10$, the focal radius is $a = 1.22f\lambda_L$ for f = 30 below 10^{16} electrons/cm^3 and a = 1 mm above; a hydrogen plasma is assumed; and all the input sources are assumed to have the same power, 1 MW for the solid lines and 1 GW for the dashed lines.

Below 10^{16} cm^{-3} the assumptions lead to the scattered power being independent of density (Eq. (IV-41)) in marked contrast to Thomson scattering. The scattered power is smaller for higher electron temperature plasmas due to its T^{-2} dependence.

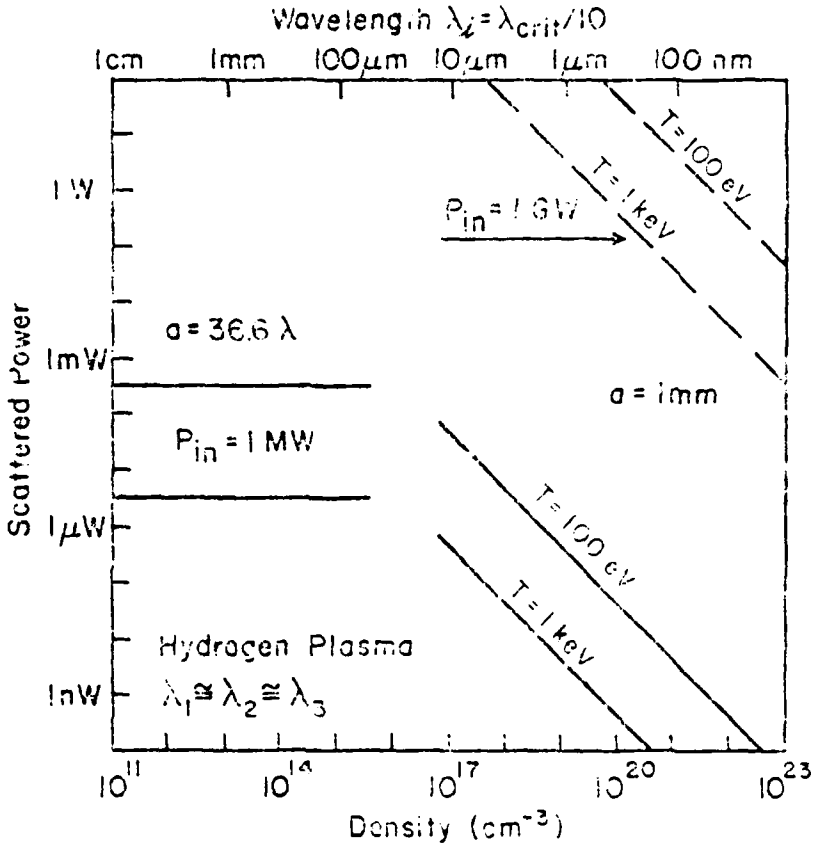

Fig. II-5 Power [illegible] for [illegible] input power is 1 MW for the solid lines and 1 GW for the dashed lines.

5. Possible Experimental Configurations

So far in the discussion the only restrictions that have been placed on the experimental use of four-wave scattering have been on the general frequency range and bandwidth of the sources, the angle between $\bar{k}_1$ and $\bar{k}_2$, and the matching conditions for the scattered wave eq. (IV-20):

$$\bar{k}_4 = \bar{k}_3 \pm (\bar{k}_1 - \bar{k}_2)$$
$$\omega_4 = \omega_3 \pm (\omega_1 - \omega_2)$$

In addition the electric fields $\bar{E}_1$ and E_2 should not be polarized perpendicular to each other so that $|\hat{\epsilon}_1 \cdot \hat{\epsilon}_2|^2$ does not vanish. The lack of further restrictions on the scattering geometry, beam polarizations, and even the number of beams needed allows a flexibility that can provide several advantages over other techniques. To illustrate this point several possible experimental configurations will be described.

If only two beams are imposed on a plasma the formalism of this chapter is all completely valid upon the substitutions $\bar{k}_3 = \bar{k}_1$ and $\omega_3 = \omega_1$. The matching conditions Eq. (IV-20) for anti-Stokes scattering then become

$$\bar{k}_4 = 2\bar{k}_1 - \bar{k}_2 \qquad \text{(IV-47)}$$
$$\omega_4 = 2\omega_1 - \omega_2$$

This type of scattering is called "CARS" for coherent anti-Stokes Raman spectroscopy, a term coined by the atomic and molecular spectroscopists. This configuration is illustrated schematically

in Fig. (IV-6). The polarizations of $\tilde{E}_1$ and $\tilde{E}_2$ would ideally be made parallel to each other and perpendicular to $\bar{k}_4$.

The Stokes component of such a two beam interaction has matching conditions

$$\bar{k}_4 = \bar{k}_1 - (\bar{k}_1 - \bar{k}_2) = \bar{k}_2$$
$$\omega_4 = \omega_1 - (\omega_1 - \omega_2) = \omega_2 \qquad \text{(IV-48)}$$

This scattered field emerges along one of the beam directions. It could be detected if, for instance, $\tilde{E}_1$ were circularly polarized and $\tilde{E}_2$ were plane polarized. A polarizer downstream of $\tilde{E}_2$ could block $\tilde{E}_2$ and allow a component of $\tilde{E}_4$ (which would also be circularly polarized) to pass to the detector. Because this effectively rotates the polarization of part of $\tilde{E}_2$ this interaction has been termed RIKES for Raman-induced Kerr effect spectroscopy. It is illustrated in Fig. (IV-7).

A third class of experiments could be performed using three separate beams with frequency ω_3 being significantly different from ω_1 or ω_2. This could help alleviate stray light problems. These are illustrated in Fig. (IV-8).

One distinct advantage of all four-wave scattering techniques is that the scattered field is localized in a well-collimated beam. This allows the collection f/number to equal the focussing f/number of the input beams, allowing good rejection of any plasma radiation or stray light. This is in distinct contrast to the situation in Thomson scattering where the collection angle should be maximized.

CARS

(Coherent Anti Stokes Raman Spectroscopy)

$$\bar{k}_4 = \bar{k}_1 + (\bar{k}_1 - \bar{k}_2)$$

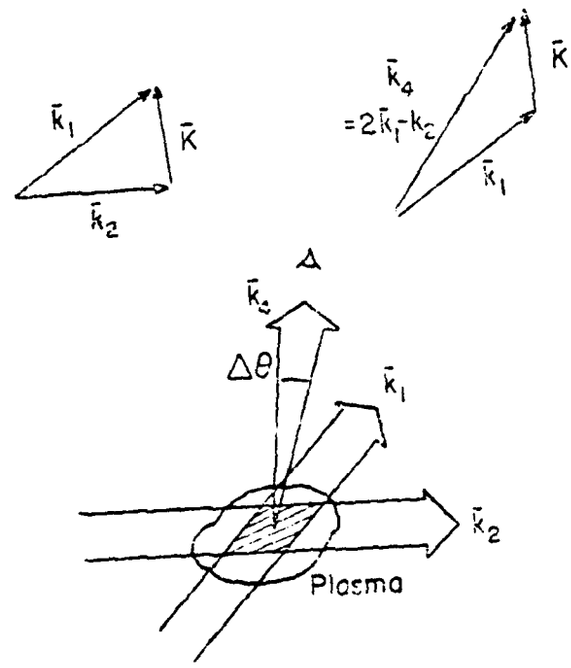

Fig. V-5 Schematic of CARS (Coherent Anti-Stokes Raman spectroscopy) experiment.

RIKES

(Raman Induced Kerr Effect Spectroscopy)

$$\bar{k}_4 = \bar{k}_1 - (\bar{k}_1 - \bar{k}_2)$$

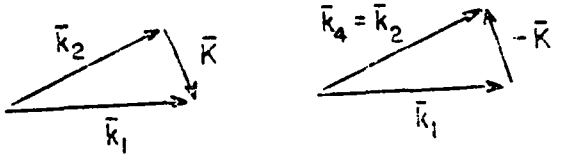

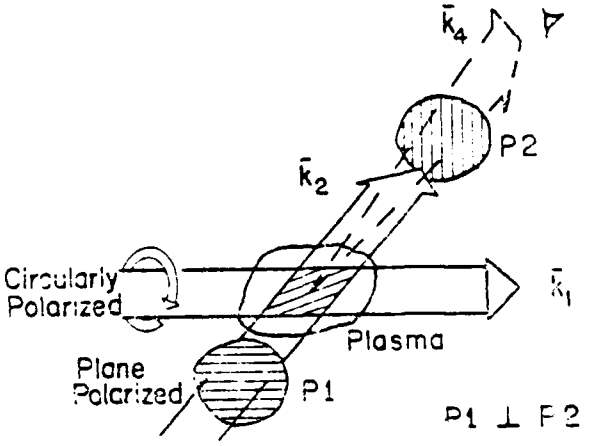

Fig. IV-7 Schematic of a RIKES (Raman-induced Kerr effect spectroscopy) experiment.

Three Beam Scatering

$$\bar{k}_4 = \bar{k}_3 \pm (\bar{k}_1 - \bar{k}_2)$$

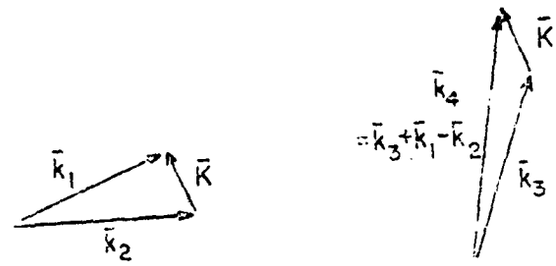

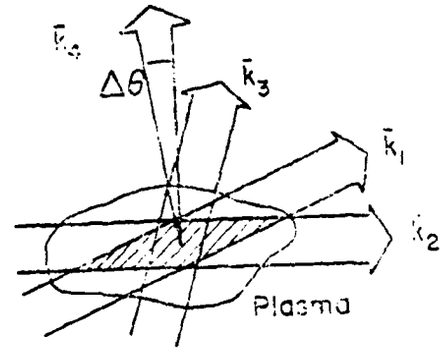

Fig. IV-6 Schematic of a three beam experiment.

In all of these configurations fields E_1 and E_2 could even be allowed to be broadband with Δf_L as given the subsection 2, even derived from the same source. By monitoring the spectral shapes of the input sources, the spectral shape of the spectral function could be unfolded.

REFERENCES

1. B.D. Fried and S.D. Conte, The Plasma Dispersion Function, (Academic Press, New York, 1961).

2. J.F. Drake, P.K. Kaw, Y.C. Lee, G. Schmidt, C.S. Liu and M.N. Rosebluth, Phys. Fluids 17, 778 (1974).

3. C.S. Liu, M.N. Rosenbluth, and R.B. White, Phys. Fluids 17, 1211-1219 (1974).

4. M.N. Rosenbluth, R.B. White and C.S. Liu, Phys. Rev. Lett. 31, 1190 (1973).

5. C. Karmendy, W. Halverson and B. Lax, J. Mag. and Mag. Mat. 11, 379-382 (1979).

6. A.A. Offenberger, M.R. Cervenan, and P.R. Smy, J. Appl. Phys. 47, 494-497 (1976).

7. A. Yariv, Quantum Electronics, 1st ed., (John Wiley & Sons, Inc., New York, 1967), p.323.

8. D.W. Forslund, J.M. Kindel, and E.L. Lindeman, Phys. Fluids 18, 1017-1030 (1975).

9. N.G. Loter, Soft X-Ray Diagnostics for Magnetically Combined CO_2 Laser-Heated Plasma, Ph.D. Thesis, Massachusetts Institute of Technology, Cambridge, Massachusetts (1979).

10. H.J. Kunze, A.H. Gabriel and H.E. Griem, Phys. Rev. 165, 267 (1968).

11. G.W.F. Drake and A. Dalgarno, Astrophys. J. 15, 459 (1967).

12. H.J. Kunze, A.H. Gabriel and H.R. Griem, Phys. Fluids 11, 662 (1968).

13. O. Bely, Phys. Lett. 26A, 408 (1968).

14. A.H. Gabriel and C. Jordan, "Spectral Intensities from Plasmas," in Case Studies in Atomic Collision Physics II, E.W. McDaniel and M.R.C. McDowell, eds., (New York: North Holland, 1972).

15. R.C. Elton, "Atomic Processes," in Methods of Experimental Physics: Plasma Physics, Part A, H.R. Griem and R.H. Lovberg, eds., (Academic Press, New York, 1970), p. 115.

16. R.C. Elton and W.W. Köppendörfer, Phys. Rev. 160, 194 (1967).

17. D.R. Bates and A. Dalgarno, "Electronic Recombination," in Atomic and Molecular Processes, D.R. Bates, ed., (Academic Press, New York, 1962).

18. H. VanRegemorter, Astrophys. J. 136, 906 (1962).

19. P. Bogen, "X-ray Diagnostics of Plasmas," in Plasma Diagnostics, W. Lochte-Holtgreven, ed., (Elsevier (North Holland), New York: 1968), p. 424.

20. A.H. Gabriel and T.M. Paget, J. Phys.B 5, 673 (1972).

21. A. Pospieszcyk, Astron. and Astrophys. 39, 357 (1975).

22. C.P. Bhalla, A.H. Gabriel and L.P. Presnyakov, Monthly Not. Roy. Ast. Soc. 172, 359 (1975).

23. R.F. Benjamin, P.B. Lyons and R.H. Day, Appl. Opt. 16, 393 (1977).

24. R.D. Bleach and D.J. Nagel, J. Appl. Phys. 49, 3832 (1978).

25. F.C. Jahoda and R.E. Siemon, Holographic Interferometry Cookbook, Los Alamos Report, LA-5058-MS, (1972).

26. D.L. Jones, Phys. Fluids 5, 637 (1962).

27. B. Ahlborn, Can. J. Phys. 53, 976 (1975).

28. V.B. Krapchev, Phys. Rev. Lett 42, 497 (1979).

29. J. Sheffield, Plasma Scattering of Electromagnetic Radiation, Academic Press, New York, 1975), p. 130.

Appendix A

LIST OF PUBLICATIONS

1. W. Halverson, "Bremsstrahlung Photon Emission Rate from Maxwellian Plasmas," Plasma Physics 14, 601 (1972).

2. D.R. Cohn, C.E. Chase, W. Halverson, and B. Lax, "Magnetic-Field-Dependent Breakdown of CO_2-Laser-Produced Plasma," Appl. Phys. Lett. 20, 225 (1972).

3. Daniel R. Cohn and Benjamin Lax, "Magnetic-Field-Enhanced Heating of Plasmas with CO_2 Lasers," Appl. Phys. Lett. 21, 217 (1972).

4. D.R. Cohn, W. Halverson, B. Lax, and C.E. Chase, "Effect of Magnetic Field on Electron Density Growth during Laser-Induced Gas Breakdown," Phys. Rev. Lett. 29, 1544 (1972).

5. M.P. Hacker, D.R. Cohn, and B. Lax, "Low-Pressure Gas Breakdown with CO_2 Laser Radiation," Appl. Phys. Lett. 23, 392 (1973).

6. Benjamin Lax, A.H. Guenther, D.R. Cohn, and W. Halverson, "Feasibility of X-Ray Lasers," Laser Interaction and Related Plasma Phenomena, Vol. 3, edited by H.J. Schwarz and H. Hora, (Plenum, New York, 1973).

7. N.G. Loter, G.J. Raff, D.R. Cohn, and W. Halverson, "Effect of Magenetic Field upon Plasmas Produced by Laser-Induced Gas Breakdown," Appl. Phys. Lett. 45, 97 (1974).

8. M.P. Hacker, D.R. Cohn, and R.L. Brooks, "Effect of Inelastic Energy Loss on CO_2 Laser Breakdown of Gases," Appl. Phys. Lett. 24, 173 (1974).

9. W. Halverson, "CO_2-Laser-Driven Detonation Waves in the Presence of a Strong Magnetic Field," Appl. Phys. Lett. 24, 364 (1974).

10. Benjamin Lax, Daniel Cohn, and Ward Halverson, "Laser Interaction with Plasmas in High Magnetic Fields," Physique sous Champs Magnetiques Intenses, Colloques Internationaux C.N.R.S., No. 242, (1974).

11. D.R. Cohn, G.J. Raff, R.L. Brooks, N.G. Loter, and W. Halverson, "Beam Self-Focusing in a Laser-Produced Plasma in a Magnetic Field," Phys. Lett. 49A, 95 (1974).

12. W. Halverson, "Quasistatic Calculation of Radial Plasma Velocity in Laser-Heated Solenoid," J. Appl. Phys. 45, 5209 (1974).

13. Benjamin Lax and Daniel R. Cohn, "Laser Interaction with Plasmas in Magnetic Fields," Principles of Laser Plasmas, ed. by George Bekefi (John Wiley and Sons, New York, 1975), Chapter 12.

14. G.C. Vlases, H. Rutkowski, A. Hertzberg, A. Hoffman, L. Steinhauer, J. Dawson, D.R. Cohn, W. Halverson, B. Lax, J.D. Daugherty, J.E. Eninger, E.R. Pugh, T.K. Chu, L.C. Johnson, and R.V. Lovelace, "Progress on CO_2 Laser Gas Fusion," Plasma Physics and Controlled Nuclear Fusion Research 1974, Vol. III (International Atomic Energy Agency, Vienna, 1975).

15. D.R. Cohn, M.P. Hacker, B. Lax, and W. Halverson, "Effects of Pressure and Magnetic Field upon Physical Processes in Laser-Induced Gas Breakdown," J. Appl. Phys. 46, 668 (1975).

16. S.Y. Yuen and B. Lax, "Laser Heating of Magnetically Confined Plasma," Phys. Fluids 18, 829 (1975).

17. N.G. Loter, D.R. Cohn, W. Halverson, and B. Lax, "Beam Self-Trapping and Dynamics of Laser-Induced Magnetoplasmas," J. Appl. Phys. 46, 3302 (1975).

18. M.P. Hacker and W. Halverson, "Method for Accurate Determination of Threshold Energies for Laser-Induced Gas Breakdown," Rev. Sci. Instrum. 47, 634 (1976).

19. Ward Halverson, "Head-on Collisions between Radiation-Driven Ionization Fronts," Phys. Fluids 19, 1342 (1976).

20. J.P. Yangos and W. Halverson, "Head-on Collisions between Radiation-Driven Fronts with Self-Consistent Absorption," Phys. Lett. 60A, 37 (1977).

21. W. Halverson and C.V. Karmendy, "X-Ray Measurements of Electron Temperatures in CO_2-Laser Heated Magnetoplasmas," J. Appl. Phys. 48, 99 (1977).

22. B. Lax and S.Y. Yuen, "Effect of Radial Expansion of the Laser Heating of a Magnetically Confined Plasma," J. Appl. Phys. 48, 581 (1977).

23. S.Y. Yuen, "Gaussian Beam Stabilization in a Long Absorptive Plasma Column," Appl. Phys. Lett. 30, 223 (1977).

24. W. Halverson, N.G. Loter, W.W. Ma, R.W. Morrison, and C.V. Karmendy, "CO_2 Laser Irradiation of Solid Targets in Strong Magnetic Fields," Appl. Phys. Lett. 32, 10 (1978).

25. C. Karmendy, W. Halverson, and B. Lax, "Brillouin Scattering from CO_2 Laser Plasmas in Strong Transverse Magnetic Fields," J. Mag. and Mag. Mat. 11, 379 (1979).

26. N.G. Loter, W. Halverson, B. Lax, and D.J. Nagel, "Soft X-Ray Diagnostics of CO_2 Laser-Produced Magnetoplasmas," J. Mag. and Mag. Mat. 11, 376 (1979).

27. H.C. Praddande, D.W. Scudder, and B. Lax, "Coherent Four-Wave Scattering in Plasmas--Application to Plasma Diagnostics," Appl. Phys. Lett. 35, 766 (1979).

APPENDIX B

List of Papers Presented at Meetings

D.R. Cohn, C.E. Chase, W. Halverson, and B. Lax, "Magnetic Field Dependence of Breakdown Threshold Pressure in CO_2 Laser-Produced Plasmas," General Meeting of APS (December 1971).

W. Halverson, D.R. Cohn, C.E. Chase, and S.M. Wolfe, "Observation of Heating of CO_2 Laser Breakdown Plasmas in a Magnetic Field," General Meeting of APS (December 1971).

W. Halverson, D.R. Cohn, C.E. Chase, and B. Lax, "CO_2 Laser Produced Plasmas in a Magnetic Field," VII Internat. Q. Electron. Conf. (June 1972).

D.R. Cohn, W. Halverson, B. Lax, and C.E. Chase, "Time of Laser-Induced Gas Breakdown Effects in a Magnetic Field, "APS - Plasma Phys. Div. Meeting, Monterey (November 1972).

W. Halverson, C.E. Chase, D.R. Cohn. G.J. Raff, and S. Wolfe, "Heating of CO_2 Laser-Produced Plasmas in Magnetized Field," APS Plasma Phys. Div. Meeting, Monterey (November 1972).

B. Lax, D.R. Cohn, and W. Halverson, "Theory of CO_2 Laser-Heating of Plasmas in High Magnetic Fields," APS Plasma Phys. Div. Meeting, Monterey (November 1972).

W. Halverson, "Image-Converter Camera Study of CO_2 Laser-Induced Plasmas in a Magnetic Field," APS Plasma Phys. Div. Meeting, Philadelphia (October 1973).

G.F. Raff, N.G. Loter, D.R. Cohn, and W. Halverson, "Magnetic Field Effect on Temperature and Density of CO_2 Laser Produced Plasmas," APS Plasma Phys. Div. Meeting, Philadelphia (October 1973).

D.R. Cohn, M.P. Hacker, and B. Lax, "Pressure and Magnetic Field Dependence of Threshold Power for CO_2 Laser Induced Gas Breakdown," APS Plasma Phys. Div Meeting, Philadelphia (October 1973).

D.R. Cohn, W. Halverson, G.J. Raff, B. Lax, and S.Y. Yuen, "CO_2 Laser-Induced Plasmas in a Magnetic Field," VIII Internat. Q. Electron. Conf., San Francisco (June 1974).

G.C. Vlases, H. Rutkowski, A. Hertzberg, A. Hoffman, L. Steinhauer, J. Dawson, D.R. Cohn, W. Halverson, B. Lax, J.D. Daugherty, J.E. Eninger, E.R. Pugh, T.K. Chu, L.C. Johnson, and R.V. Lovelace, "Progress on CO_2 Laser Gas Fusion," IAEA 8th Internat. Conf. on Plasma Phys. and Cont. Nuc. Fusion Res., Tokyo (July 1974).

B. Lax, S.Y. Yuen, and D.R. Cohn, "Ion Heating in a Laser Irradiated Plasma Column," APS Plasma Phys. Div. Meeting, Albuquerque (October 1974).

W. Halverson, D.R. Cohn, N.G. Loter, and B. Lax, "Beam Self-Focusing and Heating in Laser-Induced Plasmas with $\beta \leq 1$," APS Plasma Phys. Div. Meeting, Albuquerque (October 1974).

J.D. Daugherty, J.E. Eninger, D.R. Cohn, and W. Halverson, "Scaling of Laser Heated Plasmas Confined in Long Solenoids," APS Plasma Phys. Div. Meeting, Albuquerque (October 1974).

W. Halverson, D.R. Cohn, and B. Lax, "Laser-Plasma Interacions in Intense Magnetic Fields," 7th European Conf. on Cont. Fusion and Plasma Phys., Lausanne, Switzerland (1975).

W. Halverson, "Head-on Collisions Between Radiation-Driven Ionization Fronts," 6th Anamolous Absorption Conf., Vancouver, Canada (May 1976).

W. Halverson, "Head-on Collisions Between Laser-Driven Shock Waves," APS Plasma Phys. Div. Meeting, St. Petersburg, Florida (November 1975).

N.G. Loter, D.R. Cohn, W. Halverson, and B. Lax, "Dynamics of CO_2 Laser-Induced Magnetoplasmas," APS Plasma Phys. Div. Meeting, St. Petersburg, Florida (November 1975).

B. Lax. S.Y. Yuen, and W. Halverson, "Effect of Radial Expansion on the Laser Heating of a Magnetically Confined Plasma," APS Plasma Phys. Div. Meeting, St. Petersburg, Florida (November 1975).

F.R. Chang, D.R. Cohn, H.E. Eninger, W. Halverson, and D.J. Rose, "Stress, Dissipation, and Neutronics Constraints on Magnets for Laser-Solenoid Reactors," APS Plasma Phys. Div. Meeting, St. Petersburg, Florida, (November 1975).

W. Halverson, C.V. Karmendy, and N.G. Loter, "X-ray Measurements of Electron Temperatures in CO_2 Laser Heated Magnetoplasmas," APS Plasma Phys. Div. Meeting, San Francisco (1976).

W.W. Ma, N.G. Loter, and W. Halverson, "Suppression of Upstream Ionization Fronts in CO_2 Laser-Heated Plasmas," APS Plasma Phys. Div. Meeting, San Francisco, (1976).

W. Halverson, N.G. Loter, W.W. Ma, and R.W. Morrison, "CO_2 Laser Irradiation of Solid Targets in High Magnetic Fields," IEEE Internat. Conf. Plasma Sci., New York (1977).

W. Halverson, N.G. Loter, W.W. Ma, R.W. Morrison, C.V. Karmendy, and J.H. Watts, "CO_2 Laser Irradiation of Solid Targets in High Magnetic Fields," 7th Anamolous Absorption Conf., Ann Arbor, Michigan (May 1977).

W. Halverson, N.G. Loter, W.W. Ma, C.V. Karmendy, J.H. Watts, and R.W. Morrison, "CO_2 Laser Irradiation of Solid Targets in High Magnetic Fields," CPA Congress, Saskatoon, Canada (1977).

J.P. Yangos, B. Lax, W. Halverson, and C.V. Karmendy, "Brillouin Backscattering from Gaseous Plasmas in a Transverse Magnetic Field," APS Plasma Phys. Div. Meeting, Atlanta (1977).

W. Halverson, N.G. Loter, W.W. Ma, C.V. Karmendy, and J.H. Watts, "CO_2 Laser Irradiation of Solid Targets in High Magnetic Fields," APS Plasma Phys. Div. Meeting, Atlanta (1977).

N.G. Loter, W. Halverson, and C.V. Karmendy, "Soft X-ray Diagnostics of CO_2-Laser-Heated Megneto-Plasma," APS Topical Conf. on High Temp. Plasma Diagnostics, Santa Fe (1978).

C. Karmendy, W. Halverson, and B. Lax, "Brillouin Scattering from CO_2 Laser Plasmas in Strong Transverse Magnetic Fields," 1st Internat. Conf. on Solids and Plasmas in High Mag. Fields, Cambridge, (1978).

N.G. Loter, W. Halverson, B. Lax, D.J. Nagel, "Soft X-ray Diagnostics of CO_2 Laser-Produced Magnetoplasmas," 1st Internat. Conf. on Solids and Plasmas in High Mag. Fields, Cambridge (1978).

C. Karmendy, W. Halverson, and B. Lax, "Transverse Magnetic Field Dependence of Stimulated Brillouin Scattering from Laser Plasmas," APS Plasma Phys. Div. Meeting, Colorado Springs (1978).

N.G. Loter, W. Halverson, and B. Lax, "Soft X-ray Diagnostics of CO_2 Laser Magnetoplasmas," Conf. on Atomic Processes in High Temp. Plasmas, Boulder (Jan., 1979).

N.G. Loter, W. Halverson, and B. Lax, "Soft X-Ray Diagnostics for Magnetically Confined CO_2 Laser-Heated Plasmas," IEEE Internat. Conf. on Plasma Sci., Montreal (June 1979).

C. Karmendy and B. Lax, "Stimulated Brillouin Scattering from CO_2 Laser Plasmas in Strong Transverse Magnetic Fields," IEEE Internat. Conf. on Plasma Sci., Montreal (1979).

D.W. Scudder, H.C. Praddaude, and B. Lax, "Coherent Four-Wave Scattering for Plasma Temperature Diagnostics," APS Plasma Phys. Div. Meeting, Boston (November 1979).

Appendix C

LIST OF THESES

1. Mark P. Hacker, "Diagnostic Techniques for Laser Produced Plasmas," S.B. Thesis, Dept. of Physics, MIT (1972).

2. N. Loter, "Spectroscopically Determined Temperatures in a Magnetically Confined CO_2 Laser-Produced Plasma," S.B. Thesis, Dept. of Physics, MIT (1973).

3. Robert Brooks, "Laser Beam Self-Focussing in a Magnetically Confined CO_2 Laser Produced Plasma," S.B. Thesis, Dept. of Physics, MIT (1974).

4. Charles S. Rosenblatt, "A Quasi-Static Model of a Radially Expanding Laser Produced Plasma with High Axial Magnetic Field," S.B. Thesis, Dept. of Physics, MIT (1974).

5. Dan Hall, "Measurement of Electron Temperature in Laser-Heated Plasmas Using Soft X-Ray Gas Absorbers," S.B. Thesis, Dept. of Physics, MIT (1975).

6. Saeed Zaki Jabbawy, "Measurement of Temporal and Spatial Dependence of Plasma Density by Mach-Zhender Interferometer," Eng. Thesis, Dept. of Nuc. Eng., MIT (1975).

7. Charles V. Karmendy, Jr., "X-Ray Temperature Diagnostics on Laser-Produced Plasmas in High Magnetic Fields," S.B. Thesis, Dept. of Physics, MIT (1976).

8. John P. Yangos, "Plasma Heating by Collision between Laser-Driven Fronts," S.B. Thesis, Dept. of Elec. Eng. and Comp. Sci., MIT (1976).

9. William Wai-Han Ma, "CO_2 Laser Irradiation of Solid Targets in High Magnetic Fields," M.S. Thesis, Dept. of Physics, MIT (1977).

10. James H. Watts, "CO_2 Laser Irradiation of Solid Carbon Targets in Transverse Magnetic Fields," S.B. Thesis, Dept. of Physics, MIT (1977).

11. John P. Yangos, "Stimulated Brillouin Backscattering from a Laser-Produced Magnetoplasma," M.S. Thesis, Dept. of Nuc. Eng., MIT (1977).

12. Mark P. Hacker, "Gas Breakdown with Far Infrared Laser Radiation in Intense Magnetic Fields," Ph.D. Thesis, Dept. of Physics, MIT (1977).

13. Nicholas George Loter, "Soft X-Ray Diagnostics for Magnetically Confined CO_2 Laser-Heated Plasmas," Ph.D. Thesis, Dept. of Physics, MIT (1979).

14. Charles V. Karmendy, Jr., "Stimulated Brillouin Backscatter from Laser-Produced Plasmas in High Magnetic Fields," Dept. of Physics, MIT (1979).